

UNIVERSITY OF OKLAHOMA

GRADUATE COLLEGE

FILAMENTOUS BIOLOGICAL MACROMOLECULES BASED
NANOSTRUCTURES AND THEIR APPLICATIONS

A DISSERTATION

SUBMITTED TO THE GRDUATE FACULTY

in partial fulfillment of the requirements for the

Degree of

DOCTOR OF PHILOSOPHY

By

BINRUI CAO

Norman, Oklahoma

2010

FILAMENTOUS BIOLOGICAL MACROMOLECULES BASED
NANOSTRUCTURES AND THEIR APPLICATIONS

A DISSERTATION APPROVED FOR THE
DEPARTMENT OF CHEMISTRY AND BIOCHEMISTRY

BY

Dr. Chuanbin Mao, Chair

Dr. Alberto Striolo

Dr. Michael Ashby

Dr. Paul Cook

Dr. Wai Tak Yip

©Copyright by BINRUI CAO 2010
All Rights Reserved.

Table of Contents

Content	Page
List of Tables	xi
List of Figures.....	xii
List of Abbreviations.....	xviii
Abstract.....	xx
Appendix	242
Chapter 1 Introduction.....	1
1.1. General Background	1
1.2. Spider Dragline Silk.....	4
1.3. Bacteriophage and Phage Display Technique.....	7
1.3.1. Biology	9
1.3.2. Chemistry.....	11
1.3.3. Phage Display.....	11
1.3.4. Liquid Crystalline Behavior	14
1.3.5. Phage Library.....	15
1.3.6. Biopanning.....	16
1.4. Bacterial Pilus.....	19
1.4.1. Structure	20
1.4.2. Biology	21
1.4.3. Chemistry.....	24

1.4.4. Isolation, Purification and Self-Assembly	25
1.5. Bone Regeneration.....	26
Chapter 2 Oriented Nucleation of Hydroxylapatite Crystals on Spider Dragline Silks.....	29
2.1. Introduction	29
2.2. Materials and Experiments	32
2.2.1. Mineralization of Silks from HAP Precursor Solution.	32
2.2.2. Microscopy Characterization of Mineralized Silks.....	33
2.2.3. Fourier Transform Infrared Spectroscopy (FTIR) Analysis.....	34
2.2.4. Energy-Dispersive X-ray Spectroscopy (EDS).....	34
2.2.5. CdS Nucleation on Silks.	36
2.2.6. Au Nucleation on Silks.	36

2.3. Results	36
2.4. Discussion	40
2.5. Conclusion.....	52

Chapter 3 Identification of Microtubule-Binding Domains on Microtubule-Associated Proteins by Major Coat Phage Display Technique	53
---	-----------

3.1. Introduction	53
--------------------------------	-----------

3.2. Methods and Experiments.....	60
--	-----------

3.2.1. Materials	60
------------------------	----

3.2.2. Fixation of Biotin-Labeled Tubulins onto a 35 mm Petri Dish.....	61
---	----

3.2.3. Affinity-Selection of Tubulin-Binding Phage Clones.....	62
--	----

3.2.4. Preparation of Starved Cells.....	63
--	----

3.2.5. Amplification of Eluates.....	63
--------------------------------------	----

3.2.6. Purification of Amplified Phages by Using Double PEG Precipitation.....	64
---	----

3.2.7. Titering of Phage.....	65
-------------------------------	----

3.2.8. Second and Third Round of Affinity Selection.....	66
--	----

3.2.9. Sequencing of Selected Phage Colonies.....	66
---	----

3.2.10. Interaction between Tubulin-Selected Phage and Free Tubulins Characterized by Transmission Electron Microscopy (TEM).	67
--	----

3.3. Results and Discussion	68
--	-----------

3.3.1. Identification of Affinity-Selected Peptides by Biopanning.	68
---	----

3.3.2. Global Characterization of Affinity-Selected Peptides.....	70
---	----

3.3.3. Identification of Potential Microtubule-Binding Domains on MAPs.....	78
3.3.4. Comparison of Our Identified Domains on Tau with Reported Domains from Literature.	89
3.3.5. Comparison of Our Identified Domains with other MAPs with Reported Domains from Literature.....	95
1. MAP1B.....	95
2. MAP1A.....	96
3. MAP1S.....	96
4. MAP4.....	97
5. MAP2.....	97
3.3.6. Advantages and Limitations of Using Landscape Phage Display for Identifying Microtubule-Binding Domains.....	98
3.4. Conclusion.....	101
Chapter 4 A Selection of Hydroxyapatite-Binding phage for the Fabrication of Bone Regeneration Scaffold.....	102
4.1. Introduction	102
4.2. Experiments.....	105
4.2.1. HAP Nanorods Synthesis	105
4.2.2. Surfactant Removal from HAP Nanorods	106
4.2.3. Solutions and Typical Methods.	107
4.2.4. Hydroxyapatite Column Preparation	107
4.2.5. Biopanning: Selection of HAP-Binding Phages.....	108
4.2.6. Receptor Ligand Contacts (RELIC).....	110

4.2.7. Specificity Determination of Selected Phages through Binding Assay	110
4.2.8. Interaction between HAP-Selected Phage and HAP Powder/HAP Nanorods and Characterized by Transmission Electron Microscopy (TEM).....	111
4.2.9. Assembly of Selected Phage and HAP Nanorods into a Scaffold	112
4.2.10. Sample Preparation for TEM and SEM Characterization.....	112
4.2.11. Harvest and Isolation of Rat MSCs	113
4.2.12. Assessment of MSCs Proliferation/Cell Viability	114
4.2.13. SEM Characterization for MSCs	115
4.3. Results	116
4.3.1. HAP Nanorod Synthesis and Surface Modification.....	116
4.3.2. Affinity-Selected Peptides	118
4.3.3. Best HAP-Binder Selections	120
4.3.4. Interaction between DSSTPSST-Phage and HAP Nanorods ..	124
4.3.5. DSSTPSST-Phage - HAP Nanorod Scaffold Fabrication.....	126
4.3.6. Proliferation of MSCs on the HAP-Phage Scaffold	132

4.4. Discussion	136
4.5. Conclusion.....	148
Chapter 5 Controlled Growth and Differentiation of Mesenchymal Stem Cells on M13 Bacteriophage Films.....	149
5.1. Introduction	149
5.2. Experiments.....	153
5.2.1. Display of Peptides on M13 Phage.....	153
5.2.2. Engineered Phage Propagation and Purification.....	154
5.2.3. Harvest and Isolation of Rat MSCs.....	155
5.2.4. Phage Film Fabrication	156
5.2.5. Methylthiazoletetrazolium (MTT) Assay.....	157
5.2.6. Scanning Electron Microscopy (SEM) for Substrate and Cell Morphological Examination.....	158
5.2.7. Immunofluorescence of Actin and Osteopontin/Osteocalcin....	158
5.2.8. Mineralized Bone Matrix Formation Assay.....	160
5.2.9. Statistical Analysis	160
5.3. Results	160
5.3.1. Characterization of the Phage Film.....	160
5.3.2. Morphology of MSCs on Phage Films.....	163
5.3.3. Proliferation of MSCs on Phage Film.....	168
5.3.4. Differentiation of MSCs on Phage Film.....	169

5.4. Discussion	173
5.5. Conclusion.....	183
Chapter 6 Novel Colloidal Crystals Self-Assembled from Rodlike Bacterial Pili Particles	185
6.1. Introduction	185
6.2. Experiments, Results, and Discussion.....	188
6.3. Conclusions.....	201
Chapter 7 Summary of Results and Future Directions	202
7.1. Summary of Results.....	202
7.2. Future Directions.....	205
7.2.1. Tissue Engineering Scaffold for Bone Regeneration	205
7.2.2. Phage Display Technique for Protein-Protein Interaction Studies.	207
7.2.3. Microtubule-Binding Phages as an Anti-Cancer Drug.....	209
7.2.4. Pili Colloidal Crystals for the Fabrication of Photonic Crystals.	210

List of Tables

TABLE 1.1	SUMMARY OF INORGANIC-MATERIAL-BINDING PEPTIDES, USED PHAGE LIBRARIES AND CORRESPONDING REFERENCES.	18
TABLE 1.2	AMINO ACID COMPOSITION OF THE TYPE 1 FIMBRIAL PROTEIN	24
TABLE 2.1	SUMMARY OF AVERAGE ANGLES BETWEEN THE C AXIS OF HAP AND THE LONG AXIS OF SPIDER SILK.....	40
TABLE 3.1	SELECTED PEPTIDE SEQUENCES AND FREQUENCY.	69
TABLE 3.2	THE INFORMATION CONTENT OF EACH PEPTIDE.	76
TABLE 3.3	POTENTIAL MICROTUBULE-BINDING DOMAINS ON MAPS FROM THE ALIGNMENT OF SELECTED PEPTIDES TO MAPS SEQUENCE.....	89
TABLE 4.1	SELECTED PEPTIDES FROM BIOPANNING.....	119
TABLE 4.2	IDENTIFIED HAP-BINDING DOMAINS ON THE BONE RELATED PROTEINS.....	141
TABLE 6.1	7 DIFFERENT CHEMICAL COMPOSITIONS OF THE AQUEOUS SOLUTIONS OF PILI WERE TRIED FOR THE ASSEMBLY OF PILI INTO 1D BUNDLES, 2D DOUBLE-LAYERED LATTICES AND 3D MULTI-LAYERED LATTICES.....	199

List of Figures

FIGURE 1.1 THE FABRICATION OF LITHIUM ION BATTERY CATHODES BY USING DOUBLE-DISPLAYED M13 PHAGES.....	4
FIGURE 1.2 MOLECULAR AND CRYSTAL STRUCTURE OF SPIDER SILKS.....	7
FIGURE 1.3 THE STRUCTURE OF A FILAMENTOUS PHAGE (M13 OR FD) AND ITS GENETICALLY ENGINEERED FASHION.....	13
FIGURE 1.4 TRANSMISSION ELECTRON MICROSCOPY (TEM) IMAGE OF M13 PHAGES STAINED BY 1% URANYL ACETATE.	14
FIGURE 1.5 PROCEDURE OF SELECTING MICROTUBULE-BINDING PEPTIDES FROM LANDSCAPE PHAGE LIBRARY (BIOPANNING).	17
FIGURE 1.6 STRUCTURE OF TYPE 1 PILUS..	21
FIGURE 1.7 OVERVIEW OF TYPE 1 PILUS ASSEMBLY THROUGH THE CHAPERONE-USHER PATHWAY [77].....	23
FIGURE 1.8 TEM IMAGES OF PILI BUNDLES AND ANGLE-LAYERED LATTICE	26
FIGURE 1.9 THE PROCESS OF BONE REGENERATION.....	28
FIGURE 2.1 TEM IMAGES AND ED PATTERNS OF HAP ON THE SPIDER SILK.....	39
FIGURE 2.2 SEM IMAGES OF HAP ON THE SPIDER SILK.	40
FIGURE 2.3 TEM IMAGE OF SPIDER SILK COATED BY CDS CRYSTALS AND GOLD CRYSTALS. THE RELATED ED PATTERNS ARE ALSO PROVIDED.	42

FIGURE 2.4 THE LATTICE MATCHING BETWEEN THE A-B PLANE OF HAP AND B-C PLANE OF NANOCRYSTALLIN DOMAIN OF THE SPIDER SILKS AS WELL AS THE HYDROGEN BONDING BETWEEN THEM.....	44
FIGURE 2.5 FT-IR SPECTRA OF O-H STRETCHING VIBRATIONS OF SYNTHETIC HAP CRYSTALS (BLUE), SPIDER SILK (PURPLE), AND SILK/HAP (RED).....	46
FIGURE 2.6 PROPOSED MECHANISMS OF ORIENTED NUCLEATION OF HAP ON THE SPIDER SILK.....	49
FIGURE 2.7 EDS SPECTRA OF SPIDER SILKS (RED) AND SPIDER SILKS AGED IN A 4MM CaCl_2 SOLUTION (BLACK).....	51
FIGURE 3.1 PROCEDURE OF SELECTING MICROTUBULE-BINDING PEPTIDES FROM LANDSCAPE PHAGE LIBRARY (BIOPANNING).....	58
FIGURE 3.2 NORMALIZED DISTRIBUTION OF INFORMATION CONTENT FOR TWO PEPTIDE POPULATIONS CALCULATED BY USING RELIC/INFO PROGRAM.....	74
FIGURE 3.3 CUMULATIVE SIMILARITY SCORE OF EACH AMINO ACID IN THE SEQUENCES OF PROTEINS OF THE MAP1 FAMILY.....	83
FIGURE 3.4 ALIGNMENTS OF SELECTED PEPTIDES WITH MAP1A.....	83
FIGURE 3.5 ALIGNMENTS OF SELECTED PEPTIDES WITH MAP1B.....	84
FIGURE 3.6 ALIGNMENTS OF SELECTED PEPTIDES WITH MAP1S.....	85
FIGURE 3.7 ALIGNMENT OF OUR SELECTED PEPTIDES WITH TAU.....	86
FIGURE 3.8 ALIGNMENTS OF SELECTED PEPTIDES WITH MAP2.....	87

FIGURE 3.9 ALIGNMENTS OF SELECTED PEPTIDES WITH MAP4.	88
FIGURE 3.10 CUMULATIVE SIMILARITY SCORE OF EACH AMINO ACID IN THE MICROTUBULE-BINDING REGIONS OF THE PROTEINS OF THE MAP2/TAU FAMILY.....	88
FIGURE 3.11 INTERACTION OF TUBULIN-SELECTED PHAGE AND FREE TUBULINS VERIFIED BY TEM.....	93
FIGURE 3.12 FORMATION OF BUNDLES DUE TO THE INTERACTION BETWEEN TUBULIN-SELECTED PHAGE (DISPLAYING TUBULIN-BINDING PEPTIDE ADTVSGMV) AND TUBULINS.	94
FIGURE 3.13 FORMATION OF BUNDLES AND NETWORKS DUE TO THE INTERACTION BETWEEN TUBULIN-SELECTED PHAGE (DISPLAYING TUBULIN-BINDING PEPTIDE AEMVKSSID) AND TUBULINS.	94
FIGURE 4.1 SCHEMATIC DIAGRAM OF DEVELOPING HAP-PHAGE SCAFFOLD FOR THE PROLIFERATION OF MESENCHYMAL STEM CELLS.	105
FIGURE 4.2 CHARACTERIZATIONS AND SURFACE FUNCTIONALIZATION OF SYNTHESIZED HAP NANORODS.....	118
FIGURE 4.3 SHARED MOTIFS AMONG SELECTED PEPTIDES FROM BIOPANNING LANDSCAPE PHAGE LIBRARIES AGAINST HAP POWDER.....	121
FIGURE 4.4 THE NUMBER OF COLONIES IN ACID ELUTED SOLUTIONS IN THE PHAGE-BINDING ASSAY.....	122
FIGURE 4.5 INTERACTIONS BETWEEN HAP-SELECTED PHAGES AND HAP POWDER.....	124

FIGURE 4.6 INTERACTIONS BETWEEN DSSTPSST-PHAGES AND HAP NANORODS.....	126
FIGURE 4.7 MORPHOLOGIES OF FORMED SCAFFOLDS BY (A) DSSTPSST-PHAGE WITH HAP NANORODS, (B) HAP NANORODS ONLY, (C) DSSTPSST-PHAGE ONLY AND (D) WILD TYPE PHAGE WITH HAP NANORODS.....	129
FIGURE 4.8 SEM IMAGES OF FORMED SCAFFOLD FROM (A), (B) AND (C) HAP NANOROD WITH DSSTPSST-PHAGE HAP NANOROD; (D) AND (E) HAP NANORODS ONLY; (F) DSSTPSST-PHAGE ONLY.	130
FIGURE 4.9 HAP NANORODS WERE ALIGNED BY DSSTPSST-PHAGES FORMING A HAP-PHAGE COMPLEX WITH A C-AXIS PREFERRED ORIENTATION..	132
FIGURE 4.10 THE PROLIFERATION OF MSCS ON CELL CULTURE PLATE, A FILM OF HAP NANORODS AND HAP-PHAGE SCAFFOLD.....	134
FIGURE 4.11 MORPHOLOGIES OF MSCS ON HAP-PHAGE SCAFFOLD AFTER 3 DAYS OF CULTURING.....	135
FIGURE 4.12 MSCS ON HAP-PHAGE SCAFFOLD. CELLULAR NUCLEOLUS OF RESIDENT MSCS WERE STAINED BY DAPI.	135
FIGURE 4.13 APPLICATION OF GEOMETRICAL CONSTRAINTS.....	138
FIGURE 4.14 PREDICTED ADSORBED-STATE PROTEIN STRUCTURES.....	139
FIGURE 5.1 M13 PHAGE FILM OBTAINED AT DIFFERENT CONCENTRATIONS (10^{12} , 10^{14} PFU/ML) OF PHAGE ASSEMBLY.	162

FIGURE 5.2 THE CELLS ELONGATED ALONG ONE DIRECTION, RADIATED FROM THE CENTRE OF THE FILM. DAPI (BLUE), PHALLOIDIN (GREEN).	165
FIGURE 5.3 AN ORDERLY ARRANGEMENT OF CELLS WHERE THE PHAGE BUNDLES ARE CONSISTENT WITH THE ORDERLY NATURE.....	166
FIGURE 5.4 THE FILMS WHICH WERE GENERATED WITH DIFFERENT CONCENTRATIONS (10^{14} , 10^{13} , 10^{12} PFU/ML) OF PHAGE CAN AFFECT THE CELL ALIGNMENT AND CELL STRETCHING DEGREE OF ORDER.....	166
FIGURE 5.5 THE SURFACE AREA OF MSCS CULTURED ON THE PHAGE FILMS GENERATED AT DIFFERENT CONCENTRATIONS OF PHAGE (10^{14} , 10^{13} , 10^{12} PFU/ML)	167
FIGURE 5.6 MSCS CULTURE ON THE TYPE OF SUBTRATES.	168
FIGURE 5.7 A) MSCS CULTURED ON A PHAGE FILM MODIFIED WITH PEPTIDE (PDPLEPRREVCE).....	168
FIGURE 5.8 MTT ASSAY RESULTS	172
FIGURE 5.9 THE PHAGE FILM COULD UP-REGAULATE OSTEOCALCIN AND OSTEOPONTIN EXPRESSION COMPARED TO THE CONTROL.	172
FIGURE 5.10 MINERALIZATION ASSAYED BY ALIZARIN RED S AT 14DAYS.....	173
FIGURE 6.1 SELF-ASSEMBLY OF PILI INTO 1D BUNDLES, 2D LATTICES AND 3D CRYSTALS.....	187
FIGURE 6.2 TEM IMAGES OF PILI ASSEMBLIES..	190

FIGURE 6.3 A) EVIDENCE SHOWING THAT THE CRYSTALLIZATION OF PILI TOOK PLACE IN A LAYER-BY-LAYER FASHION. B) PILI WERE CRYSTALLIZED INTO CRYSTALS WITH M13 PHAGE AS A CONTAMINANT. C) BACTERIAL FLAGELLA AFTER INCUBATION IN 80 MM PIMELIC ACID. D) PHAGES AFTER INCUBATION IN 80 MM PIMELIC ACID. 194

FIGURE 6.4 SILICA-PILI COMPOSITES FORMED BY TEMPLATING SILICA NUCLEATION ON PILI ASSEMBLIES. 198

FIGURE 6.5 A) SINGLE PILUS WITH A SET OF ALTERNATING RIDGES AND GROOVES WITH A PITCH ANGLE OF 21° . B) WHEN CROSSING ANGLE BETWEEN PILI A AND B IS 42° , THE RIDGES OF PILUS A CAN MAKE A REASONABLE INTERLOCKING FIT INTO CORRESPONDING GROOVES OF PILUS B. IMAGES ARE MODIFIED FROM 200

List of Abbreviations

1D, 2D, 3D	one dimensional, two dimensional, three dimensional
APTES	3-Aminopropyltriethoxysilane
Asp	aspartic acid
BSA	bovine serum albumin
DAPI	4',6-diamidino-2-phenylindole
DMSO	dimethyl sulfoxide
E.Coli	escherichia coli
ECM	extracellular matrix
EDS/EDX	energy-dispersive X-ray spectroscopy
ED	electron diffraction
FT-IR	fourier transform infrared spectroscopy
FWHM	full width at half maximum
HAP	hydroxyapatite
IP	isoelectric point
MAP	microtubule-associated protein
MTT	(3-(4,5-Dimethylthiazol-2-yl)-2,5-diphenyltetrazolium bromide
MSC	mesenchymal stem cell
OCN	osteocalcin
OPN	osteopontin
PBS	phosphate buffered saline

PCR	polymerase chain reaction
PEG	polyethylene glycol
PFU	plaque-forming unit
PRM	proline rich motif
PTA	phosphotungstic Acid
R1,R2,R3,R4	repeat 1, repeat 2, repeat 3, repeat 4
RELIC	receptor ligand contacts
SEM	scanning electron microscopy
ssDNA	single-stranded DNA
SWNT	single-walled nanotubes
TBS	tris buffered saline
TEM	transmission electron microscopy
TEOS	tetraethyl orthosilicate
WT	wild type

Abstract

In nanoscience, one promising strategy for achieving precise placements of nanomaterials and specific recognitions between individual build blocks is to use self-ordered templates to arrange them into designed pattern. Refined bio-molecules from nature, such as nucleic acids, proteins and viruses, have beautiful hierarchical nanostructures and precise molecular recognition capabilities, which make them ideal templates for fabricating hierarchical nanostructures. One branch of such biological templates is filamentous biological macromolecules like spider silks, M13 phages, tobacco mosaic virus, etc. The beauty of filamentous biological templates is that they can assemble functional nanomaterials into one-dimensional, two-dimensional or three-dimensional organizations with controlled size, shape, alignment and orientation.

This thesis presents the synthesis and assembly of nanomaterials on individual or self-assembled filamentous biological templates including spider dragline silks, bacteriophages and bacterial pili. Specifically, we found: (1) Spider dragline silks could induce the nucleation of

hydroxyapatite (HAP) crystals with preferred orientation; (2) The interactions between microtubule-associated proteins (MAPs) and microtubules were studied by biopanning of a phage displayed random peptide library against purified tubulins; (3) HAP-binding phages had an ability to attract and assemble HAP nanorods into a HAP-phage hybrid for bone regeneration; (4) Films made from bacteriophages could serve as a scaffold for the controlled growth and differentiation of resident mesenchymal stem (MSC) cells; (5) Rodlike bacterial pili particles could be induced to self-assemble into a novel colloidal crystal for nanosynthesis.

Chapter 1 Introduction

1.1. General Background

Exquisitely designed materials on the nanometer scale have shown lots of interesting and unique properties [1-4]. But how to assemble them into well-defined structures or integrate them into large-scale devices is still a big challenge. One possible solution is called the bottom-up approach, which seeks to have nano-scaled building blocks built up into functional nanosystems [5-7]. However, the difficulties in achieving the precise placements of nanomaterials and the specific recognition between individual build blocks have impeded further progress of the usage of nanomaterials. Accordingly, significant efforts have been made towards the controlled assembly of nanocomponents. One promising strategy is to use self-ordered templates to arrange nanomaterials into designed pattern. Up to now, a wide variety of ordered nano-scaled templates have been successfully employed to build functional nanosystems [8-11]. One branch of the templates is refined bio-molecules directly from nature, such as nucleic acids, proteins and viruses [12-17]. The combination of functional

inorganic nanomaterials with biological molecules has led to many two-dimensional (2D) or three-dimensional (3D) organizations of nanostructures with controlled size, shape, alignment, and orientation.

In this thesis, we are mainly focused on filamentous biological templates which include spider dragline silks, bacteriophages, bacterial pili, etc. The inherent 1-D morphologies and elegant nanostructures of these filamentous biological templates are designed for biological functions. In nanoscience, these features can be exploited to organize nanomaterials. The highly ordered functional materials have a lot of unique properties which have been or will be applied into practical applications such as high-performance batteries, sensitive biosensors and biomedical hard tissues. For example, recently, a filamentous phage-based lithium-ion battery has been fabricated with high performance [18]. The phage/FePO₄/SWNT cathode showed a capacity of 1C (1C=134 mAh/g) at a high discharge rate of 3C which is much better than the best reported record (80 mAh/g at 3C) (Figure 1.1). Moreover, the capacity retention of this phage/FePO₄/SWNT cathode upon cycling at 178 mA/g is so stable that,

even up to 50 cycles, virtually no capacity fade was observed (Figure 1.1 d). Filamentous biological macromolecules have also been utilized in biosensor area. Liu *et al.* found that phage-AuNP film exhibiting unique humidity-dependent SPR spectra could be used as a phage-based humidity sensor by means of a spectrophotometer [19]. This thesis describes how to take advantage of spider dragline silks, bacteriophages, bacterial pili to assemble functional nanomaterials into 1-D, 2-D or 3-D organizations of nanostructures with controlled size, shape, alignment and orientation for potential applications. The following three sections are about the basic structures, unique properties and related techniques of spider dragline silks, bacteriophages and bacterial pili.

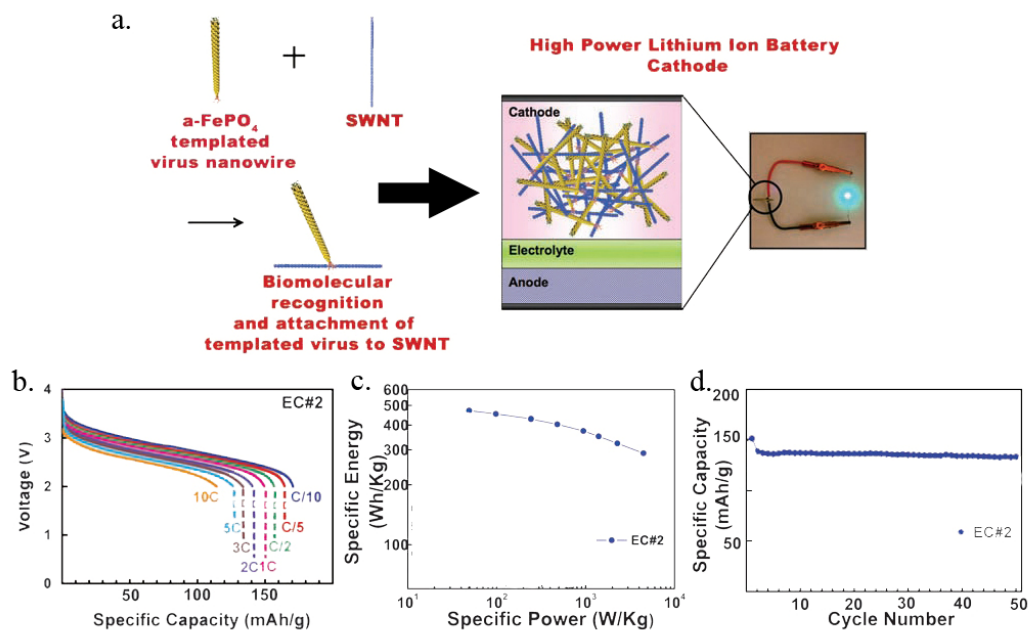


Figure 1.1 The fabrication of lithium ion battery cathodes by using double-displayed M13 phages. A) A schematic diagram for fabricating lithium ion battery cathodes by using double-displayed M13 phages. This battery can power a green LED. b and c) The electrochemical performance of phage-FePO₄-SWNT nanocomposite. b) First discharge curves at different rates c) The Ragone plot representing rate performance in terms of specific power versus energy. d) Capacity retention for 50 cycles at 1C rate. Reproduced with permission from reference 18.

1.2. Spider Dragline Silk

Spider dragline silk is a protein fiber spun by spiders. Dragline silks are used for the web's outer rim and spokes and the lifeline. Every single spider dragline silk consists of major ampullate spidroins 1 and 2 which have a highly repetitive core sequence. This sequence contains 3

consensus motifs with iterated tandem repeats which are alanine-rich stretches (A_n or $(GA)_n$), GPGXX (X often representing Q), and GGX (X represents A, L, Q or Y) [20]. The molecular structure of spider silk is composed of regions of proteins crystals separated by less organized protein chains (Figure 1.2) [21]. Hydrogen bonding and hydrophobic regions drive the self-assembly of amino acid sequences consisting of multiple repeats of A, GA or GAS into beta sheets, which further assemble into soft micelles. With increasing protein concentration, micelles transform into gel-like states, resulting in liquid crystalline structures. This crystalline beta sheets contribute to the high tensile strength of spider dragline silks. GPGXX formed beta-turns and GGX based helical structures make up of the non-crystalline regions which account for the elasticity of silks. The protein nanocrystals are oriented with their *c* axis distributed along the long axis of the silk with a 23° fwhm [22]. Hence, the silk protein molecules are well oriented along the silk (Figure 1.2) [16].

Spider dragline silks are incredibly tough and are stronger by weight than steel. Their mechanical properties render them an ideal

biomaterial for tissue engineering and other applications. Several groups have already treated spider silks as supporting scaffolds to assist the growth of resident cells and observed some positive results [23, 24]. On the other hand, mineral-coated silk fibers have been readily produced by a straightforward approach using nanoparticle suspensions [25]. Such silk-mineral hybrids that combine the strength and elasticity of naturally occurring spider silks with physical properties such as magnetism, electrical conductivity, or semiconductivity from nanoparticles might be useful as smart structural fabrics in a range of applications. Recently, scientists have produced soluble recombinant silk proteins in mammalian cells and spun them into recombinant spider silks which exhibited toughness and modulus values comparable to those of native dragline silks but with lower tenacity [26]. This technique could be used to increase the production of high quality silks and broaden their applications in textile industry, tissue engineering, etc.

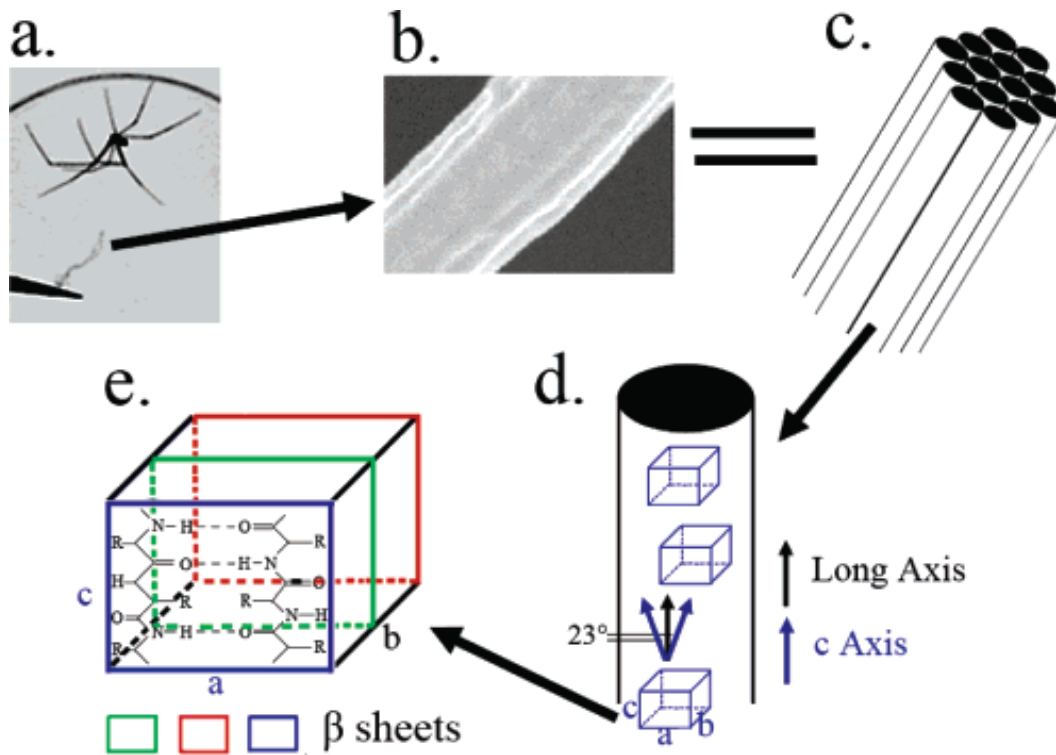


Figure 1.2 Molecular and crystal structure of spider silks. (a) The spider in the corner of a Petri dish and the silks (secreted by this spider and held by tweezers) that we used in this experiment. (b) SEM images of spider silk. (c) Hierarchical structure of a single strand of silk showing that it is assembled from many oriented fibrils. (d) Structure of a spider silk fibril showing that the protein nanocrystals are preferentially oriented with their c axis distributed along the fiber axis with a 23° fwhm. (e) Unit cell of nanocrystalline regions (made of oriented beta sheets) in a fibril, showing that the beta sheets are parallel to the c axis. [16] Reproduced with permission from reference 16.

1.3. Bacteriophage and Phage Display Technique

Filamentous bacteriophage (phage), which can specifically infect bacteria, has a refined nanostructure, genetically programmable system,

and astonishing stability. These properties are all attractive to materials scientists. Although the natural function of phage is to store and transport genetic materials, it has recently been employed to serve as biotemplate for the synthesis and assembly of nanomaterials [13, 14, 19, 27-41]. Phage-based nanosystems can be employed in practical applications such as lithium ion battery [42], biosensors [19, 43], and bone mimics which greatly encouraged scientists to explore more this promising field.

Among various different biotemplates studied for the synthesis and assembly of nanomaterials, filamentous phage has been demonstrated to be the most powerful for several reasons. First, a well-established technique, called phage display [44], can be used to identify and generate phages that can specifically bind to target nanomaterials. The process includes several steps: identifying a target-binding peptide from a combinatorial phage library, displaying the peptide on the outer surface of phage, and then assembling nanomaterials along the side wall of engineered phage [10, 32]. Luckily, many targeting peptides against various materials have already been identified and are ready to be used.

Second, phage is chemically stable in various media (most acid, basic, and organic solvents) and thermally stable until 80°C [45]. Third, the mass production of identical phage nanofibers from natural factories, bacteria, yields phage nanofibers that are extremely monodispersed [45]. Fourth, up to 3 different peptides can be displayed on the coat proteins simultaneously, making it possible for an individual nanofiber to assemble more than one functional nanomaterials (Figure 1.3) [46, 47]. Fifth, individual phage nanofibers can self-assemble into ordered structures [28, 48-51], which could further direct the assembly of nanomaterials.

1.3.1. Biology

The phages successfully used in templated nanosynthesis are the filamentous M13 phage and fd phage. Wild-type M13 phage is a flexible nanofiber of 6.5nm in diameter and 930nm in length (Figure 1.4). A circular 6407-base single stranded DNA (ssDNA) genome is packed into a protein coat, which is composed of 2700 copies of major coat proteins (pVIII) and 5 copies of each minor coat protein (including pIII, pVI, pVII, and pIX) (Figure 1.3). 2700 copies of pVIII proteins form the side wall,

while 5 copies of pIII and pVI are located at one tip, and 5 copies of pIX and pVII at the other tip. The ssDNA genome encodes a total of 11 proteins including 5 structural coat proteins. In order to understand the phage display technology, it is better to know the M13 life cycle: briefly, pIII of M13 phage binds to bacteria through the F-pilus and at the same time, the ssDNA genome is injected into the bacterial cell. Then thousands copies of ssDNA and phage coat proteins are synthesized by the bacterial factory. After that, the synthesized ssDNA and coat proteins are assembled and secreted simultaneously from cell membrane. Finally, the new M13 phages are released from bacterial cells without killing them. The fd phage has an almost identical structure and morphology with like the M13 phage, with two small differences: the fd phage has about 4000 copies of major coat protein pVIII instead of the 2700 copies in M13, and the Asn of the 12th amino acid of pVIII in M13 is substituted by the Asp in fd phage [44, 52].

1.3.2. Chemistry

Whether a phage can serve as an ideal template is mainly determined by its surface chemistry. Because there are a lot more copies of pVIII proteins than other 4 coat proteins, pVIII coat proteins dominate the outer surface and therefore determine the surface chemistry of the phage (Figure 1.3). For a wild-type M13 phage, the amino terminus of each pVIII protein is exposed to the surface with the first four to five residues (AEGDD) extending away from the phage. So it can be easily figured out that on the phage surface there are 2700 copies of Glu and 5400 copies of Asp which both have carboxyl groups leading to a negatively charged surface. The experimental isoelectric point (IP) value of 4.2 also confirmed the negative phage surface charge. For chemical modification, surface carboxyl groups and amino groups (7th residue is Lys) are able to interact with other molecules in mild conditions [44, 52].

1.3.3. Phage Display

The beauty of using phage as a template is that one can change their surface chemistry easily by controlling the biology. This well

established biological technique is called phage display. The principle is: by inserting DNA encoding foreign peptides into the N terminal genes of coat proteins, the peptides can be fused onto the outer surface of the phage either at the tips (pIII or pIX display) or along the length (pVIII display) (Figure 1.3). Briefly, through genetic engineering, designed peptides can be site-specifically displayed at the tip and/or along the side-wall of a phage. Although single display, either pIII display or pVIII display is mostly preferred and used, double or triple display of different peptides on a single phage fiber can also be achieved (Figure 1.3). Therefore, by phage display technique, the surface chemistry of a filamentous phage can be site-specifically controlled [44, 52].

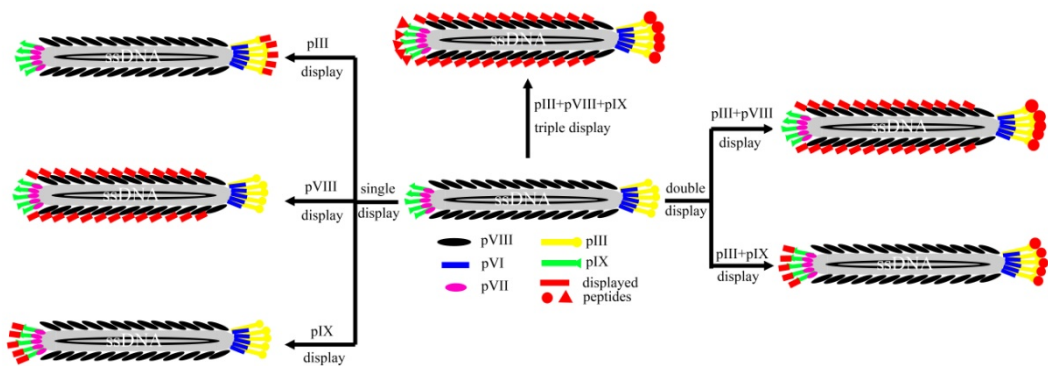


Figure 1.3 The structure of a filamentous phage (M13 or fd) and its genetically engineered fashion. A ssDNA is backed into a protein coat which is composed of thousands copies of major coat proteins (pVIII) and 5 copies of each minor coat proteins (including pIII, pVI, pVII, and pIX). Single, double or triple display of different peptides on the surface of a single phage fiber could be achieved, leading to the site-specific modification of the phage surface. The foreign peptides fused to the coat proteins are highlighted in red.

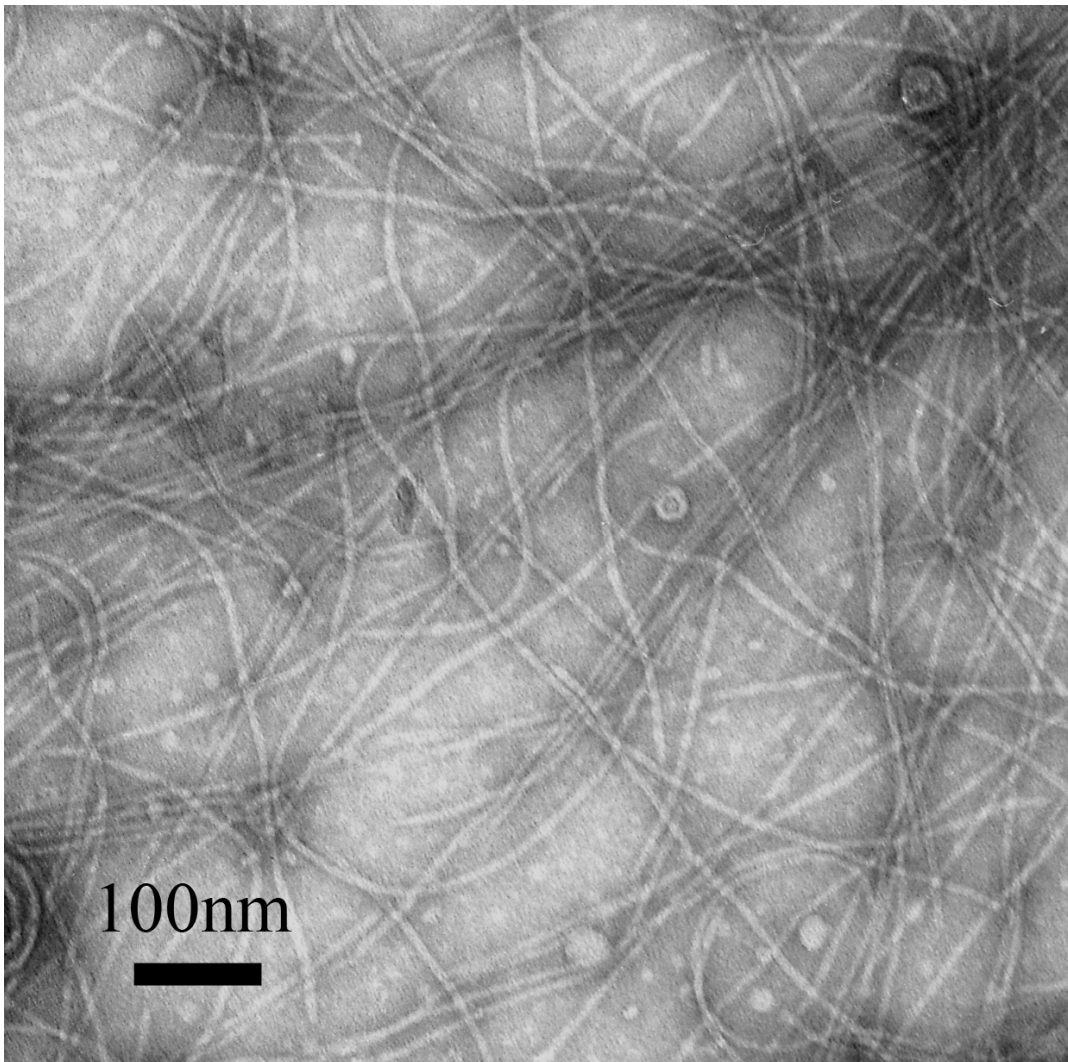


Figure 1.4 Transmission electron microscopy (TEM) image of M13 phages stained by 1% uranyl acetate.

1.3.4. Liquid Crystalline Behavior

Not only the controllable surface chemistry of phage is attractive, its unique physical properties are also interesting. The most attractive one is that filamentous phages with certain concentration can form liquid crystal

structure [48]. With increasing concentration, filamentous phages exhibit the following phase sequence: isotropic, nematic, cholesteric, smectic A and smectic C [48]. This ordered phage self-assembling system has been used to fabricate highly ordered functional nanoparticle composite [28].

1.3.5. Phage Library

For single peptide display, we can just insert peptide DNA into the gene of pIII, for example, resulting in the peptide displayed at one tip of outer. Similarly, if we insert randomized DNA sequences into the genes of pIII coat protein, a library of billions of M13, or fd, phages can be fabricated in which each phage displays a unique foreign peptide at its tip (pIII). This tip-displayed library, also called pIII phage library, is the most popular one which is commercial available from New England Biolabs. Petrenko and Smith et al. [53] developed a new side-wall-displayed phage library which is called landscape phage library or pVIII phage library. In this library, there are billions of fd-tet phages with each phage displaying one unique peptide on the side wall (fused to each of the 4000 copies of pVIII major coat protein) of the phage.

1.3.6. Biopanning

Either tip-display (pIII) phage library or landscape (pVIII) phage library can be used to identify a peptide out of billions of candidates that can specifically bind to a target. Targets include inorganic materials through a biological evolutionary selection process, called biopanning. Figure 3 illustrates the biopanning process by using landscape phage library. A landscape phage library is allowed to interact with the immobilized target leaving some phages to bind the target, while some do not. Nonbinding phages are then washed away followed by the elution of binding phages from the target. The eluate containing the target-binding phages are amplified by infecting bacteria *E. coli* forming an enriched library. To find the best target binder, the enriched library is treated as a new input and allowed to interact with the target again. After 3 rounds of selection, enriched phage library containing reduced number of phages is sequenced to figure out the specific peptide displayed on the phages that survive in the biopanning process. In theory, a specific target will correspond to a unique target-binding peptide identified from biopanning.

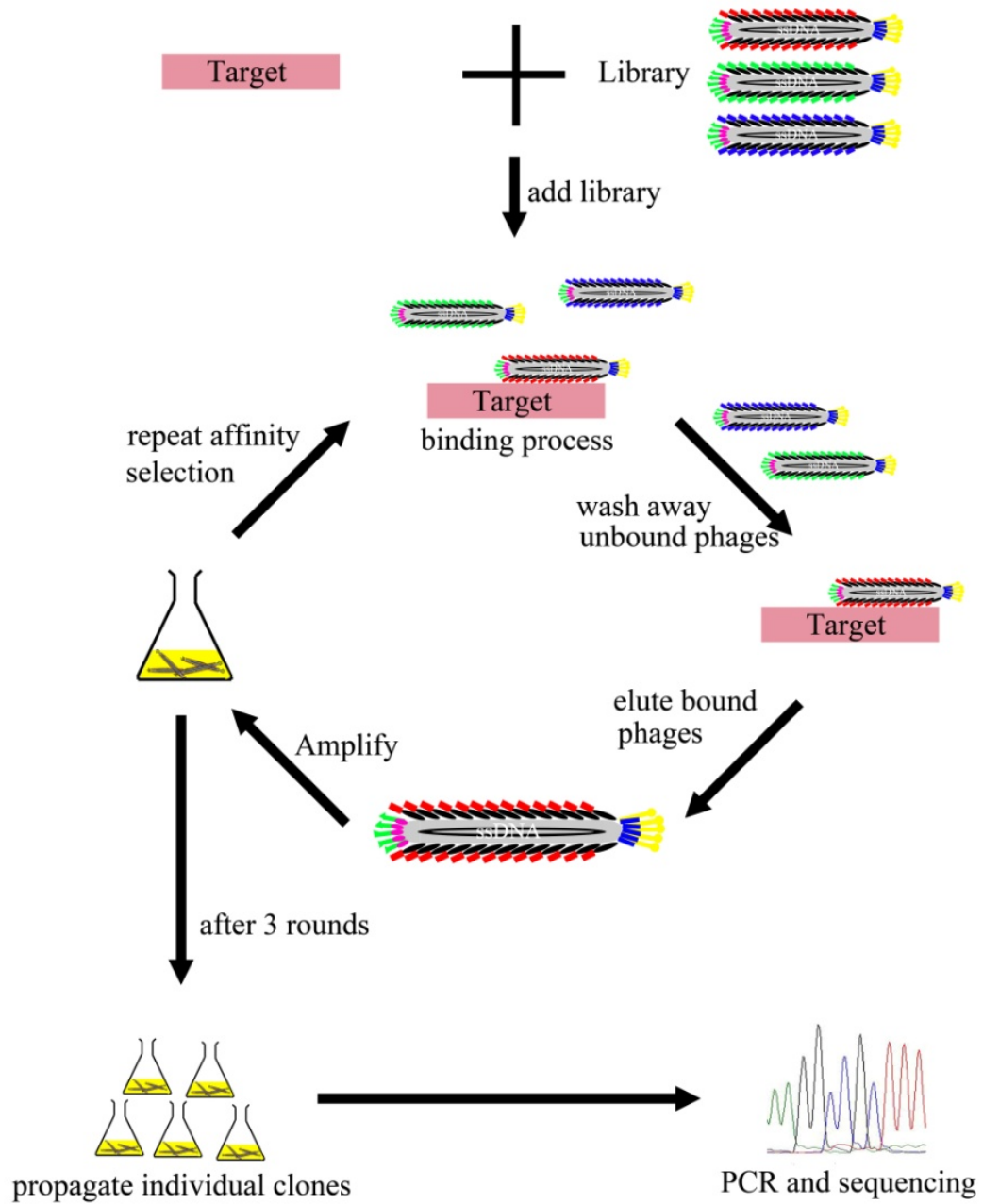


Figure 1.5 Procedure of selecting microtubule-binding peptides from landscape phage library (Biopanning).

Biopanning has been successfully applied to the identification of peptides that can specifically bind to inorganic materials such as GaAs, GaN, Ag, Pt, Au, Pd, Ge, Ti, SiO₂, Quartz, CaCO₃, ZnS, CdS, Co, TiO₂, ZnO, CoPt, FePt, BaTiO₃, CaMoO₄, Hydroxyapatite, C₆₀, and carbon nanotube. All the binding peptides, used phage libraries and corresponding references are all summarized in Table 1.1. Phages displaying these peptides have also been used to template the synthesis and assembly of the corresponding materials, forming ordered and functional nanosystems.

Table 1.1 Summary of inorganic-material-binding peptides, used phage libraries and corresponding references.

Libraries	Materials	Sequences	References
12mer-pIII	GaAs	AQNPSDNNTHH	[27]
12mer-pIII	GaN	SVSVGMKPSRP	[54]
12mer-pIII	Ag	NPSSLFRYLPSD	[55, 56]
C7C-pIII	Pt	PTSTGQA	[57]
C7C-pIII	Pd	SVTONKY	[58]
		SPHPGPY	[58]
		HAPTPML	[58]
12mer-pIII	Ti	RKLPDA	[59]
7mer-pIII		TLHVSSY	[60]
8mer-pVIII	Au	VSGSSPDS	[37]
12mer-pIII	SiO ₂	MSPHPHPRHHHT	[61]
		RGRRRRLSCRL	[61]
		KPSHHHHHTGAN	[61]
12mer-pIII	Quartz(SiO ₂)	RLNPPSQMDPPF	[62]
12mer-pIII	CaCO ₃	HTQNMRMYEPWF	[63]
15mer-pVIII		DVFSSFNLKHM	[63]
		AYGSSGFYSASFTPR	[64]

C7C-pIII	ZnS	NNPMHQN VISNHAESSRRL	[28] [14]	
C7C-pIII 12mer-pIII	CdS	TYSRLHL SLTPLTTSHLRS	[31] [14, 31]	
8mer-pVIII 12mer-pIII	Co ²⁺ Co	EPGHDAVP HYPTLPLGSSTY	[38] [56]	
12mer-pIII	TiO ₂	RKKRTKNPHTKL	[65]	
12mer-pIII	ZnO	EAHVMHKVAPRP	[66]	
12mer-pIII	FePt	HNKHLPTQPLA	[13, 67]	
12mer-pIII	BaTiO ₃	HQPANDPSWYTG NTISGLRYAPHM	[68] [68]	
12mer-pIII	CaMoO ₄	YESIRIGVAPSQ DSYSLKSQLPRQ	[69] [69]	
12mer-pIII	CoPt	KTHEIHSPLLHK	[13, 70]	
12mer-pIII C7C-pIII 12mer-pIII 12mer-pIII 12mer-pIII	Hydroxyapatite	SVSVGMKPSRP MLPHHGA APWHLSSQYSRT STLPIPHEFSRE VTKHLNQISQSY	[71] [72] [73] [73] [73]	
12mer-pIII		Ge	SLKMPHWPHELLP TGHQSPGAYAAH	[74] [74]
12mer-pIII		SWNT	HWSAWWIRSNQS HWKHPSGAWDTL	[75] [75]
12mer-pIII		Carbon Nanohorn	DYFSSPYEQLF	[76]
C7C-pIII		C ₆₀	NMSTVGR	[77]

1.4. Bacterial Pilus

Pilus is a protein fiber on the surface of bacteria. Its main biological function is to mediate adherence to host cells. From the point of view of nanoscientists, it has a nano-sized scale, a genetically engineerable body, and it is also easily produced. These features render it a promising

biological template for nanosynthesis. In this work, the type of pilus we used is *E.coli* type 1 pilus.

1.4.1. Structure

Type 1 pili have a stiff, rod-like appearance. They cover the bacteria body like spines on a hedgehog. Each pilus is about 0.5-2 μm long and 7 nm wide with a longitudinal cavity inside (Figure 1.6). Structurally, it is helically assembled from more than 3000 copies of protein subunit called fimA and a linear tip fibrillum. The fibrillum is formed by one copy of the adhesion fimH at the tip and several copies of FimG and FimF [78-80]. High resolution TEM images show that helical pili tubes are right-handed with a 19.31nm long helical repeat consisting of 27 FimA subunits in eight turns (Figure 1.6) [79]. The principle of the association between continuous subunits is termed “donor strand complementation”. Each subunit possesses an N-terminal extension of about 15 residues act as a donor strand to complement the fold of the previous subunit (Figure 1.6c). FimH only has a much longer N-terminal segment instead of a

donor strand extension so that it can only be incorporated at the tip of the pilus.

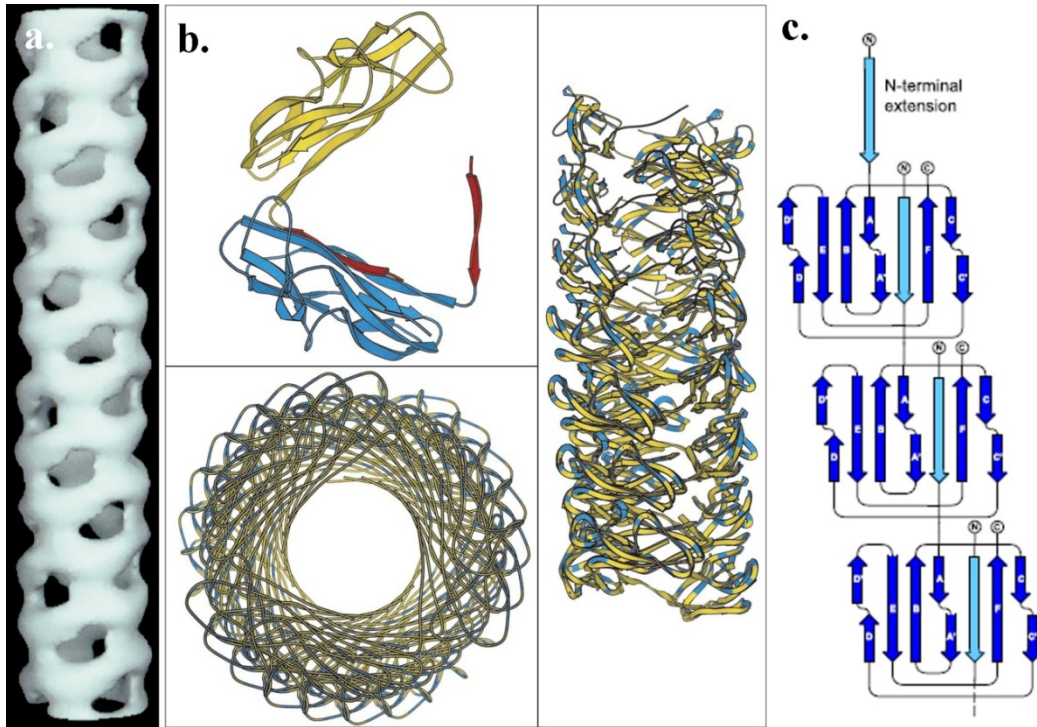


Figure 1.6 Structure of type 1 pilus. a) The 3-D reconstruction of the pilus [79]. b) Model of the type 1 pilus [81]. c) Schematic beta-sheet topology of a mature pilus fiber [78]. Reproduced with permission from reference 77 and 80.

1.4.2. Biology

Type 1 pili are expressed by as many as 80% of all wild-type *E.coli* strains associated with severe infections of the upper urinary tract. Figure 1.7 represents the assembly of type 1 pili through the chaperone-usher

pathway. The periplasmic chaperone FimC binds pilus subunits in periplasm which is secreted by the Sec YEG translocon and delivers FimC to the transmembrane assembly platform FimD. FimD recognizes binary chaperone-subunit complexes and incorporates subunits into the pilus [78, 82]. Genetically, the translated nucleotide sequence of the main subunit of pilus, FimA, has been determined and contains a 23-residue signal peptide and a 158-amino acid processed subunit yielding a relative molecular weight of 15706 [83]. When foreign peptide sequences are fused into the specific positions of the gene of FimA or FimH, they can be displayed on the outer surface or the tip of the protein fiber [82]. This finding demonstrated that the surface chemistry of type 1 pilus is tunable by varying displayed peptides. Moreover, random peptides have also been displayed at the exposed regions of FimH so that this pili based expression system can be a powerful tool for epitope mapping or antibody engineering [82]. With regard to its biological functions, type 1 pilus can not only mediate adherence to host cells, but also internalize into bladder epithelial cells [84]. The tip FimH subunit can interact with the surface of bladder epithelial cell and cause the cytoskeletal rearrangements,

resulting in the internalization of uropathogenic *Escherichia coli* into bladder epithelial cell.

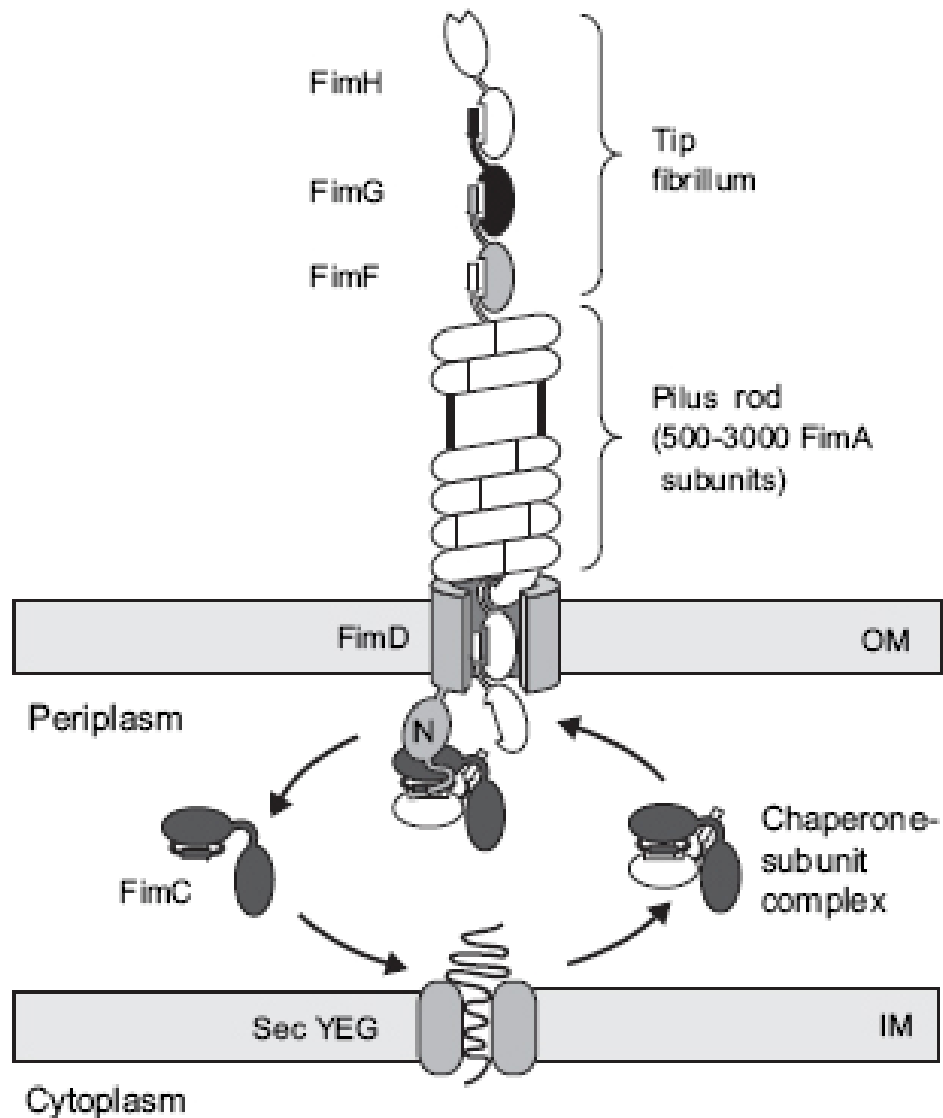


Figure 1.7 Overview of type 1 pilus assembly through the chaperone-usher pathway [78]. Reproduced with permission from reference 77.

1.4.3. Chemistry

There are a lot more copies of FimA than other 4 subunits, FimA proteins dominate the outer surface and therefore determine the surface chemistry of pili (Figure 1.6). Each FimA consists of 181 amino acids including 51 hydrophobic residues, 8 positively charged residues and 10 negatively charge residues (Table 1.2), showing a high proportion of hydrophobic residues and a low proportion of basic amino acids. Piliated cells tend to form pellicles at the air-liquid interface of a still culture and will adhere to almost any surface. From the 3-D model of FimA, we can see the exposed surface of subunits is mainly composed of basic, acidic and polar residues. An isoelectric point of 3.9 indicates an anionic surface of such protein fibers. For chemical modification, surface carboxyl groups and amino groups are able to interact with other molecules in mild conditions.

Table 1.2 Amino acid composition of the type 1 fimbrial protein [83].

Amino Acid	Amount in protein	Amino Acid	Amount in protein
Asp	8	Val	17
Asn	11	Met	1
Thr	21	Ile	6
Ser	14	Leu	15

Glu	3	Tyr	2
Gln	10	Phe	7
Pro	2	His	2
Gly	16	Lys	5
Ala	36	Arg	3
Cys	2	Trp	0

1.4.4. Isolation, Purification and Self-Assembly

Under conditions of limiting oxygen and high cell concentration, pili are favored to grow on the surface of bacteria cells. Therefore, a long time (24 hours) of incubation of *E.coli* cells in a sealed flask with a gentle shaking can increase piliated cells and number of pili on each cell. Then pili were detached from cells by mechanical shearing and purified by double PEG-based precipitations. Under the inducing by salts or multivalent positive molecules such as polylysine, purified pili can form well-aligned paracrystalline bundles or angle-layered lattice [85-87]. These induced self-assemblies can be used as templates to produce novel nanostructures.

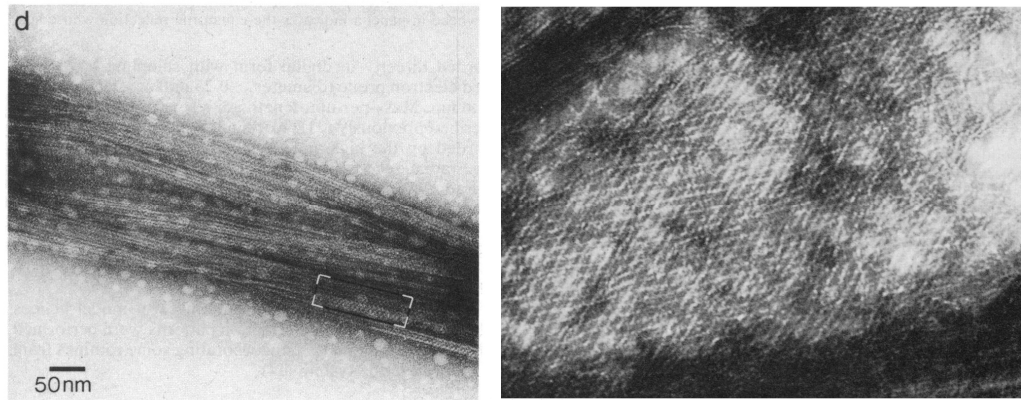


Figure 1.8 TEM images of pili bundles and angle-layered lattice [88]. Reproduced with permission from reference 87.

1.5. Bone Regeneration

Chapter 2, 4 and 5 are related to hydroxyapatite crystals and bone related cells. The final goal of this research is to heal bone defect using biomaterials-based tissue engineering. A brief introduction about bone regeneration is necessary.

Bone defect is a clinical problem for millions of people all over the world. Conventional solutions including autogenous bone graft, allograft and xenograft, especially autografts, have long been considered the gold standard of the biomaterials for bone repair [89, 90]. However, limitations were encountered with their usage, such as the shortage of supply, the

risk of donor site morbidity, and the possibility of pathogen transfer and graft rejection. To overcome these shortcomings, alternative biomaterials including synthetic polymers, alloys, metals, ceramics and biopolymers have been developed [91-96]. Among them, hydroxyapatite (HAP), a calcium phosphate ceramic, has been considered to be the best due to its high biocompatibility, bioactivity, and osteoconductivity. As the main inorganic component of natural bone, HAP can bind to natural bone [97], stimulate bone regeneration and enable it to be gradually substituted by newly formed bone. For a long time, conventional large sized HAP ceramics have been incorporated into biomaterial composites.

Bone is a hierarchically structured composite material, containing multiple levels of organization. Bone regeneration by tissue engineering method also includes several steps (Figure 1.9). First, hydroxyapatite crystals pack with collagen fibers, or their substitutes, to form larger fibers. Second, a lot of large composite fibers self-assemble into a scaffold. Third, bone cells are grown on the scaffold, and the whole system is implanted into defective bone for regeneration.

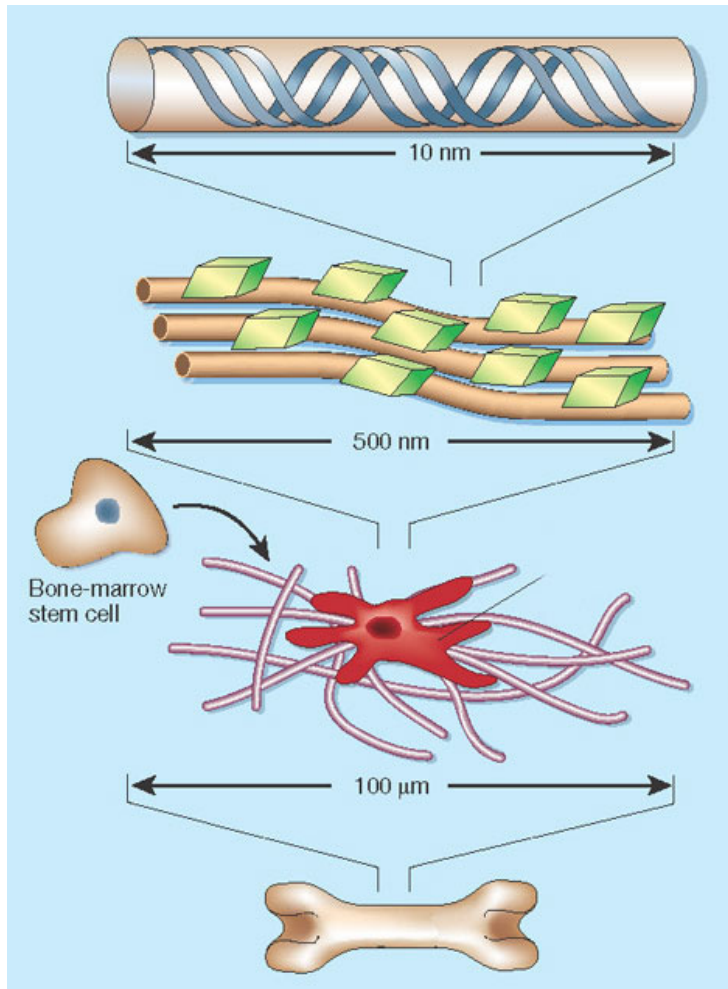


Figure 1.9 The process of bone regeneration. Reproduced with permission from reference [98].

Chapter 2 Oriented Nucleation of Hydroxylapatite Crystals on Spider Dragline Silks

2.1. Introduction

This work has been published as reference 16. Biomineralization has been mimicked for the fabrication of biomaterials [13, 14, 30, 99-104] which play an important role in hard tissue (e.g., bone) growth and maintenance. Interfacial molecular recognition is the core of this process and has strong ties to protein structures [101]. Several mechanisms of interfacial molecular recognition have been proposed to explain the controlled nucleation and growth of minerals in biomineralization such as lattice matching, stereochemistry matching, and electrostatic interaction at the protein-inorganic interfaces [101, 103]. The key to lattice and stereochemistry matching is the interaction of protein side chains with ions. The R-helix motif of a protein has been shown to have a lattice match with Ca^{2+} in the nucleation of hydroxylapatite (HAP, $\text{Ca}_{10}(\text{PO}_4)_6(\text{OH})_2$) [105] and other crystals [106]. We found that stereochemistry matching due to hydrogen bonding between an organic residue and OH^- can control the

crystal orientation of HAP [103]. Electrostatic attraction between two oppositely charged species helps to accumulate ions at the interfaces [105, 107]. Overall, interfacial molecular recognition leads to local supersaturation, followed by the nucleation of crystals with controlled structure and orientation.

The fabrication of artificial bone materials to replace traditional bone grafts is becoming a promising area. Bone has a very complicated hierarchical structure, but the basic organizational unit is mineralized type 1 collagen fibrils, formed as a result of the oriented nucleation and growth of HAP crystals on the collagen fibrils. HAP crystals are preferentially oriented with their *c* axis parallel to the long axis of collagen molecules that have triple helices [108]. Therefore, as a biomimetic strategy, many fiberlike organic materials have been used as templates to grow HAP to form a mineralized fiber that can be used as a building block for bone implant fabrication, such as collagen fibers isolated from animal tissues [109], synthetic organic fibers [107], silk fibroin [110], and sequence-engineered scaffolds [111]. Those templates can grow HAP, but few of

them can form HAP crystals with a preferred orientation similar to that in natural bone.

Although other silks such as those from cocoons have been used to nucleate HAP [112], there has been no report on using natural spider dragline silks for HAP nucleation. Spider dragline silk not only has excellent mechanical properties but also is an ideal potential template for HAP nucleation because of its semi-crystalline structure and repeated sequences (such as $(A)_n$ and $(GA)_n$) [110, 113]. Although the structural details of spider dragline silk were not as clear as those of type 1 collagen, its main secondary structure and repeated amino acid sequences such as alpha-helix, beta-sheets, repeated poly A motifs, and GPGX motifs are already known [113]. Spider dragline silk can be pictured as the oriented organization of protein nanocrystals (<10 nm, made of oriented β sheets) along the long axis with their spacing filled by amorphous protein domains (Figure 1.2) [22, 114, 115]. The protein nanocrystals are oriented with their c axis distributed along the long axis of the silk with a 23° fwhm (Figure 1.2d) [22]. Hence, the silk protein molecules are well oriented along the

silk. It was also found that beta-sheets, which also exist in the spider silk protein nanocrystals, tend to absorb Ca^{2+} ions [112, 116-118]. These facts indicate that spider dragline silk may bind Ca^{2+} from a HAP precursor solution and organize ions into an ordered array that favor HAP nucleation. Therefore, spider silk is a potential template for the controlled nucleation of HAP crystals from solution.

In this work, we allowed natural spider dragline silks to interact with a HAP precursor solution and found that HAP crystals grew on the silks consistently with their *c* axis preferentially oriented at an average angle of 72.9° with respect to the long axis of the spider silk at different times. We believe that the structure of spider silk is the key factor in the oriented nucleation of HAP crystals.

2.2. Materials and Experiments

2.2.1. Mineralization of Silks from HAP Precursor Solution.

The spider dragline silks were secreted by the daddy longlegs spider. They were collected, washed with water, and then incubated in a supersaturated HAP solution (pH 7.01), which was prepared by following a

reported procedure [119], at room temperature for different times. Specifically, 50mM hydroxyapatite crystals were dissolved in 100mM HCl and diluted by NaCl solution to a working solution with 4mM of hydroxyapatite and 200mM of NaCl. After that, KOH was used to adjust the pH of the final solution to 7.01. Our previous work successfully demonstrated that this solution can serve as a mineralization solution to nucleate and grow HAP on functionalized organic templates.

2.2.2. Microscopy Characterization of Mineralized Silks.

After different incubation times (1 hour, 4 hours, 16 hours and 10 days), silks were taken out of the solution, washed, dried, and transferred to a carbon supporting film for transmission electron microscopy (TEM) characterization and to a mica surface for scanning electron microscopy (SEM) characterization. The TEM is a JEOL 2000-FX intermediate voltage (200 000 V) scanning transmission research electron microscope, and the SEM is a JEOL JSM-880 high-resolution scanning electron microscope. Selected area electron diffraction (ED) was performed on different

mineralized spider silks and on different sections of an individual mineralized spider silk in the TEM.

2.2.3. Fourier Transform Infrared Spectroscopy (FTIR) Analysis.

To understand the mechanism of nucleation, FTIR analysis was performed on three samples: synthesized HAP crystals, spider silks, and HAP-coated spider silks. Both mineralized and nonmineralized spider silks were heated in an oven at 50 °C for 2 days to remove the adsorbed water. The synthesized HAP crystals were powders purchased from Sigma-Aldrich and were held at 150 °C for 12 h to increase the crystallinity and remove adsorbed water. Then three samples were mixed with KBr crystals, finely grounded and processed into homogenous and transparent sample-KBr pellets. They were then analyzed on a Nexus FTIR spectrometer from Nicolet.

2.2.4. Energy-Dispersive X-ray Spectroscopy (EDS).

EDS is an analytical technique used for the elemental analysis or chemical characterization of a sample. In principle, an atom within the sample contains ground state electrons in discrete energy levels. The

incident beam may excite an electron, kicking it out from the shell while creating an electron hole where the electron was. An electron from an outer, higher-energy shell then fills the hole, and releases the energy between the higher-energy shell and the lower energy shell in the form of an X-ray. The energy of the X-rays are characteristic of the difference in energy between the two shells, and of the atomic structure of the element from which they were emitted, this allows the elemental composition of the specimen to be measured.

To determine if the spider silks could bind Ca^{2+} from the HAP solution, the spider silks were washed and incubated in a 4mM CaCl_2 solution, which has the same concentration of Ca^{2+} as the supersaturated HAP solution (pH 7.01), for 1 day at room temperature. After incubation, the spider silks were washed and dried with filter paper. Then they were transferred onto a TEM grid and observed on the JEOL 2000-FX intermediate voltage (200 kV) scanning transmission research electron microscope. An EDS detector was used to analyze the elements presenting in the spider dragline silks to identify if spider silks can attract

calcium ions from supersaturated HAP solution by electrostatic interactions.

2.2.5. CdS Nucleation on Silks.

The spider silks were incubated in 100ml 100mM CdCl₂ solution at room temperature for one night. Then 10ml 1M Na₂S₂O₃ was added to the solution to induce the nucleation of CdS crystals on silk surface. After 12 hours, the spider silks were transferred onto an amorphous carbon supporting film for TEM and ED characterization.

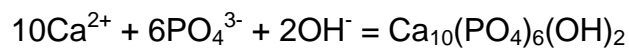
2.2.6. Au Nucleation on Silks.

The spider silks were incubated in 100ml HAuCl₄ (0.2%) solution at room temperature for one night. Then 3ml 0.1mg/ml NaBH₄ was added to the solution to induce the reduction of HAuCl₄ into Au on silk surface. After 12 hours, the spider silks were transferred onto an amorphous carbon supporting film for TEM and ED characterization.

2.3. Results

The spider dragline silks were incubated in the supersaturated HAP (pH 7.01) solution at room temperature for different times (1 hour, 4 hours,

16 hours and 10 days). After 10 days, the pH value of the solution dropped to 6.59. This result is consistent with the fact that OH⁻ ions are transferred from the solution to the lattice of HAP crystals grown on the silks (Figures 2.1 and 2.2). Crystallization of HAP from the precursor solution used in this study can be summarized by the following equation



which indicates that the reduction of pH value serve as an effective indicator of the process of HAP crystal nucleation and growth on the spider silks from the mineralization solution [102-104]. It also indicates that with the reduction of pH, OH⁻ ions are being transferred from the solution phase to the lattice of mineral phase. Electron diffraction (ED) patterns (Figure 2.1) of the crystals on the silks show that those crystals are HAP. Surprisingly, among all of the mineralized silks that we studied, the ED patterns show that the diffraction spots from the (002) plane of HAP do not form a ring that is a characteristics of the electron diffraction pattern from a randomly oriented crystalline HAP sample. Instead, the diffraction spots from the (002) plane of HAP on the spider silks form a very short arc,

indicating that HAP crystals were nucleated on the spider silks with a *c*-axis preferred orientation. In the ED patterns shown in Figure 2.1, the heads of the double-headed black arrows indicate the (002) diffraction spots. Therefore, the double-headed black arrows represent the *c*-axis orientation of the spider silks from which the corresponding patterns were taken. We then measured the angles between the *c*-axis orientation derived from the ED patterns and the long axis of the corresponding silks derived from the TEM images. We found that the angle between the *c* axis of HAP crystals and the long axis of the silks ranges from 69.9 to 78.4° (Table 2.1 and Figure 2.1). The average angle at each time point in Table 2.1 is calculated from the orientation angles of multiple spider dragline silks studied under TEM. These results indicate that the HAP crystals have a similar preferred orientation at different incubation times and on different silk samples, indicating that the oriented nucleation of HAP on silks is directly related to the oriented structure of silks used in this study. The variation of the average angles between the *c* axis of HAP and the long axis of the template in Table 2.1 is probably due to the distribution of the orientation of the *c* axis of the protein nanocrystals in the skin area of

the silks with respect to the long axis of the silks [22]. Moreover, ED patterns taken from different sections of an individual silk are similar, indicating that the preferred orientation of HAP along one strand of silk is uniform (Figure 2.1d).

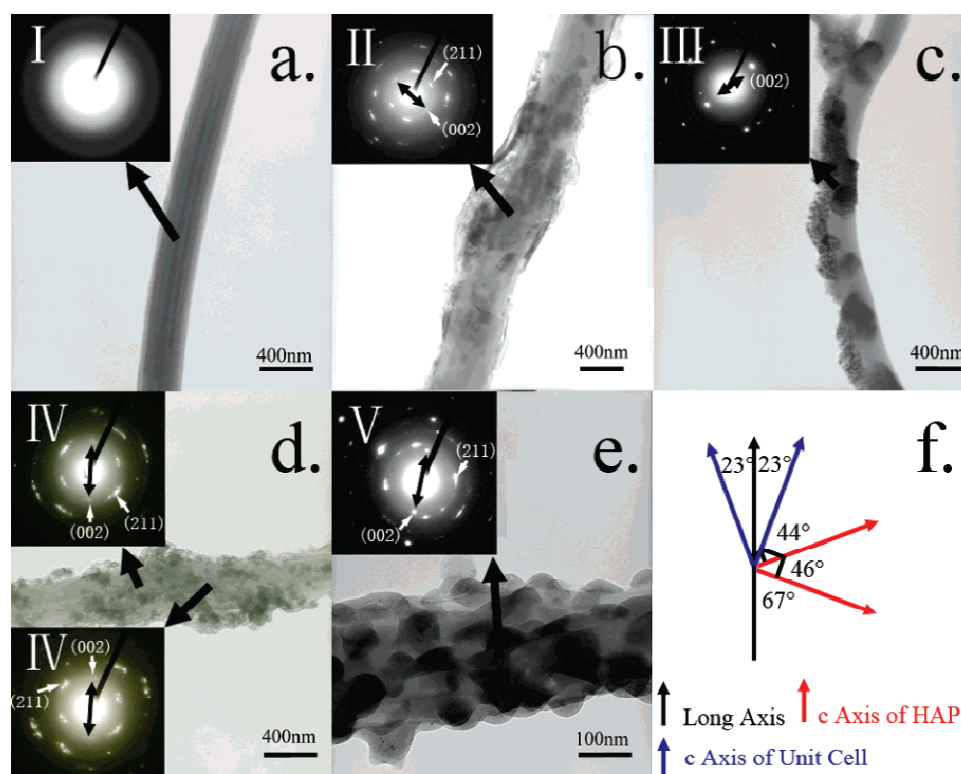


Figure 2.1 TEM images and ED patterns of HAP on the spider silk. (a) spider silk without HAP, (b) after 1 h of incubation, (c) after 4 h of incubation, (d) after 16 h of incubation, (e) after 10 days of incubation, and (f) calculated angles between the long axis of a strand of silk, the c axis of the silk unit cell, and the c axis of HAP. I-V are ED patterns of a-e, respectively. Single-headed black arrows on the silks label the positions where ED patterns were taken. Double-headed black arrows on the ED patterns indicate (002) diffraction spots and thus the c axis of HAP. Reproduced with permission from reference 16.

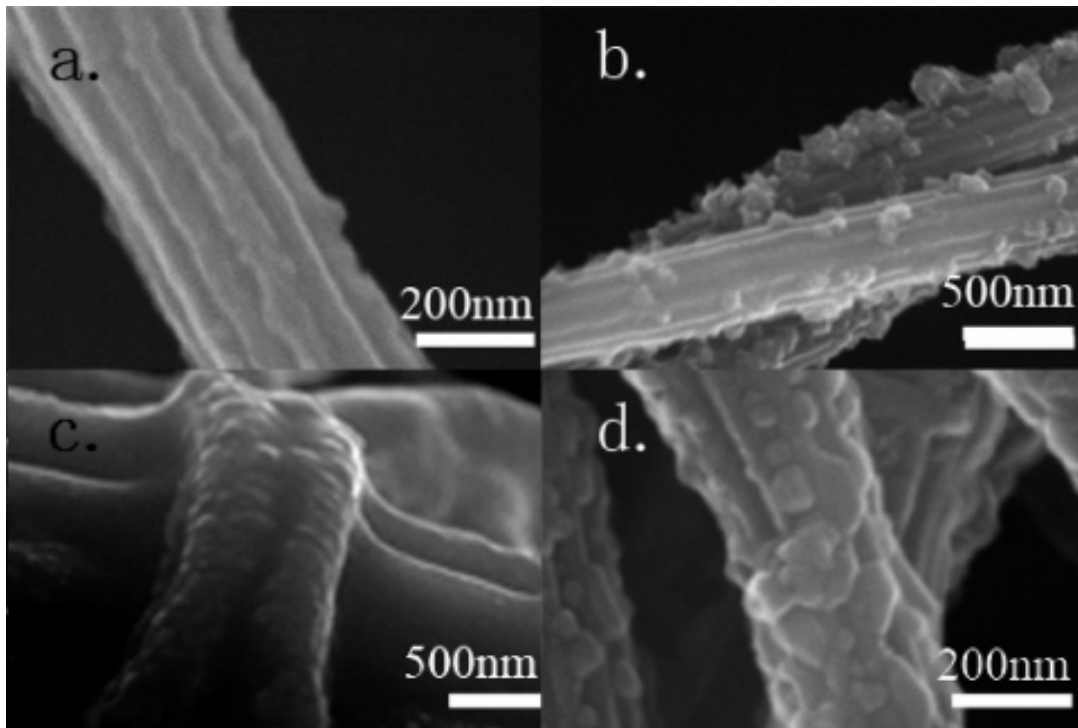


Figure 2.2 SEM Images of HAP on the spider silk.

(a) spider silk without HAP, (b) after 1 h of incubation, (c) after 4 h of incubation, and (d) after 16 h of incubation. Reproduced with permission from reference 16.

Table 2.1 Summary of Average Angles between the c Axis of HAP and the Long Axis of Spider Silk.

Time	1 h	4 h	16 h	10 days
Angle	69.6°	73.4°	78.4°	70.2°

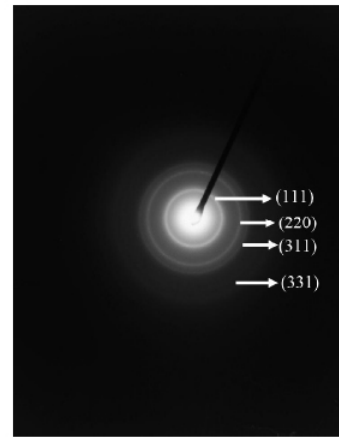
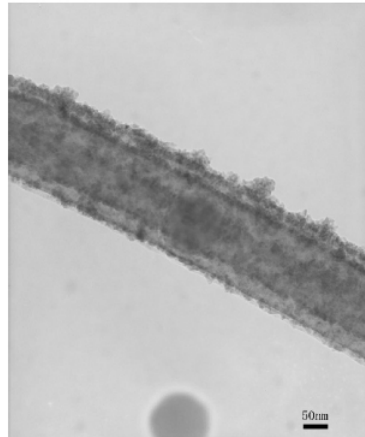
2.4. Discussion

To the best of our knowledge, this is the first report on the oriented growth of HAP on natural spider dragline silk, which is analogous to

biomineralization. We believe that crystal plane matching, stereochemistry matching, and the electrostatic interactions between HAP and silk proteins are the three dominant interfacial molecular recognition mechanisms that contribute to the oriented nucleation of HAP on the silks here. We found that other materials such as Au and CdS crystals could also be nucleated on the spider silk, but they did not have a preferred orientation (Figure 2.3).

This fact prompted us to analyze the mechanism of oriented nucleation of HAP on the silks on the basis of the unique features of the crystal structure of HAP as follows. Namely, the HAP crystal structure (hexagonal, $a=b=0.942$ nm, $c=0.688$ nm) has a lattice with its a-b plane matching b-c plane of silk protein nanocrystals (Figure 2.4), has Ca^{2+} ions that the β sheets (parallel to c-axis of protein nanocrystals) of the silk proteins can preferentially bind to, and has a chain (along c-axis of HAP) made of parallel O-H groups that can form directional hydrogen-bonding with C=O group (i.e., $=\text{O}\dots\text{H}-\text{O}$) of the β sheet of silk protein (Figure 2.4).

CdS



Au

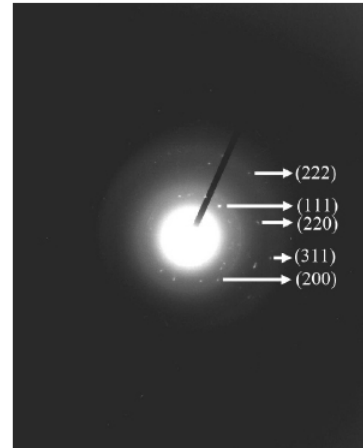
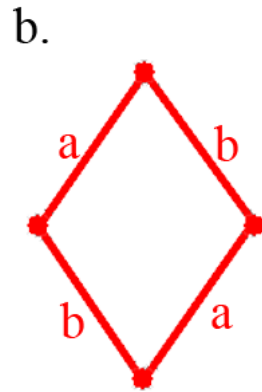
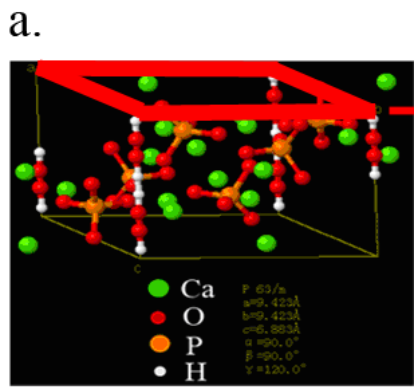
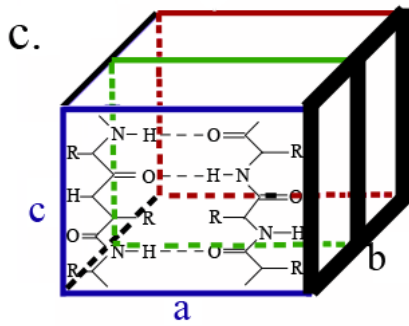


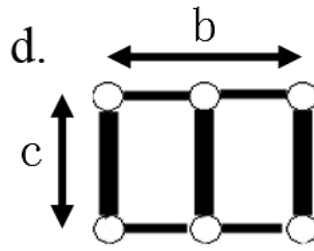
Figure 2.3 TEM image of spider silk coated by CdS crystals and gold crystals. The related ED patterns are also provided. Reproduced with permission from reference 16.



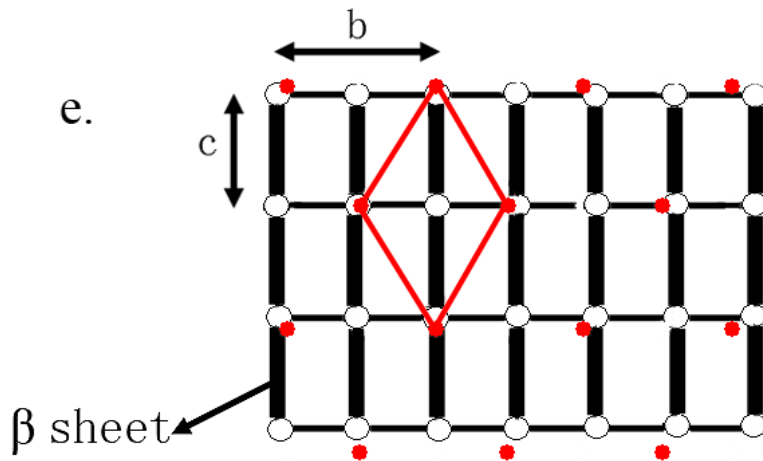
● O-H group in HAP



□ □ □ β sheets



○ C=O group in β sheets



◇ a-b plane of HAP

● C=O...H-O hydrogen bond

Figure 2.4 Lattice matching between the a-b plane of HAP and b-c plane of nanocrystallin domain of the spider silks, as well as hydrogen bonding between them. (a) The unit cell of HAP crystal structure, which belongs to a hexagonal crystal system. The highlighted plane (in red) in (a) is the a-b plane of HAP shown in (b). (c) Unit cell of nanocrystalline regions that are made of oriented β sheets in the spider silk. The highlighted (in black) plane in (c) is the b-c plane of silk proteins shown in in (d). (e) superimposition of the a-b plane of HAP (in red) and b-c plane of the silk protein (in black), indicating that the a-b plane of HAP and b-c plane of protein nanocrystals match each other approximately and that OH^- perpendicular to the a-b plane of HAP can form hydrogen bonding with the O in the C=O group (i.e., $=\text{O}\dots\text{H}-\text{O}$) of the β sheet of silk protein nanocrystals. Reproduced with permission from reference 16.

The protein nanocrystals assembled along the silk are composed of β sheets and have an orthogonal unit cell with the following lattice constants: $a=0.93$ nm, $b=1.04$ nm, $c=0.70$ nm (Figure 1.2), which are corresponding to the distance of β sheets repeat, interchain repeat within β sheets (consisting of two chains), and intrachain repeat (consisting of one dipeptide), respectively (Figure 2.4c) [22, 115]. Because of the preferred orientation of protein nanocrystals along spider silks (Figure 1.2d), the a-b plane of the protein nanocrystals are almost parallel to the cross-section of the silks, and thus is not exposed to the HAP solution, whereas the b-c plane of the silk is almost parallel to the silk length and

exposed on the silk surface [120], and thus can interact with HAP solution. We found that the a-b plane of HAP and b-c plane of protein nanocrystals match approximately (only about 7.5% mismatch) and can be bound to each other through hydrogen bonding between C=O groups from β sheets and H-O groups from HAP (Figure 2.4).

The hydroxyl group in the HAP nuclei can form hydrogen bonding with O in the C=O group (i.e., =O...H-O) of the β sheet of silk protein, which is perpendicular to the c-axis of protein nanocrystals in the silk (Figure 2.4). In order to verify this hydrogen-bonding, we performed Fourier transform infrared (FT-IR) spectroscopy on three samples: synthetic HAP crystals, spider silks, and the spider silks with HAP nucleated for 1 day on their coats. Figure 2.5 shows the FT-IR spectral regions of the three samples where characteristic IR absorption peaks due to hydrogen bonding are expected. From the FT-IR data, the peak of O-H stretching vibrations in HAP crystals is about 3427cm^{-1} and relatively narrower, which is consistent with the results published by Aaron Posner *et al.* [121]. However, the O-H stretching vibration peak of spider silks after

HAP is nucleated on the coats is shifted to about 3347cm^{-1} and becomes broader (Figure 2.5). This obvious shift of the O-H stretching vibration peak is due to the hydrogen bonding between spider silks and HAP crystals, which lowers the energy of O-H stretching vibrations in HAP [122]. These results confirm the formation of hydrogen bonds (i.e., $=\text{O}\dots\text{H}-\text{O}$) between HAP and spider silk protein during nucleation.

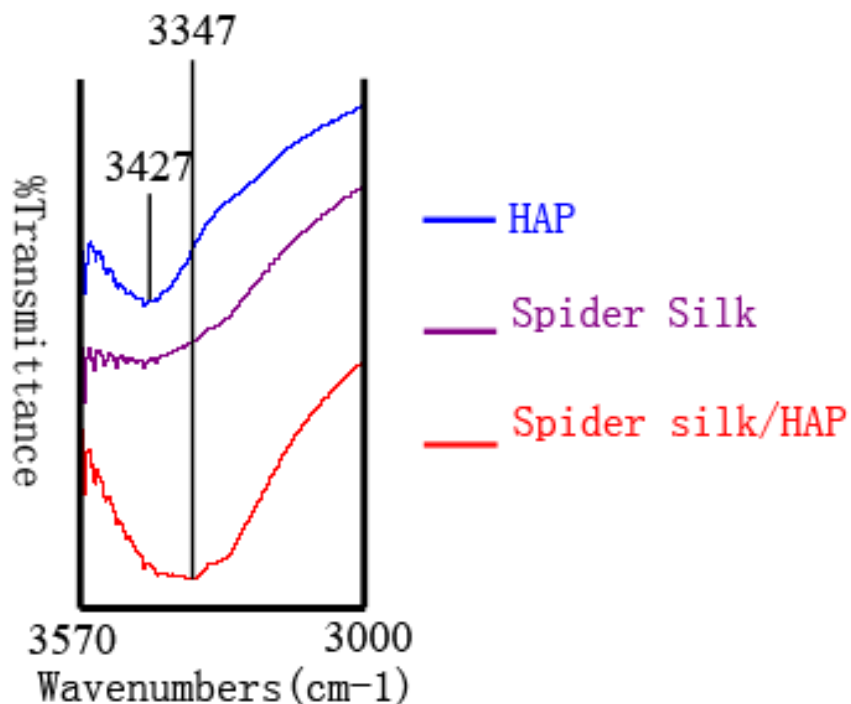


Figure 2.5 FT-IR spectra of O-H stretching vibrations of synthetic HAP crystals (blue), spider silk (purple), and silk/HAP (Red). The O-H peak is shifted to smaller wave number and becomes broader due to the hydrogen bonding between HAP and spider silks. Reproduced with permission from reference 16.

The O...H-O hydrogen bond is characteristic of linearity [123]. The directionality (linearity) of the hydrogen bonding indicates that the O-H group in HAP nuclei tends to be parallel to the C=O group in the protein at the interface (Figure 2.6). Namely, the O-H group in HAP nuclei will tend to be perpendicular to the *c* axis of the protein nanocrystals to satisfy the linearity of the hydrogen bonding. In addition, O-H groups have to be parallel to the *c* axis of HAP and organized into a chain along the *c* axis of a HAP crystal lattice, which is determined by the HAP crystal structure (Figure 2.4a). This constraint indicates that the orientation of the O-H groups of the nuclei will determine that of the *c* axis of the HAP [118]. Therefore, because of the formation of hydrogen bonds between HAP and silk proteins at the HAP/silk interface, the *c* axis of the HAP nuclei will have a tendency to be perpendicular to that of the spider silk, suggesting that the preferred orientation of the *c* axis of protein nanocrystals will determine that of HAP nucleated on the silk (Figure 2.6). Riekel et al. found that the protein nanocrystals of spider silks are preferentially oriented with their *c* axes distributed along the fiber axis with a 23° FWHM (Figure 1.2d) [22]. In fact, all of the spider silks have similar

nanocrystalline protein domains made of beta sheets. Thus, we use the 23° fwhm reported by Riek et al. to analyze the preferred orientation. A simple geometrical measurement reveals that the stereochemistry match based on hydrogen bonding will cause the *c* axis of HAP nuclei to form an angle in between 67° and 90° with respect to the long axis of spider silk (Figure 2.1f). This analysis is consistent with our finding that the *c* axis of HAP crystals on the spider silk is always at an angle of 69.9 to 78.4° with respect to the long axis of the spider silk at different times (Figure 2.1).

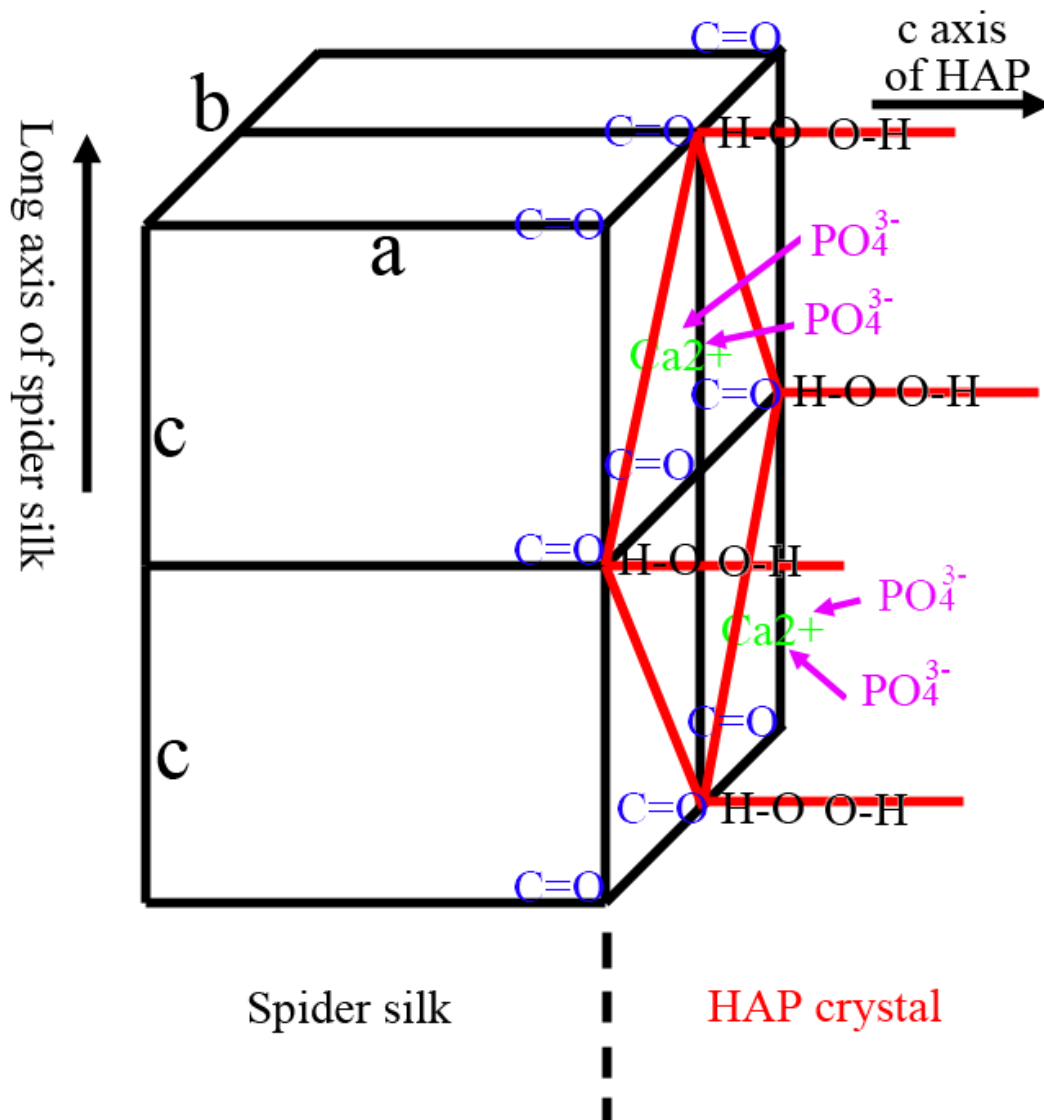


Figure 2.6 Proposed mechanisms of oriented nucleation of HAP on the spider silk, including crystal plane match between a-b plane of HAP and b-c plane of silk protein, stereochemistry match due to $\text{C}=\text{O}\cdots\text{H}-\text{O}$ hydrogen bonding and electrostatic interaction at the silk/HAP interface. Please note that (1) OH^- ions are parallel to c-axis of HAP and organized into a chain in HAP, (2) OH^- and Ca^{2+} can constitute an HAP a-b plane (Figure 2.4a), and (3) c-axis of silk protein is preferentially oriented along silk length direction with a 23° FWHM (Figure 1.2d). Reproduced with permission from reference 16.

Finally, the nanocrystalline domains of silk proteins that are made of oriented beta sheets can preferentially bind to Ca^{2+} ions, but amorphous domains do not. As a matter of fact, most beta sheets of proteins can bind to Ca^{2+} ions. Spider silk proteins have many glutamate amino acids, which have carboxyl groups as their side groups. Under our experimental conditions (pH between 6.59 and 7.01), these carboxyl groups are negatively charged and thus can electrostatically bind to Ca^{2+} . To determine if our spider silks can preferentially bind to Ca^{2+} ions from the HAP precursor solution, we conducted an energy-dispersive X-ray spectroscopy (EDS) study on the silks with and without being incubated in a 4 mM CaCl_2 solution, which has the same concentration of Ca^{2+} as the HAP precursor solution that we used for nucleation on the silks (Figure 2.7). This measurement can identify if calcium ions were attracted on the surface of spider silks. Our data clearly show that there are no obvious Ca peaks in untreated spider silks within the EDS detection limit. However, after the spider silks were incubated in the 4mM CaCl_2 solution, removed from the solution, thoroughly washed, and then dried at 80 °C, their EDS spectrum (Figure 2.7) shows a strong Ca peak but no Cl peaks, indicating

that our silks can preferentially bind to Ca^{2+} ions from the HAP precursor solution.

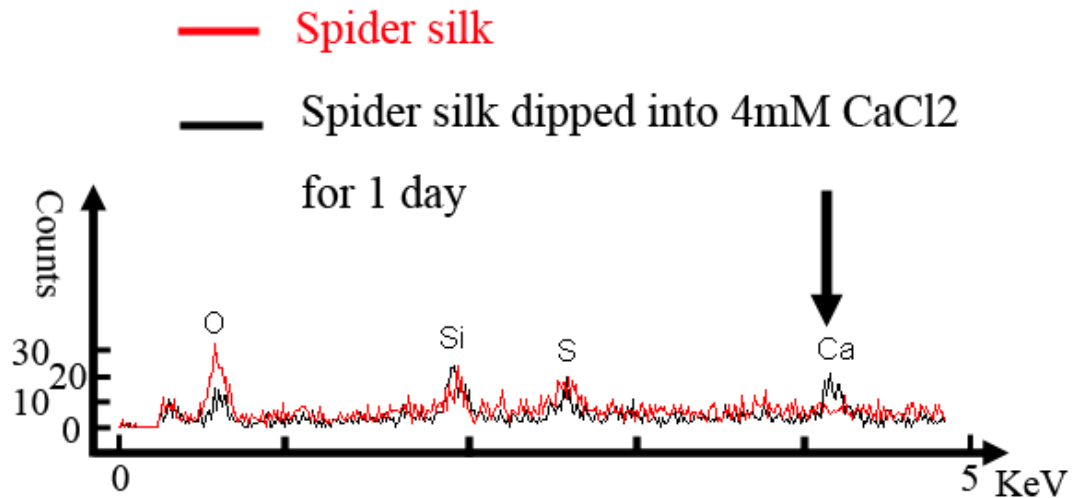


Figure 2.7 EDS spectra of spider silks (red) and spider silks aged in a 4mM CaCl_2 solution (black). There is an obvious Ca peak but no Cl peaks are observed on the latter, indicating the preferential binding of Ca^{2+} by the spider silks. Reproduced with permission from reference 16.

Once the Ca^{2+} ions are bound to the spider silk, PO_4^{3-} ions will be electrostatically attracted to the silk surface. This electrostatic effect, together with hydrogen bonding between the silk and OH^- ions, leads to an increase in the local concentration of HAP at the silk-solution interface (Figure 2.6). When the local inorganic ions are supersaturated, the hydrogen bond controls the direction of the c axis of HAP nuclei. In the meantime, Ca^{2+} and OH^- ions attracted to the silk surface are organized

into the *a-b* plane of HAP (Figure 2.4a), resulting in the oriented nucleation of HAP crystals along the silk (Figure 2.6).

2.5. Conclusion

The work presented in this chapter demonstrates that HAP crystals can be nucleated and grown on the natural spider dragline silk with a preferred orientation to form biomineralized silk. The resultant biomineralized silk may serve as a building block that can be assembled into a larger material that has the potential for application as a bone implant and tissue engineering scaffold. Our work also indicates that natural spider silk contains protein domains that can nucleate HAP and the beta sheets in the silk protein can induce the oriented nucleation of HAP crystals. We believe that the oriented growth of HAP is a result of silk protein-mediated nucleation dominated by crystal plane matching, stereochemistry matching, and electrostatic interactions.

Chapter 3 Identification of Microtubule-Binding Domains on Microtubule-Associated Proteins by Major Coat Phage Display Technique

3.1. Introduction

This work has been published as reference 179. Microtubule is a basic cellular component built by the self-assembly of α , β -tubulin subunits. This biopolymer is involved in a variety of cellular processes including mitosis, cytokinesis, and vesicular transport. It was found that the microtubules are stabilized by several kinds of proteins that bind to microtubules and these proteins are collectively called microtubule-associated proteins (MAPs). The MAPs play important roles in maintaining normal functions of the microtubules. Unusual structural changes of MAPs may lead to instability of the microtubules and cause diseases such as Alzheimer's disease [124]. Therefore, the study of interactions between microtubules and MAPs followed by the design of artificial drugs according to the interaction mechanism is a promising strategy to cure the diseases caused by abnormal actions of MAPs. 3-D structures of α , β -tubulins and

high resolution models of microtubules have already been published [125-129]. However, most MAPs do not have secondary structures or only have limited secondary structures. This fact is an advantage for using phage display technique to identify microtubule-binding domains on MAPs because the peptides displayed on phage in this work are unlikely to have secondary structure and may well mimic the binding properties of the protein segments on MAPs.

There are two main families of MAPs, MAP1 family and MAP2/Tau family. The MAP1 family includes MAP1A, MAP1B, and MAP1S, whereas the MAP2/Tau family includes MAP2, MAP4, and tau. A lot of work was focused on the tau structure and tau-microtubule interaction [130-137], but few structural details about MAP1 family proteins have been reported until now [138, 139]. Among the MAP1 family, MAP1A, MAP1B, and MAP1S all consist of a heavy chain and a light chain [140, 141]. All of the light chains can bind to the microtubules by themselves [140, 142, 143]. The heavy chain of MAP1A has microtubule-binding domains at 281-336 and 540-630 [144]. Self-similar region 2 (1307-1606) was proposed as one of the

binding domains of MAP1A heavy chain [145]. The heavy chain of MAP1B contains a domain (517-848), consisting of 21 repeats of a KKE motif, which can bind to the microtubules in vitro [146]. It also has another microtubule-binding domain located at one side of the basic repeat domain. So far, no microtubule-binding domains on the heavy chain of MAP1S have been reported. MAP2, MAP4, and tau proteins in the MAP2/tau family are natively unfolded molecules and all have a carboxyl-terminal microtubule-binding region and an amino-terminal projection region of varying sizes. Each microtubule-binding region of MAP2/tau family contains a proline-rich motif (PRM), a repeats domain, and a C-terminal domain (also called C-terminal tail domain). Repeats domain includes 3-4 conserved repeats and was reported as one of the microtubule-binding domains [147, 148]. Two flanking domains (including 20-30 amino acids) of the repeats domain are also considered as microtubule-binding domains. As for tau, it has been reported that it binds to microtubules in two ways: (1) tau binds to the outer surface of microtubules that are preassembled and stabilized by taxol [135, 136]; and (2) part of tau can bind to the interior wall of the microtubules if tau and

tubulin co-assemble in the absence of taxol [134]. It has been found that tau and taxol may have a competition or cooperation relationship [133] in the process of assembly. In vivo study also showed that taxol could induce rapid detachment of tau from the microtubules [137].

Phage display technology has matured to be a powerful tool in the postgenome era of biology to study protein-protein interaction. Although yeast two-hybrid analysis has been established for a long time, the successful application of phage display in the study of protein-protein interaction demonstrates that phage display is an alternative strategy for identifying the protein-ligand interaction sites [149, 150]. The principles of phage display have been reviewed elsewhere [44, 52], and the procedure we used in this work is summarized in Figure 3.1. In phage display, a phage-displayed random peptide library (also called phage library) is allowed to interact with a target (e.g., a protein), then the nonbinding phages are washed away from the target, leaving the binding phages bound to the target. The binding phages are then eluted from the target by changing the pH value or using an elution buffer and amplified by infecting

bacteria to form an enriched phage-displayed peptide population, which can be treated as a new library to interact with the target again. This process is called biopanning and usually repeated for several rounds to identify the peptides with binding affinity against the target. This is the principle of using phage display to identify a target-binding peptide (Figure 3.1). The most widely used phage library is a tip-displayed library, where billions of phage clones are present and a unique peptide is displayed at one specific tip (i.e., genetically fused to five copies of minor coat protein pIII) of filamentous M13 phage. Petrenko and Smith et al. developed a side-wall-displayed library called landscape phage library, where there are billions of fd-tet phage clones but each clone has one unique peptide displayed on the side wall (i.e., fused to each of the ~3900 copies of major coat protein called pVIII) of filamentous fd-tet phage (Figure 3.1) [45, 53, 151, 152].

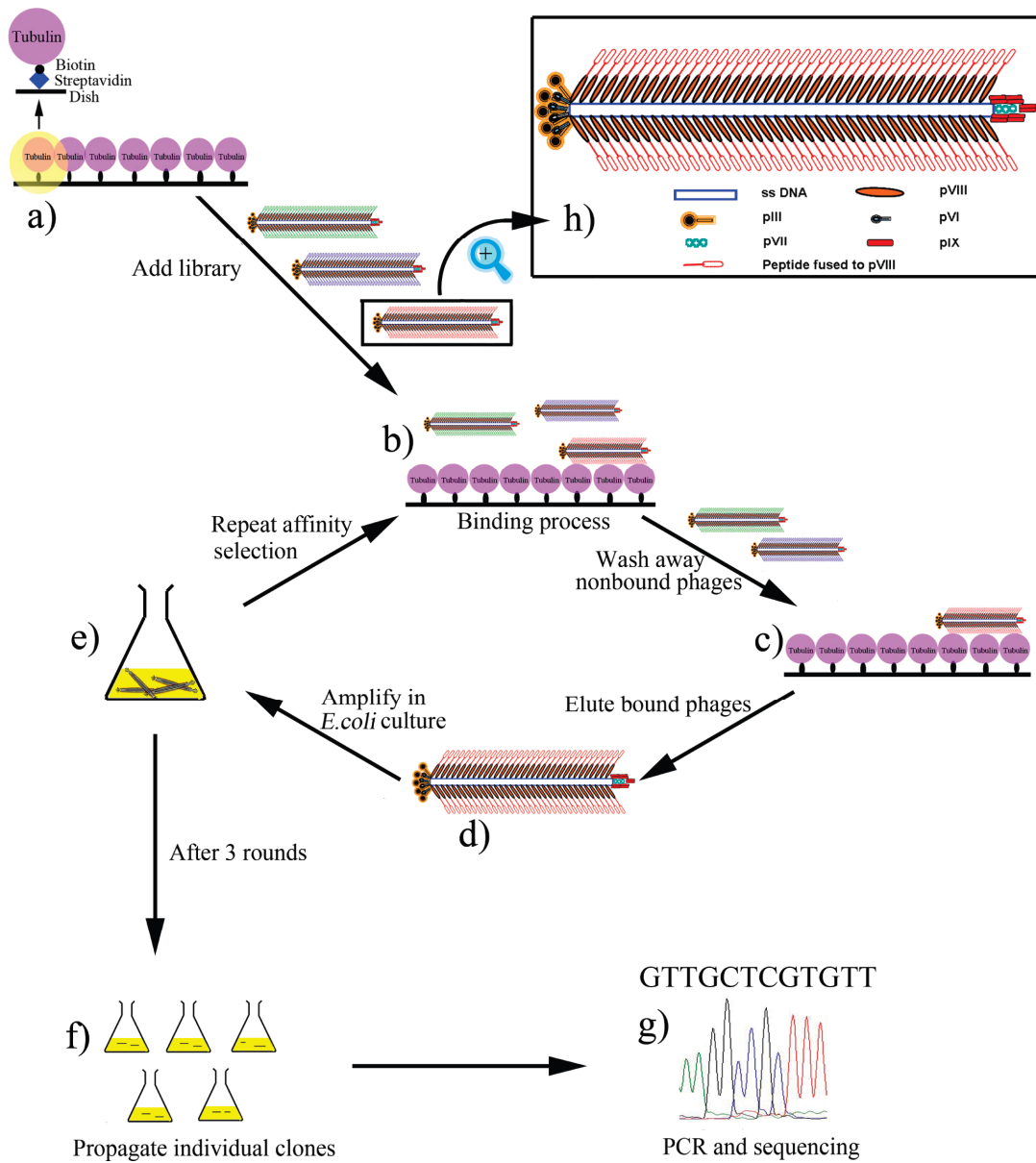


Figure 3.1 Procedure of selecting microtubule-binding peptides from landscape phage library (Biopanning). (a) Immobilization of biotin-labeled tubulins on a streptavidin-coated Petri dish; (b) some phages bind tubulins, while some do not after a landscape phage library is added to the Petri dish; (c) nonbinding phages are washed away and the binding phages are left on the dish; (d) the microtubule-binding phage is eluted from the dish by using an elution buffer; (e) the eluted phage is amplified by infecting bacteria *E. coli*; (f) amplified phage clones are propagated by PEG/NaCl precipitation and redissolved in TBS buffer (pH 7.0); (g) part of phage

genome (insert-coding region) is amplified by PCR and sequenced; (h) illustration of the structure of a single phage particle. Five copies each of pIII and pVI are at one tip, five copies each of pVII and pIX are at the other tip, and ~3900 copies of pVIII form a protein shell. A foreign peptide is fused to the solvent-exposed end of each of the ~3900 copies of pVIII which constitute the side walls of phage. Reproduced with permission from reference 179.

We chose to use landscape phage library instead of the widely used tip-displayed phage libraries to identify a peptide that can specifically bind to the microtubules for two main reasons: (1) The large periodic array of peptides presented on the side wall of the fd-tet phage may mimic the repeating units in some MAPs such as tau during the biopanning process; (2) Our future plan is to use tubulin-binding phage as a drug to interfere with the microtubule dynamics in vivo, so we need as many binding sites on the individual phage as possible. In addition, we chose purified tubulins instead of entire microtubules as a selection target during biopanning because (1) we do not want to exclude the possibility of binding peptides that can specifically interact with the inner wall of microtubule; (2) we want to explore the possibility of assembling free tubulins along the phage to form a microtubule-like nanostructure; and (3) our future plan, where tubulin-binding phage will be introduced into cells as a drug to interfere

with the microtubule assembly in vivo is based on the interaction between phage and free tubulins.

3.2. Methods and Experiments

3.2.1. Materials

A 9-mer landscape phage library (called f8/9) was constructed and provided by Dr. Valery Petrenko at Auburn University and the construction details were described in the literature [53]. The landscape phage library consists of billions of phage clones with each phage clone displaying a unique nine amino acid random peptide on each of the ~3900 copies of the major coat proteins (pVIII). The concentration of phage in our library is 1.4×10^{11} cfu/mL. Biotinlabeled tubulins from bovine brain were supplied in the form of a lyophilized powder from Cytoskeleton Inc. The tubulins received have been modified so that random surface lysines contain a covalently linked, long-chain biotin derivative. This long-chain biotin derivative not only allows the biotin molecules to be spaced far enough away from the tubulin protein so as not to interfere with its activity, but also enables the immobilization of the tubulins on the streptavidin-coated Petri

dish. In addition, the biotin-labeled tubulins can still be assembled into microtubules.

3.2.2. Fixation of Biotin-Labeled Tubulins onto a 35 mm Petri Dish.

A 35 mm Petri dish was coated with streptavidin by treating the dish with 400 μL /mL streptavidin in 0.1 M NaHCO_3 for 2 h at room temperature with the lid off. The remaining streptavidin solution was aspirated out. The Petri dish was then filled with a blocking solution (0.1 M NaHCO_3 , 5 mg/mL dialyzed BSA, 0.1 μg /mL streptavidin, 0.02% NaN_3) for 2 h at room temperature with the lid off. Then the blocking solution was removed from the Petri dish and the dish was washed five times with TBS/Tween solution (0.5% v/v Tween 20 in TBS solution). The desired amount of biotin-labeled tubulins (20 μg at first round, 4 μg at second round, and 0.3 μg at third round) was dissolved in 400 μL TTDBA (1 mg/mL BSA and 0.02% NaN_3 in TBS/Tween solution) and added to the Petri dish to react for 3 h at 4 $^\circ\text{C}$ to allow the immobilization of biotin-labeled tubulins on the Petri dish surface. The Petri dish was then washed for five times with TBS/Tween to remove unbound tubulins. A total of 400 μL of TTDBA was

mixed with 4 μL of 10 mM biotin and the mixture was added to the dish followed by rocking for 10 min at 4 $^{\circ}\text{C}$ to block the free biotin-binding sites on the streptavidin.

3.2.3. Affinity-Selection of Tubulin-Binding Phage Clones.

The standard biopanning procedure was followed with slight modification. The landscape phage library was added to the untreated dish for 1 h at 4 $^{\circ}\text{C}$ to remove the phages that specifically bound to the Petri dish. This process is called depletion. The resultant depleted library was then used as an input library and introduced into the tubulin-modified dish for affinity selection of tubulin-binding phage clones. The dish was rocked for 12 h at 4 $^{\circ}\text{C}$. It was then washed for ten times with TBS/Tween solution to remove the unbound phages. The bound phages were eluted from the dish with 400 μL of elution buffer (0.1 N HCl, 1 mg/mL BSA, and pH adjusted to 2.2 with glycine) for 10 min on a rocker. The eluate was transferred to a microtube and neutralized by mixing it with 75 μL of 1 M Tris-HCl (pH =9.1) immediately.

3.2.4. Preparation of Starved Cells.

A fresh loop of *E. coli* K91 BlueKan cells (anti-kanamycin) was inoculated into two tubes containing 2 mL of NZY/Kanamycin (100 $\mu\text{L}/\text{mL}$) in each tube. The tubes were incubated in a shaking incubator at 220 rpm at 37 $^{\circ}\text{C}$ overnight. A total of 300 μL of overnight cultures were transferred into a 300 mL flask containing 20 mL of NZY broth. The flask was incubated first at 220 rpm, 37 $^{\circ}\text{C}$ until $\text{OD}_{600}=0.45$, and then for an additional 8 min with gentle shaking (50 rpm). The cells in the sterile tube were then centrifuged at 2000 g for 10 min at 4 $^{\circ}\text{C}$. The supernatant was discarded and the cells were gently resuspended in 20 mL of 80 mM NaCl solution. The resuspended solution was then gently shaken at 50 rpm for 45 min, followed by centrifugation as above. The cell pellet was resuspended in 1 mL cold NAP buffer (80 mM NaCl, 50 mM $\text{NH}_4\text{H}_2\text{PO}_4$, pH = 7.0) and stored in a refrigerator.

3.2.5. Amplification of Eluates.

The entire first-round eluate (475 μL) was concentrated to reach a final volume of 100 μL by using a Centricon 50-KDa Ultrafilter (Amicon). A

total of 100 μL of the concentrated eluate was mixed with 100 μL of the starved cells and incubated for 15 min at room temperature. Because phage gene contains anti-tetracycline part, so tetracycline can be used to kill un-infected *E.coli* cells. The phage-infected cells were transferred to 40 mL of NZY with tetracycline (0.2 $\mu\text{g}/\text{ml}$) in a 125 mL flask and incubated for 45 min at 37 $^{\circ}\text{C}$ with shaking. The tetracycline concentration was increased to 20 $\mu\text{g}/\text{mL}$ and the flask continued to be shaken at 37 $^{\circ}\text{C}$ for 24 h.

3.2.6. Purification of Amplified Phages by Using Double PEG

Precipitation.

The cell culture was centrifuged at 3000 g for 10 min at 4 $^{\circ}\text{C}$. The supernatant was poured into another fresh tube and centrifuged again at 12000 g for 10 min at 4 $^{\circ}\text{C}$. The supernatant was poured into a fresh tube, to which 6 mL of PEG/NaCl solution (100 g PEG 8000, 116.9 g NaCl, and 475 mL water) was then added. The tube was kept at 4 $^{\circ}\text{C}$ overnight for precipitation. The precipitated phages were collected by centrifuging at 31000 g for 15 min and the supernatant was removed. The pellet was

dissolved in 1 mL of TBS in a microcentrifuge tube and centrifuged again at 12000 g for 2 min to remove any undissolved material. A total of 150 μ L of PEG/NaCl solution was added to the supernatant and kept on ice overnight. The tube was then centrifuged at 12000 g at 4 $^{\circ}$ C for 10 min and the supernatant was removed. The pellet was dissolved in 200 μ L of TBS by vortexing.

3.2.7. Titering of Phage.

Serial dilutions (10^{-2} ~ 10^{-8} pfu/ml) of phage were prepared by diluting phages with TBS/gelatin buffer (0.1 g gelatin in 100 mL TBS buffer). A total of 10 μ L of starved cells were mixed with 10 μ L of each dilution in the Eppendorf tubes and incubated for 15 min at room temperature. NZY (180 μ L) with tetracycline (0.2 μ g/mL) was added to each tube and the tube was incubated for 45 min at 37 $^{\circ}$ C. Suspensions from the tubes were spread onto NZY plates with tetracycline (20 μ g/mL). The plates were incubated overnight at 37 $^{\circ}$ C in an incubator and the number of colonies on the plates was counted in the following morning.

The titer was calculated by the following formula: $\text{titer} = N \times 100 \times \text{dilution factor}$, where N is the number of the colonies on a plate.

3.2.8. Second and Third Round of Affinity Selection.

The purified phage was used as a new input library and the selection procedure as the first round was repeated. After the third round of selection, the eluted phage was not amplified. Instead, the neutralized eluates were titered and 150 colonies were picked up for sequencing to determine the tubulin-binding peptides that are fused to the major coat of the affinity-selected phage.

3.2.9. Sequencing of Selected Phage Colonies.

Each colony of phage (anti-tetracycline) infected *E. coli* K91 BlueKan cells on the plates was inoculated into a tube containing 2 mL of NZY/tetracycline (20 $\mu\text{g}/\text{mL}$) and the tube was incubated in the shaking incubator at 220 rpm, 37 °C overnight. A total of 1 mL of culture from each tube of phage infected K91 BlueKan cells and 30 μL of 830 μM related primer (5' -CAAAGCCTCCGTAGCCGTTG-3') were sent to MC Laboratory

Inc. for sequencing. A total of 1 mL of culture was mixed evenly with 250 μ L of glycerol and stored at -80 $^{\circ}$ C.

3.2.10. Interaction between Tubulin-Selected Phage and Free Tubulins

Characterized by Transmission Electron Microscopy (TEM).

A total of 20 μ L of phage infected *E. coli* K91 BlueKan cells was transferred into a tube with 4 mL of NZY/tetracycline (20 μ g/mL), followed by shaking overnight at 37 $^{\circ}$ C. Culture (4 mL) was transferred into 1 L of NZY/tetracycline (20 μ g/mL) in a 2.5 L flask, incubated for 12 h at 37 $^{\circ}$ C with shaking, and purified by double PEG precipitation. Purified phage solution (100 μ L; OD₂₇₀ = 0.3) was mixed with 2 μ L of 10 mg/mL purified tubulin solution, and the mixture was incubated at 4 $^{\circ}$ C for 12 h. A total of 5 μ L of the mixed solution was placed on the Formvar and carbon coated copper grid for 30 s, rinsed by 10 drops of distilled water, stained with 1% uranyl acetate twice, and observed under TEM (Zeiss 10). The wild-type phage was used as a control.

3.3. Results and Discussion

3.3.1. Identification of Affinity-Selected Peptides by Biopanning.

The landscape phage library was incubated with tubulins immobilized on the Petri dish to allow retention of tubulin-binding phages during washes. Affinity-selected phages were then eluted. The selection procedure was repeated for three rounds. Titers of phage were increased over three successive rounds of biopanning from 1.9×10^5 cfu/mL (round one) to 4.4×10^6 cfu/mL (round two) and to 3.7×10^7 cfu/mL (round three). After the third round biopanning of the landscape library, 143 phage clones were isolated and sent for sequencing. From these 143 clones, 87 unique sequences were obtained (Table 3.1). Among them, four sequences have the highest frequency: ADTVSGAMV (7), VARVGSPPD (7), VAVVGTFPD (5), and VSTPGSPDD (5).

Table 3.1 Selected peptide sequences and frequency. Reproduced with permission from reference 179.

ADTVSGAMV	7
VARVGSPPD	7
VAVVGTFPD	5
VSTPGSPDD	5
ASYQDLGSS	4
AEMVKSSID	4
DFVTRSPQD	4
EWDPAPAME	4
ARGGEGTED	3
DNGSLANGE	3
DRRDDAVSE	3
ENARSVNDD	3
EYSAPSADA	3
GDYQSLVED	3
GMNNASFPD	3
GSPSEYSSQ	3
VPQTSLAME	3
EGGGGLIND	2
ESGGSGSTE	2
GETLDPSLE	2
GGTESMTAS	2
VFLGDPSVE	2
VSATLEPVD	2
ADGSPDLPA	
AEGGLEHLD	
AEYAFGGTD	
AFGAQEDNT	
AFNATASMS	
AGSNINLVD	
AHMSEVEGG	
AIRDIAGDS	
AITASDSMS	
ANRVSEMTE	
ANSISFDDD	
APDSSAWS	
APNLSISDS	
APTVEADNN	
AQDLAVITG	
AQYETSYPE	
ASSHFDGSD	
AYESGTGSS	
DEHMEGNAG	
DGFADLASD	
DGRPSDIPT	
DGVADAASN	
DSGGSGIAS	
DVSGAFMAD	
EAGPIPGDG	
EDISLSMGE	
EDYPDISVG	
EETMNGMPM	
EFNDGSGVD	
EETMNGMPM	
EHELDPVMA	
EIGGMGAGG	
EMERSSSMA	
ENPVLASDS	
ESSTQDFPD	
EWVDPRGED	
EYSSSELPP	
GATHEVGGD	
GDLVQDVTA	
GESSGGADD	
GGDFAAANG	
GLRGEVEEG	
GMQAGDQDD	
GPVEGDADG	
GSDSDLTFD	
GSGGAENV	
GSLDDITDN	
GSRDGVISE	
VEGQGSVSD	
VGDAGHSME	
VGEGYREES	
VGRDSTLND	
VGTDSDNAG	
VLDSVSSPD	
VLPVGAGTD	
VNENQLVMD	
VNVTDAGID	
VPAAYIGND	
VTANPDSSA	
VTMFESNAD	
VTNDPSLDD	
VVNQGDPPD	
VVRDPGVSG	
VYQNSESTL	

3.3.2. Global Characterization of Affinity-Selected Peptides.

Selected peptides were analyzed by using the receptor ligand contacts (RELIC) suite of programs, which is a bioinformatics tool for combinatorial peptide analysis and identification of protein-ligand interaction sites [153]. RELIC can evaluate the statistical properties of a collection of peptides and has been shown to be particularly suitable for analyzing the peptide populations affinity-selected by phage display [153]. It can be used to identify most likely protein-ligand interaction sites on the basis of affinity-selected peptides. A thorough review of RELIC and its principle as well as its application in analyzing peptides affinity-selected by phage display can be found in the literature. We used two RELIC programs (RELIC/POPDIV and RELIC/INFO) to confirm that our affinity-selected peptides show tubulin-binding affinity, which resulted from the biopanning of landscape phage library against tubulins immobilized on the Petri dish.

The decreasing of the diversity of the sequences obtained from iterative rounds of selection is an indicator of affinity selection [149, 154,

155]. RELIC/POPVID program uses a statistical sampling method to estimate the sequence diversity of a combinatorial peptide library based on the sequences obtained from a limited number of randomly sampled members of the library. Specifically, for peptides with M amino acids in length, diversity (d) is defined as:

$$d = 1/(20^M \prod_i (\sum_j p_{ij}^2))$$

p_{ij} is defined as the probability of amino acid j occurring at position i in the peptide [154]. Selected peptides with the binding affinity against the immobilized target should have a diversity value lower than an equivalent number of randomly selected peptides from the initial library. We calculated the diversities of both affinity-selected peptides and random peptides selected from the initial parent library by using the RELIC/POPVID program. Our affinity selected peptides yielded a diversity value of 0.001734 ± 0.000808 , whereas the 100 randomly selected peptides from the initial parent library yielded a diversity value of 0.011612 ± 0.007429 . Compared to randomly selected peptides, our affinity-selected peptides clearly have a less diversified population. This fact is an

evidence for the successful selection of peptides with binding affinity against immobilized tubulins during the biopanning process according to the principle of RELIC/POPVID program [153].

The original peptide sequence diversity and distribution pattern within a library could be distorted during either rounds of affinity selection or broth amplification. In order to make sure that this distortion is from affinity selection but not from broth amplification, we need to exclude the noise generated by broth amplification. The noise from amplification results from the filtering effects of the various life cycle stages of the phage vector and has a regular and measurable pattern [155-157]. RELIC/INFO program was designed to first calculate the noise pattern and then subtract the noise pattern from the affinity caused pattern to obtain information content on the basis of information theory. In this program, a concept of information content is introduced and defined as $-\ln(P_N)$, where P_N is the probability of randomly observing a given peptide and can be calculated by multiplying the probability of each amino acid occurring at each position within the peptide along the length of the sequence.

Therefore, a larger information content (i.e., larger $-\ln P_N$) of a peptide, resulting from a smaller probability of random occurrence of this peptide (i.e., smaller P_N), indicates a greater chance of observing this peptide in the affinity-selected pool due to the specific binding to the target (signal) as opposed to positive growth characteristics (noise). Hence, a positive shift in the normalized distribution of information content of a collection of affinity-selected peptides compared to randomly selected peptides will be expected if the selected peptides have binding affinity against the target during biopanning and can be used to confirm that the decreasing of diversity (i.e., enrichment of selected peptides) is due to affinity binding instead of amplification noise. This is the principle of using RELIC/INFO program to determine the occurrence of the information content of the affinity-selected peptides and thereby confirm the binding affinity of the selected peptides after biopanning process in phage display. By using the RELIC/INFO program, we obtained the normalized distribution of information content for both random peptides selected from the parent phage library and the affinity-selected peptides after biopanning (Figure 3.2). Indeed, the normalized distribution of the information content for our

tubulin-selected peptides is positively shifted toward higher information content in comparison to that for the peptides randomly selected from the parent phage library (Figure 3.2). This positive shift of the curve suggests that our tubulin-selected peptides result from affinity selection instead of from amplification noise, namely, the affinity-selected peptides do have binding affinity against tubulins [149, 153].

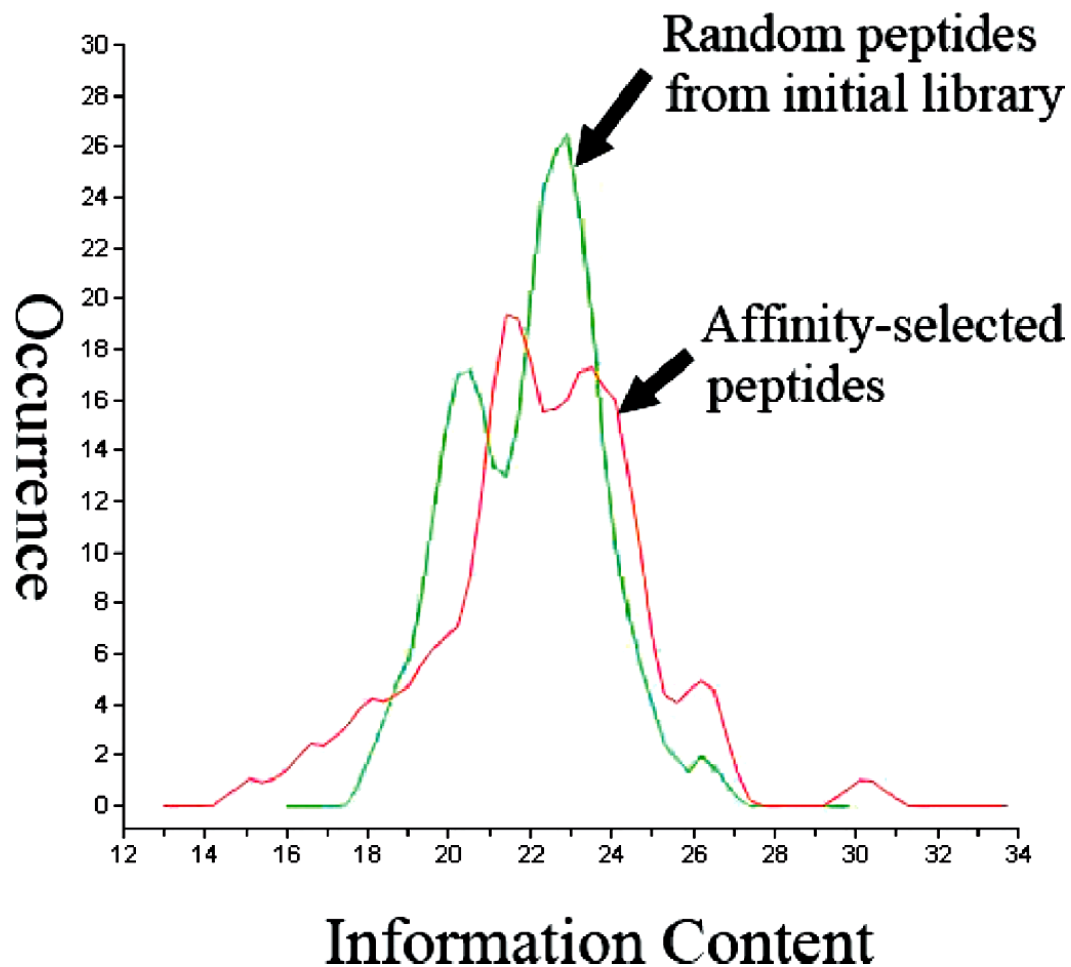


Figure 3.2 Normalized distribution of information content for two peptide populations calculated by using RELIC/INFO program.

The green curve is corresponding to the peptides randomly selected from the parent library, and the red curve is corresponding to the peptides affinity-selected from the library through phage display technique, which are listed in Table 3.1. A shift toward higher information content (i.e., red vs green curve) is observed for the affinity-selected peptides compared to the randomly selected peptides. Reproduced with permission from reference 179.

For any selected peptide, information content will be considered first. High information content indicates a greater chance of observing this peptide in the affinity-selected pool due to the specific binding to the target (signal) as opposed to positive growth characteristics (noise). Then the frequency will be considered. High frequency means high binding affinity. These selected peptides have a higher frequency (≥ 4): ADTVSGAMV (7 (= frequency), 24.304 (= information content)), VARVGSPPD (7, 24.981), VSTPGSPDD (5, 21.377), VAVVGTFFPD (5, 22.881), ASYQDLGSS (4, 24.199), DFVTRSPQD (4, 26.105), AEMVKSSID (4, 23.169), and EWDPAPAME (4, 22.030). They all have relatively high information content. So we believe that they are from affinity selection and have high binding affinity against tubulins (information content of each sequence is listed in Table 3.2).

Table 3.2 The information content of each peptide.

Peptide	Probability (P_N) of random sequence	Information ($-\ln P_N$)
APTVEADNN	7.3691E-14	30.239
AFGAQEDNT	2.9845E-12	26.538
VPAAYIGND	3.3161E-12	26.432
EHELDPVMA	3.3161E-12	26.432
DFVTRSPQD	4.5983E-12	26.105
AITASDSMS	5.3058E-12	25.962
VNENQLVMD	7.9587E-12	25.557
GPVEGDADG	1.2970E-11	25.068
VARVGSPPD	1.4149E-11	24.981
VLPVGAGTD	1.7686E-11	24.758
DGVADAASN	2.1124E-11	24.581
GSLDDITDN	2.1886E-11	24.545
GDLVQDVTA	2.6264E-11	24.363
ADTVSGAMV	2.7855E-11	24.304
ASYQDLGSS	3.0950E-11	24.199
AFNATASMS	3.0950E-11	24.199
ANSISFDDD	3.1835E-11	24.170
EETMNGMPM	3.3702E-11	24.113
ADGSPDLPA	3.5814E-11	24.053
VEGQGSVSD	3.7140E-11	24.016
VTANPDSSA	3.7140E-11	24.016
ARGGEGTED	4.1783E-11	23.899
VPQTSLAME	4.2446E-11	23.883
ENPVLASDS	5.6595E-11	23.595
VVNQGDPPD	6.1901E-11	23.505
VSATLEPVD	6.3669E-11	23.477
GLRGEVEEG	7.0036E-11	23.382
GMQAGDQDD	7.0036E-11	23.382
EFNDGSGVD	7.3691E-11	23.331
DRRDDAVSE	8.0471E-11	23.243
GGDFAAANG	8.1709E-11	23.228
EYSAPSADA	8.4892E-11	23.190
AEMVKSSID	8.6661E-11	23.169
APNLSISDS	8.8430E-11	23.149
GDYQSLVED	1.0505E-10	22.977
VAVVGTFPD	1.1555E-10	22.881

VGTDSDNDAG	1.2380E-10	22.812
VTNDPSLDD	1.3264E-10	22.743
EIGGMGAGG	1.3928E-10	22.695
AYESGTGSS	1.6507E-10	22.525
ANRVSEMTE	1.7332E-10	22.476
DNGSLANGE	1.8393E-10	22.416
GGTESMTAS	2.0427E-10	22.312
VNVTDAGID	2.1665E-10	22.253
AIRDIAGDS	2.4073E-10	22.147
EWVDPRGED	2.7082E-10	22.030
VGRDSTLND	2.7855E-10	22.001
GETLDPSLE	2.9182E-10	21.955
GSGGAENVS	3.1516E-10	21.878
AQYETSYPE	3.3702E-10	21.811
VTMFESNAD	3.4664E-10	21.783
GSPSEYSSQ	3.6769E-10	21.724
AEYAFGGTD	3.7914E-10	21.693
GSDSDLTFD	4.2022E-10	21.590
DGFADLASD	5.0697E-10	21.403
VSTPGSPDD	5.1997E-10	21.377
EWDPAPEME	5.1997E-10	21.377
ENARSVNDD	5.1997E-10	21.377
EMERSSSMA	5.1997E-10	21.377
VFLGDPSVE	5.7302E-10	21.280
VYQNSESTL	5.7302E-10	21.280
GATHEVGGD	5.9579E-10	21.241
AHMSEVEGG	6.4996E-10	21.154
VLDSVSSPD	6.7914E-10	21.110
VVRDPGVSG	7.5828E-10	21.000
EYSSSELPP	7.6403E-10	20.992
VGDAGHSME	7.9233E-10	20.956
GMNNASFPD	1.0724E-09	20.653
GESSGGADD	1.3073E-09	20.455
EDYPDISVG	1.5599E-09	20.279
ESGGSGSTE	2.0056E-09	20.027
ESSTQDFPD	2.0799E-09	19.991
DEHMEGNAG	2.1030E-09	19.980
AGSNINLVD	3.6398E-09	19.431
APDSSAWSD	3.6398E-09	19.431
VGEGYREES	3.6398E-09	19.431
AEGGLEHLD	5.8496E-09	18.957
GSRDGVISE	6.6729E-09	18.825

AQDLAVITG	1.0616E-08	18.361
DGRPSDIPT	1.2881E-08	18.168
EGGGGLIND	1.6379E-08	17.927
EAGPIPGDG	2.1232E-08	17.668
DSGGSGIAS	3.1939E-08	17.259
DVSGAFMAD	6.3878E-08	16.566
ASSHFDGSD	7.4312E-08	16.415
EDISLSMGE	2.5478E-07	15.183

3.3.3. Identification of Potential Microtubule-Binding Domains on

MAPs.

There are two main families of MAPs: MAP1 family and MAP2/tau family. MAP1 family proteins are classic MAPs that bind along the microtubules. They include three family members, MAP1A, MAP1B, and MAP1S. All of the three proteins contain heavy and light chains. The light chains of all these three proteins and heavy chains of two proteins (MAP1A and MAP1B) can bind to microtubules [139, 140, 142-145, 158]. MAP2/tau family is the other classic MAPs family that binds along the microtubules. They include three family members, MAP2, tau, and MAP4. All of these three proteins contain a projection region and a microtubule-binding region. The microtubule-binding regions of the MAP2/tau family

proteins all contain a PRM, a repeats domain, and a carboxyl-terminal domain.

Here, we use RELIC/MATCH program to align our affinity-selected peptides with MAPs to identify potential microtubule-binding domains. This RELIC/MATCH program works as follows. The program works as follows: The first selected peptide is lined up against the protein sequence at residue 1. Each residue of the protein is given a modified BLOSUM62 score. The peptide is then realigned with the protein at residue 2. A second set of scores is calculated for each of the protein residues. The peptide is then realigned at protein residue 3, rescored, and then at protein residue 4, *etc.* until the first peptide sequence is aligned with the protein sequence at the C-terminal of the protein. This same process is subsequently performed for each peptide in the selected peptides. The software programs then tally the cumulative score for each amino acid using the alignments above the cut-off value. If there is a significant fraction of peptides within the input sequences which exhibit high similarity, these peptides will cluster underneath that region of the protein in the

alignment output. The cumulative score values for those residues will be high [153].

We aligned affinity-selected peptides with the whole sequences of MAP1A, MAP1B, and MAP1S and plotted similarity score of each amino acid versus amino acid position to identify potential microtubule-binding domains separately by using the RELIC/MATCH program (Figure 3.3). In Figure 3.3, we set a cutoff value of similarity score 15 and identified potential microtubule-binding domains on MAP1 family proteins with higher similarity scores. Figure 3.3 shows that domains 527-537, 970-990, 1058-1064, 1292-1315, 1877-1900, 2390-2410, and 2653-2671 on MAP1A, discontinuous domains from 830 to 2122 on MAP1B, and domains 682-697 on MAP1S are potential microtubule-binding domains according to the similarity mapping carried out by RELIC/MATCH program. These potential microtubule-binding domains are listed in Table 3.3. In Table 3.3, we indicate which domains identified in this work are in agreement with the microtubule-binding domains reported previously and which ones are novel potential microtubule-binding domains identified by this work. How

these domains are aligned with MAP1A, MAP1B, and MAP1S are shown in Figure 3.4-3.6 respectively.

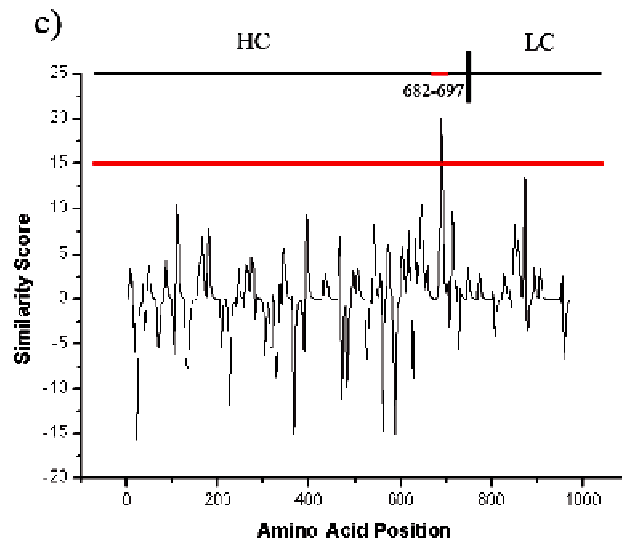
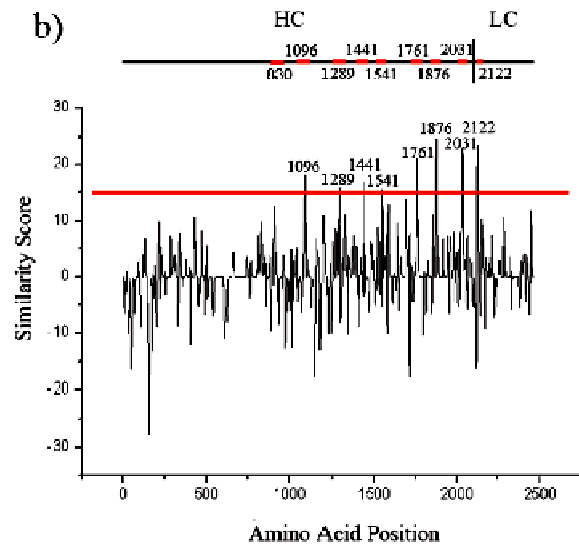
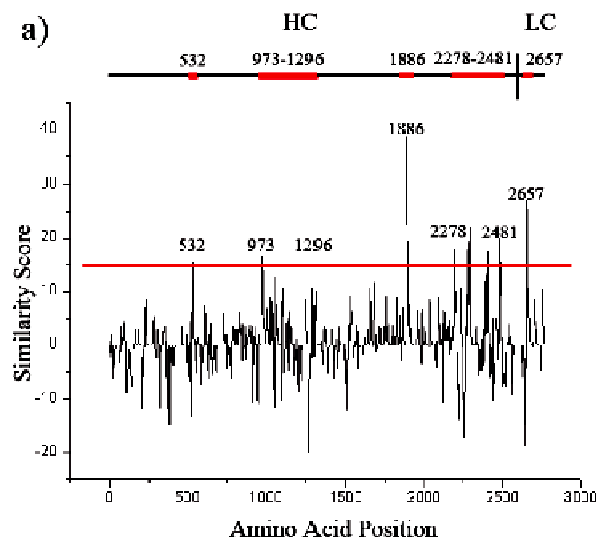


Figure 3.3 Cumulative similarity score of each amino acid in the sequences of proteins of the MAP1 family. (a) MAP1A, (b) MAP1B, and (c) MAP1S. The scores are calculated by using RELIC/MATCH program. Red line indicates a cutoff value of similarity score to identify potential microtubule-binding domains. HC: heavy chain of MAP1 proteins. LC: light chain of MAP1 proteins. The amino acid positions associated with the peaks with similarity scores above the cutoff value are indicated and the corresponding domains are highlighted by red lines. Reproduced with permission from reference 179.

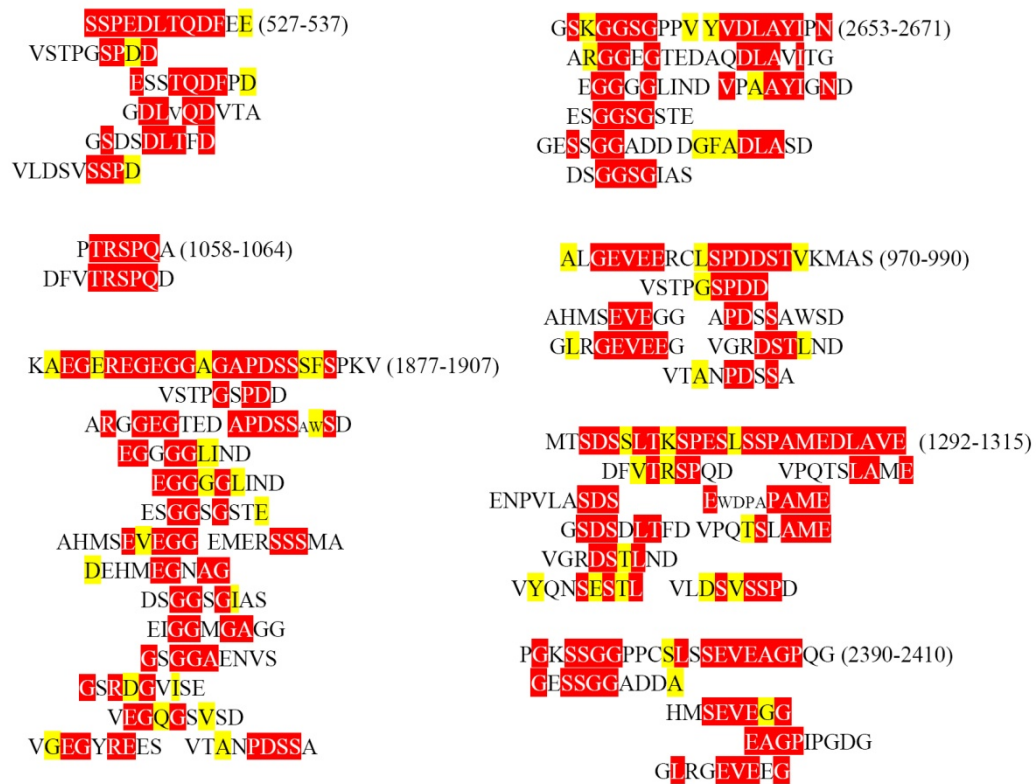


Figure 3.4 Alignments of selected peptides with MAP1A. Reproduced with permission from reference 179.

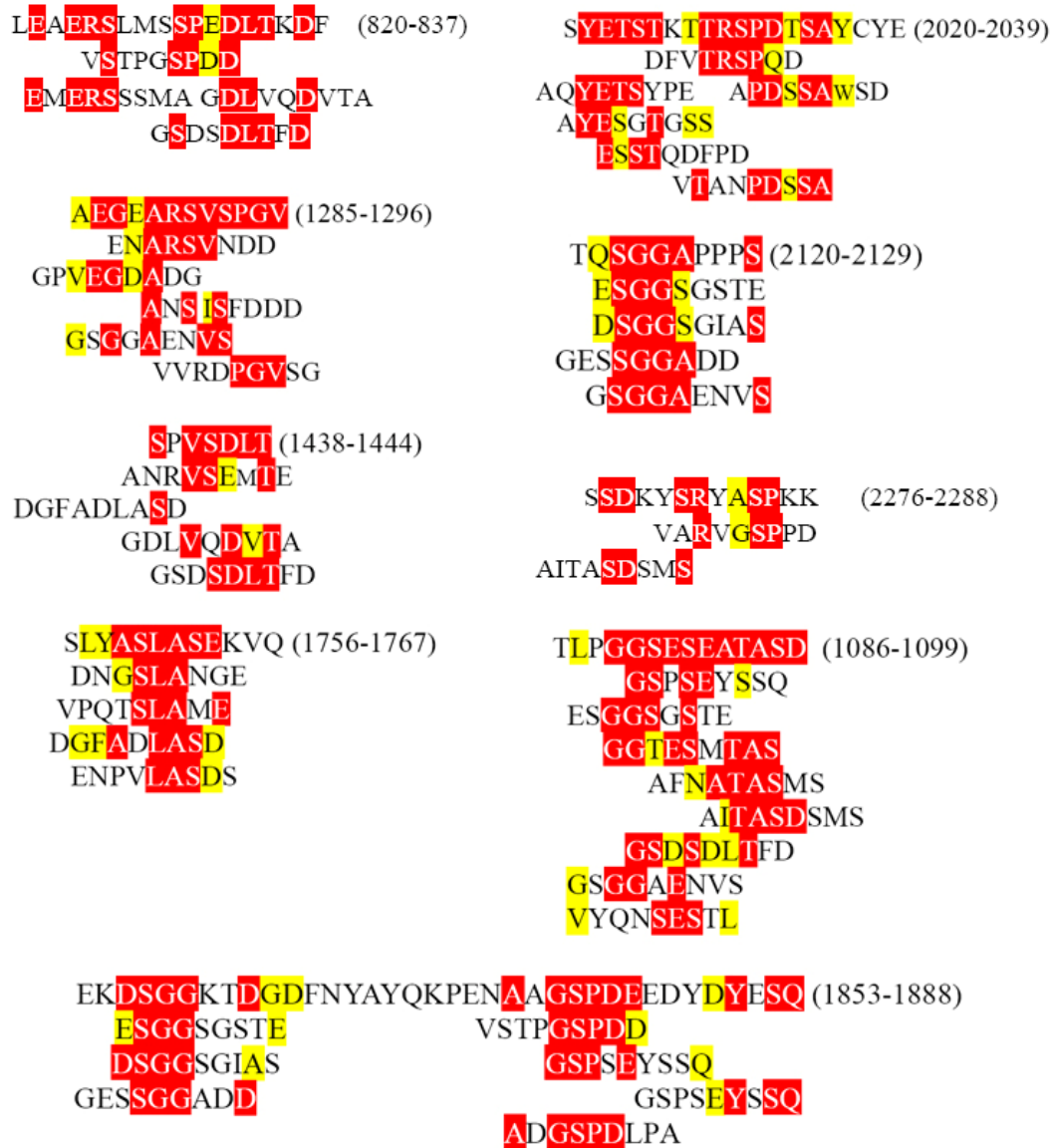


Figure 3.5 Alignments of selected peptides with MAP1B. Reproduced with permission from reference 179.

PASPGSSDSSARSQER (682-697)
 VSTPGSPDD
 ENARSVNDD
 APDSSAWSD
 VTANPDSSA

Figure 3.6 Alignments of selected peptides with MAP1S. Reproduced with permission from reference 179.

Similarly, we aligned our affinity-selected peptides with the sequences of the microtubule-binding regions of MAP2, tau, and MAP4 (Figures 3.7, 3.8, and 3.9) and plotted the similarity score of each amino acid versus amino acid position to identify potential microtubule-binding domains in the microtubule binding regions (Figure 3.10). Domains 1614-1635 and 1812-1857 on MAP2, domains 218-230 and 429-437 on tau, and domains 687-697, 738-769, 870-883, and 985-994 on MAP4 are potential microtubule-binding domains with higher similarity scores (Figure 3.10). The sequences are listed in Table 3.3. How these peptides are aligned with tau, MAP2, and MAP4 is shown in figures 3.7, 3.8, and 3.9, respectively.

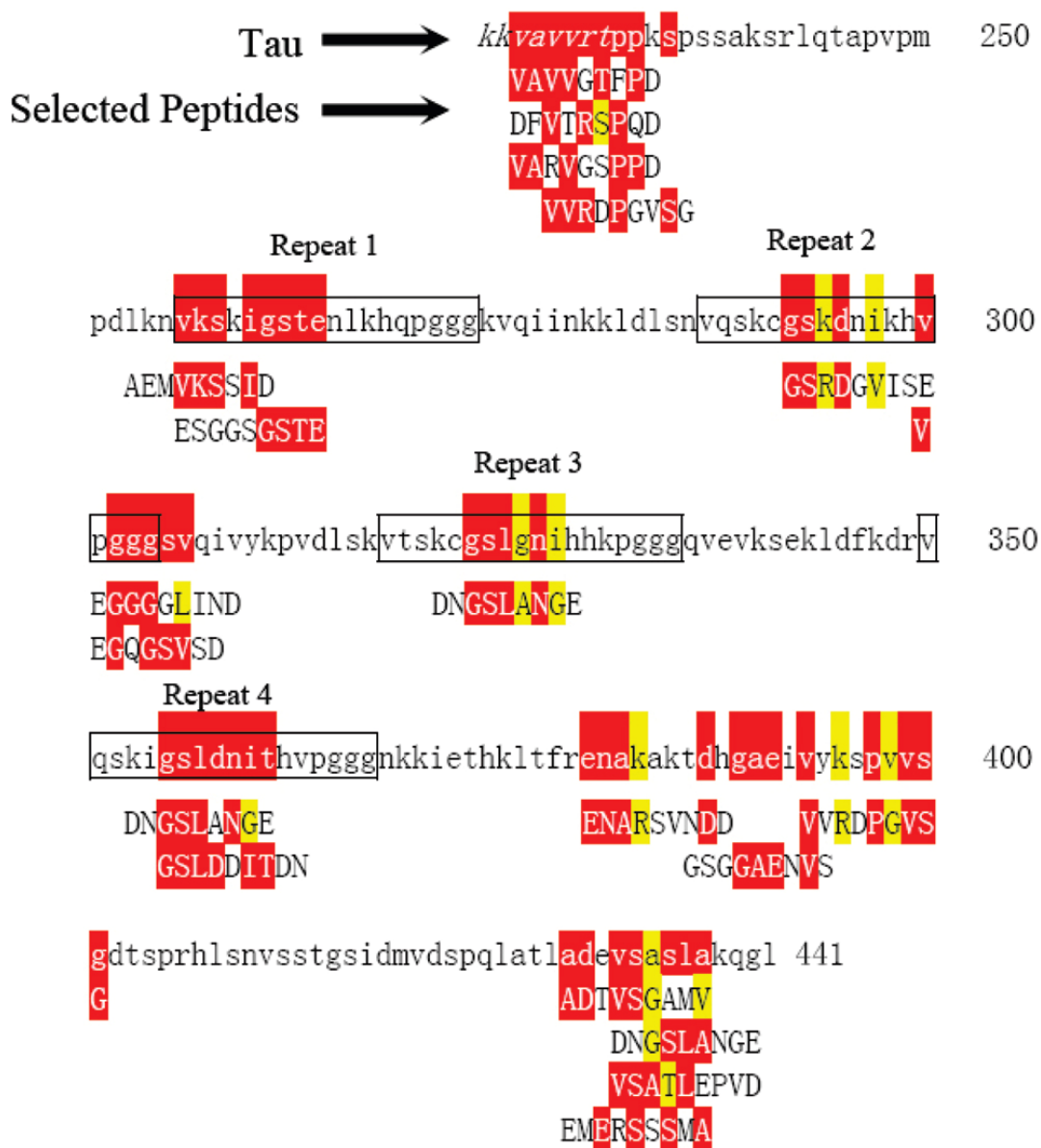


Figure 3.7 Alignment of our selected peptides with tau. First row is the sequence of microtubule binding domains on Tau and peptides below are our affinity-selected peptides. Four repeats are highlighted by boxes. Identical amino acids are highlighted by red and those with similar properties are highlighted by yellow. Reproduced with permission from reference 179.

SYSSRIPGTPGIPSYPRTPGT (1614-1635)
 VSIPGSPDD VSIPGSPDD
 GSPSEYSSQ VSIPGSPDD

IITQSPSRSSVASPRRLSNVSSSGSINL (1812-1839)
 AGSNINLV
 DSGGSGIAS AYESGTGSS
 VLDSVSSPD GESSGADD
 VLDSVSSPD

LAEDVTAALA (1848-1857)
 GDYQSLVEDVSALEPVD
 GGTESMTAS
 DVSGAFMAD
 GDLVQDVIA
 GSGGAENVIS

Figure 3.8 Alignments of selected peptides with MAP2. Reproduced with permission from reference 179.

PASAPAVKPGSKSTQAVPKAPATATLASPGST (738-769)
 EWDPAPAME VSTPGSPDD
 EYSAPSADA VSATLEPVD
 ESGGSGSTE AFNATASMS
 APTVEADNN DGFADLASD
 VYQNSSESTL

ANASAPDLKNVRS (870-883)
 GMNNASFPD
 VLDSVSSPD ENARSVNDD
 ADGSPDLPA
 APNLSISDS

KAAGPIGNAGK (922-932)
 EAGPIPGDG

KVGSLDNVGH (985-994)
 VARVGSPPD
 DNGSLANGE
 GSLDDITDN
 VLDSVSSPD

KTEGGGSEAPP (1002-1014)
 EGGGLIND
 ESGGSGSTE
 GGTESMTAS
 SEVEGG
 DSGGSGIAS
 EYSSSELPP
 GSGGAENVIS
 VEGQGSVSD

ASASGLSGHT (1035-1044)
 GGDFAAANG
 ESGGSGSTE
 DSGGSGIAS

Figure 3.9 Alignments of selected peptides with MAP4. Reproduced with permission from reference 179.

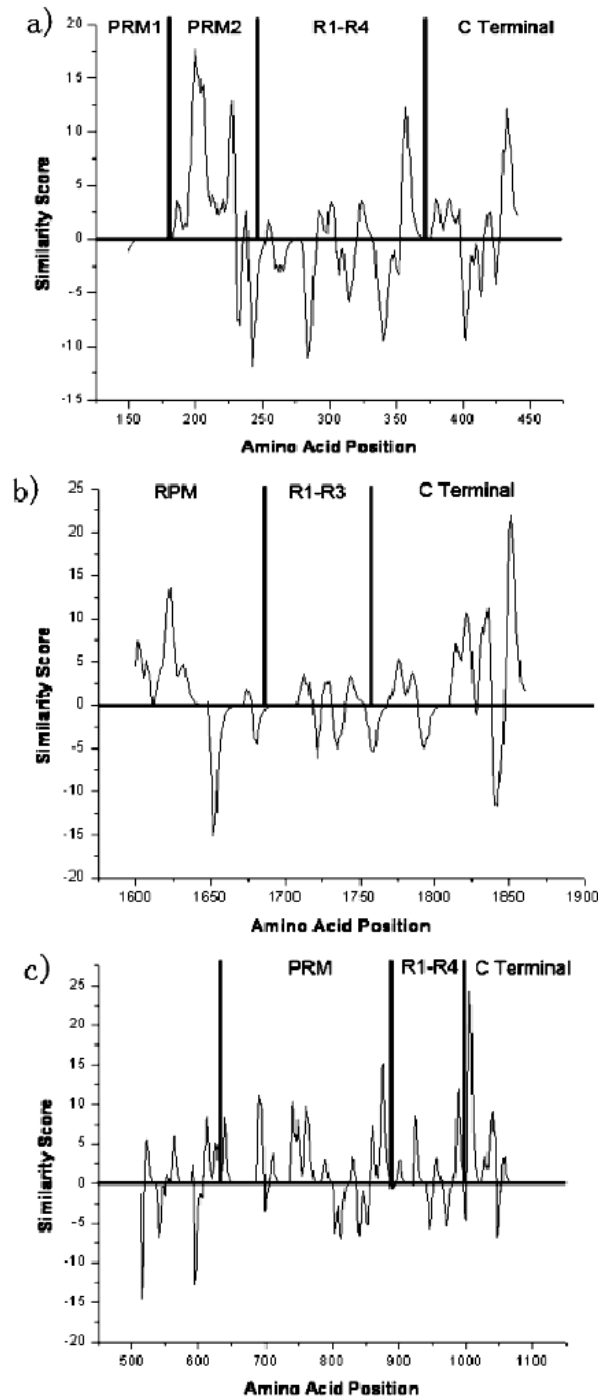


Figure 3.10 Cumulative similarity score of each amino acid in the microtubule-binding regions of the proteins of the MAP2/tau family. (a) Tau, (b) MAP2, and (c) MAP4. The scores are calculated by using

RELIC/MATCH program. PRM: proline rich motif. R1-R4: repeat 1 to repeat 4. Reproduced with permission from reference 179.

Table 3.3 Potential microtubule-binding domains on MAPs from the alignment of selected peptides to MAPs sequence. Reproduced with permission from reference 179.

MAPs	region	previous studies	this work	sequences
MAP1A	HC	281–630	527–537	SPEDLQPFEE
	HC	NI	970–990	ALGEVEERCLSPDDSTVKMAS
	HC	NI	1058–1064	PTRSPQA
	HC	1250–1600	1292–1315	MTSDSSLTKSPESLSSPAMEDLAV
	HC	NI	1877–1900	KAEGEREGEGGAGAPDSSSFSPKV
	HC	NI	2390–2410	PGKSSGGPPCSLSSEVEAGPQ
	LC	N terminal of LC	2653–2671	GSKGGSGPPVYVDLAYIPN
MAP1B	HC	517–848	820–837	LEAERSLMSSPEDLTKDF
	HC	NI	1086–1099	TLPGGSESEATASD
	HC	NI	1285–1296	AEGEARSVSPGV
	HC	NI	1438–1444	SPVSDLT
	HC	NI	1756–1767	SLYASLASEKVG
	HC	NI	1853–1888	EKDSGGKTDGDFNYAYOKPENAAAGSPDEEDYDYESQ
	HC	NI	2020–2039	SYETSTKTRSPDTSAYCYE
	LC	NI	2120–2129	TQSGGAPPPS
	LC	2210–2336	2276–2288	SSDKVSRVASPKK
	MAP1S	HC	NI	682–697
MAP2	LC	N terminal of LC	NI	NI
	PRM	NI	1614–1635	SYSSRTPGTPGTPSPRTPGTP
Tau	PRM/repeats domain	repeats domain and continuous sequences N-terminal to it	NI	NI
	C-terminal	NI	1812–1839	IITQSPSRSSVSSPRRLSNVSSSGSINL
	C-terminal	NI	1848–1857	LAEDVTAALA
	PRM 2	225–231	224–233	KKVAVVRTPP
	PRM 2	240–248	NI	NI
	R1	repeat 1	256–264	VKSKIGSTE
MAP4	C-terminal	370–381	NI	NI
	C-terminal	NI	429–437	ADEVASLA
	PRM	PRM and repeats domain	738–769	PASAPAVKPGSKSTQAVPKAPATATLASPGST
	PRM		870–883	AANASAPDLKNVRS
	R2		922–932	KAAGPIGNAQK
	R4		985–994	KVGLDNLVGH
	C-terminal	NI	1002–1014	KTEGGGSEAPCP
C-terminal	NI	1035–1044	ASASGLSGHT	

3.3.4. Comparison of Our Identified Domains on Tau with Reported Domains from Literature.

We aligned our selected peptides with the sequences of the microtubule-binding regions of tau (Figure 3.7). From Figure 3.7, it represents that both KAVAVVRTPP at PRM2 and ADEVASLA at C terminal tail of tau match four types of affinity-selected peptides out of a total of 87 unique sequences. If the frequency of each peptide is

considered, KVAVVRTPP has a total of 17 matched peptides out of 143 sequenced peptides and ADEVSASLA has 13. ²²⁴KVAVVRTPP₂₃₃ has one VxxVxxxP sequence that is a close variant of the consensus sequences (VxxVGxxPD and VxxxxxPD) found among the three most common peptides identified. From the previous literatures, KKVAVVR has been reported as a microtubule binding domain [159, 160], while ADEVSASLA at the tail has not been reported as a microtubule-binding domain yet. For repeats domain, we can only find matches on four 18-mer repeats but not on inter-repeat (IR) regions (Figure 3.7). This finding is consistent with Butner's data [161], but against Goode's data [162], which supports that R1-R2 IR binds to microtubules with high affinity. Among these four repeats, repeat 1 of tau matched six of the affinity-selected peptides, while repeat 2, 3, and 4 only have 4, 3, and 4 matched peptides, respectively, while the frequency of each peptide is considered. This comparison indicates that repeat 1 has a higher probability of being involved in binding to the tubulin targets than other repeats. But it is still lower than KVAVVRTPP and ADEVSASLA. This fact confirms that repeat 1 has relatively higher binding affinity [161]. It is also consistent with the

previously reported model that flanking domains have strong binding affinity while the interaction between microtubule and repeat domain has specificity but relatively weak binding [159, 160].

To verify that tubulins can be specifically bound to our selected peptides as well as to our identified microtubule-binding domains, we used TEM imaging to test the interaction of tubulins and tubulin-selected phages, which displayed three tubulin-binding peptides (VARVGSPPD, AEMVKSSID, and ADTVSGMV). Each of these three selected peptides has a higher frequency (Table 3.1) and matches a separate domain of tau (Figure 3.7). VARVGSPPD peptide matches $_{225}\text{KVAVVRTPP}_{233}$ on flanking domains; AEMVKSSID peptide matches $_{256}\text{VKSKIGSTE}_{264}$ from repeat 1 and ADTVSGMV peptide matches $_{429}\text{ADEV SASLA}_{437}$ on C terminal tail. At the same time, phages displaying KSRLQTAPV were treated as a control to interact with tubulins. This peptide, also from the flanking domain of tau, is not matched by our selected peptides. From the TEM images, we can see control phage (i.e., nontubulinbinding phage) is separated from each other and most tubulins are not associated with the

phage due to the lack of the binding interaction between phages displaying KSRLQTAPV and tubulins (Figure 3.11). However, our tubulin-selected surfaceengineered phage (VARVGSPPD, AEMVKSSID, and ADTVSGMV) can bind free tubulins. The tubulin-phage binding interaction holds phage together, leading to the formation of bundles and nets (Figures 3.11, 3.12, and 3.13). Namely, the tubulins, which bind to the side wall of the binding phage, serve as a bridge to cross-link the phages. Similar cross-linking between phages by their binding partners was recently reported when cationic gold nanoparticles were present in the suspension of anionic phages and served as “cross-linking agents” [43]. The TEM results directly show that VARVGSPPD, AEMVKSSID, and ADTVSGMV are microtubule-binding peptides and indirectly confirmed that KKVAVVRTPP, VKSKIGSTE, and ADEVSASLA are microtubule-binding regions but KSRLQTAPV is not. Therefore, our work confirms the previous knowledge that KKVAVVRTPP on tau is a microtubule-binding domain [159, 160] and also suggests that VKSKIGSTE and ADEVSASLA on tau are new potential microtubule-binding domains not identified before.

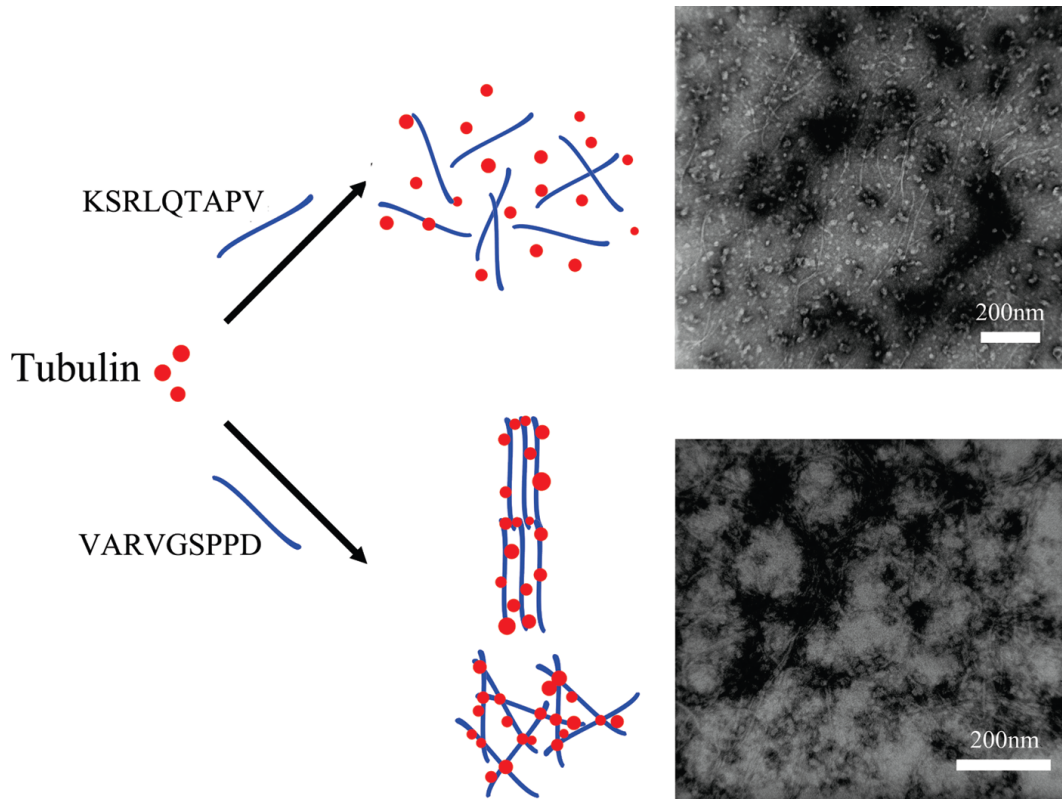


Figure 3.11 Interaction of tubulin-selected phage and free tubulins verified by TEM. Red circles are tubulins and blue lines are phages. Phages displaying KSRLQTAPV do not interact with tubulins, leading to the random distribution of spatially separated phage and tubulins, while our affinity-selected surface-engineered phage (VARVGSPPD) can specifically bind tubulins, resulting in the cross-linking of phages and the formation of bundles and nets. Reproduced with permission from reference 179.

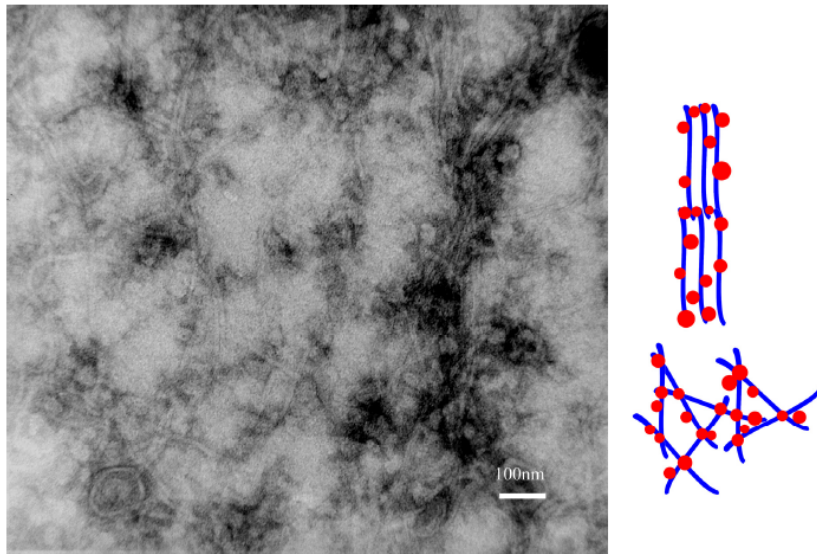


Figure 3.12 Formation of bundles due to the interaction between tubulin-selected phage (displaying tubulin-binding peptide ADTVSGMV) and tubulins. Reproduced with permission from reference 179.

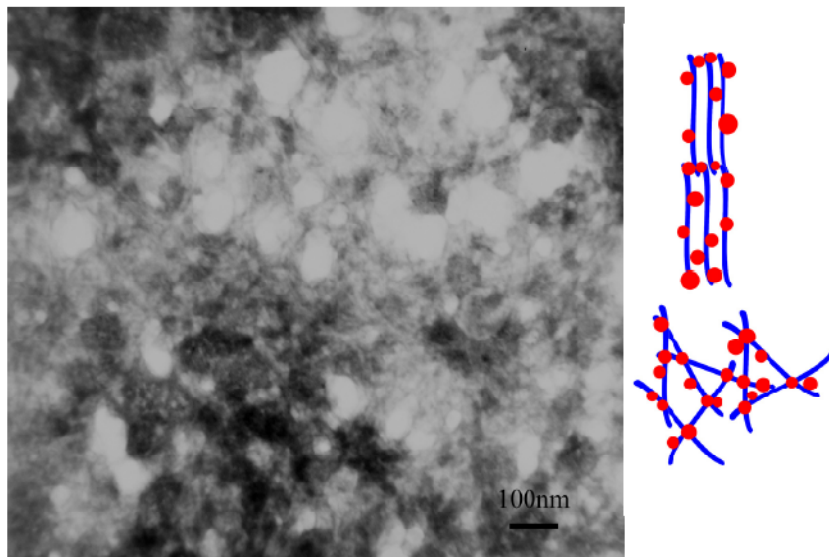


Figure 3.13 Formation of bundles and networks due to the interaction between tubulin-selected phage (displaying tubulin-binding peptide AEMVKSSID) and tubulins. Reproduced with permission from reference 179.

3.3.5. Comparison of Our Identified Domains with other MAPs with Reported Domains from Literature.

1. MAP1B

We identified eight potential microtubule-binding domains of MAP1B (Table 3.3 and Figure 3.3). Among them, two domains (820-837, 2276-2288) are located at two microtubule-binding domains reported in previous reports [146, 163, 164]. One of them, ²²⁷⁶SSDKVSRVASPKK₂₂₈₈, has a pattern (VxxVxxP) that is a close variant of the consensus sequence (VxxVGxxxPD) from the most common peptides identified. The other six domains are potential new microtubule-binding domains. These six domains include three domains 1086-1099, 1285-1296, 1438-1444 on an assembly helping domain (998-1440), which is believed to assist microtubule assembly [165], two domains 1853-1888, 2020-2039 on a hydrophilic region (1866-2071) near the C-terminal containing 12 imperfect repeats (YSYETXEXTTXXPXX), domain 1756-1767 located between assembly helping domain and hydrophilic region on the heavy chain, and domain 2120-2129 at the N-terminal of the light chain.

2. MAP1A

Three microtubule-binding regions have been identified in previous work: 281-630 [144], 1250-1600 [145] on the heavy chain, and N terminal of light chain [140, 142, 143]. We identified seven potential microtubule-binding domains from MAP1A listed in Table 3.3 (Figure 3.3). Three of the seven domains (527-537, 1292-1315, and 2653-2671) are included within those three earlier identified microtubule-binding regions. The other four domains we identified are all on the heavy chain, which we believe are new microtubule-binding candidates.

3. MAP1S

So far, only one microtubule-binding domain has been reported on MAP1S and is located at the light chain [140]. Our work did not find any microtubule-binding domain on light chain by using RELIC/MATCH program. Instead, we found domain 682-697 has a relatively high similarity score and contains two positively charged Arginine residues which make it a potential microtubulebinding domain on MAP1S (Figure 3.3).

4. MAP4

We identified six potential microtubule-binding domains from MAP4 listed in Table 3.3 (Figure 3.10). These domains include two (738-769, 870-883) from the PRM, two (985-994 and 922-932) from the repeat domain, and two (1002-1014 and 1035-1044) from the C terminal tail. It was previously reported that repeated region plus proline rich region are essential for microtubule binding [148, 166, 167], but the detailed binding domains have not been reported yet. Our identified domains are located within the general region reported previously, thus provided more specific microtubule-binding positions.

5. MAP2

We identified three potential microtubule-binding domains from MAP2 listed in Table 3.3 (Figure 3.10). One domain (1614-1635) is from RPM and the other two (1812-1839 and 1848-1857) are from the C terminal tail. This result is different from the former findings that the repeat domain and regions from both the PRM and C terminal domain adjacent to repeats domain are responsible for the interaction between MAP2 and

microtubules [138, 168, 169]. In addition, the Coffey group considered repeat 2 contributes to the binding and promotes the nucleation of microtubules [170, 171]. Apparently, more work will be needed to further study the interaction.

3.3.6. Advantages and Limitations of Using Landscape Phage Display for Identifying Microtubule-Binding Domains.

Many methods have been used to study the interactions between MAPs and microtubules, such as cosedimentation [147], cryo-EM [136], fusion protein with fluorescence, gold nanoparticle labeling [134], NMR [130, 159], and microtubule binding assay [137, 148, 164]. Besides these techniques, cocrystallization and yeast two-hybrid display are also popular tools for protein-protein interaction studies. Our work represents the first attempt to apply the phage display biopanning method to identify microtubule-binding domains on MAPs. The technique mimics antibody-antigen interaction screen and can be regarded as mimicking the strategy of the immune system [172]. Compared with other methods, it has many advantages. First, this technique is very universal. Its targets could be

proteins, small molecule drugs, inorganic crystals, cells, and tissues. Second, interacting proteins of the target are even not needed to study the interactions. For new proteins, it is always a good way to predict their interacting proteins while other methods mentioned above can only passively confirm proposed interacting proteins. Third, the selected peptides can provide insight into the minimum composition requirements for binding to the targets. The size of phage-display-selected binding domains is much smaller than the results from traditional biological methods. Fourth, phage display biopanning is not time-consuming and is cost-effective. The biopanning just needs several weeks of experiments and is supported by bioinformatics software such as RELIC. The selected peptides against one target can be used in the study of all target-interacting proteins.

In this work, we can align our selected peptides with six kinds of MAPs simultaneously by using RELIC and further identified novel potential microtubulebinding domains on MAPs. For example, Tau is one of the most important MAPs. Some of our affinity-selected peptides confirm the

previously reported microtubule-binding domains on tau, such as KVAVVRTPP from PRM2, indicating that our biopanning technique is suitable for identifying potential novel microtubule-binding domains. Moreover, because the peptide sequences identified by phage display are generally shorter than the binding domains reported previously, the identified binding domains are more specific segments on the MAPs. This fact can be considered as an important advantage of using phage display technique to identify microtubule-binding domains. On the other hand, some domains have not been reported yet, such as ADEVSASLA on the C terminal tail of tau. One of the reasons is that our targets are purified tubulins instead of preassembled microtubules so that the inner surface of microtubules and tubulin-tubulin interaction interfaces could be exposed to the phage library. As a result, more potential binding domains are identified from our method. Although the large periodic array of peptides presented on the side wall of the fd-tet phage may mimic the repeating units in tau during the biopanning process, those peptides can't fold up to form loops to bind taxol pocket efficiently. This is perhaps the limitation of phage display described in this work. It thus explains why the similarity

score of repeat 1-3 of tau is relatively low. However, the phage displaying affinity-selected tubulin-binding peptides, which match these repeat domains of tau, did bind to tubulins according to our TEM study.

3.4. Conclusion

In summary, biopanning of a phage displayed random peptide library (a pVIII library) against the purified tubulins was performed to study the interactions between MAPs and microtubules. RELIC was applied to align the affinity-selected peptides identified in biopanning with the sequences of different MAPs and thus identify the microtubule-binding domains of these MAPs. Based on our data, some known microtubule-binding domains are confirmed and many new domains (Table 3.3) on the MAPs are identified, which can play important roles in the binding interaction between MAPs and microtubules.

Chapter 4 A Selection of Hydroxyapatite-Binding phage for the Fabrication of Bone Regeneration Scaffold

4.1. Introduction

For a long time, conventional large sized HAP ceramics have been synthesized and incorporated into designed biomaterial composites. But hydroxyapatite presence in natural bone is in the form of nano-sized needle-like crystals nucleated and grown on collagen fibrils. With the development of nanoscience, nanophase HAP structures have been synthesized and characterized, showing more attracting properties. Therefore, in our work, we employed needle-like HAP nanorods as the main component of the scaffold.

Bone is a hierarchically structured composite material. The lowest level of organization is composed of nanophase HAP crystals along collagen fibrils with their c-axis preferentially parallel to the collagen fibrils. In order to mimic the structure of nature bone, an organic component that substitutes collagen fibrils is needed. Here, fd bacteriophage (also called phage) was preferred as this organic bone substitution material. Fd phage

is a flexible bio-polymer-fiber with 7 nm in width and 1 μm in length, mimicking the morphology of collagen fibrils. For its structure, it has a single stranded DNA packed into an outer protein coat composed of 3900 copies of major coat proteins (pVIII) and 5 copies of minor coat proteins (including pIII, pVI, pVII, and pIX) at tips (Figure 4.1j). The protein coat can be genetically engineered to display foreign peptides [173] which is known as phage display. Based on this technique, several foreign peptides can be displayed on the outer surface of one single phage simultaneously, making it possible for an individual nanofiber to present both HAP-binding peptide and other functional peptide (double display) [46, 47, 174]. Such engineered phages can not only assemble with HAP nanorods to form a hybrid scaffold but also induce functional peptides into the scaffold for multi-purpose applications. Therefore, morphological similarity and powerful phage display technique are two main reasons of choosing bacteriophages over other organic polymers in this work.

Herein, we report a selection of HAP-binding peptides/phages using landscape phage library and assembly of selected HAP-binding

phages with HAP nanorods into a scaffold for promoting MSCs seeding and proliferation. Specifically, first, HAP-binding phages were identified and selected from a landscape phage library through a biopanning process (Figure 4.1abcd). Landscape phage library is a collection of phages in which billions of phage clones are present but each clone has one unique peptide displayed on the side wall (i.e., fused to each of the ~3900 copies of pVIII) [175]. And biopanning is a screening process for identifying inorganic substrate targeting peptides/phages [12, 27, 176-179] from a pre-built phage library. Its principle has been described elsewhere [53, 151, 175, 179-182]. Second, identified HAP-binding phages assembled with pre-synthesized HAP nanorods to form a HAP-phage scaffold in which HAP nanorods were parallel aligned by HAP-binding phages (Figure 4.1gh). Third, the viability, adhesion and proliferation of MSCs were tested on HAP-phage scaffold (Figure 4.1hi). MSCs are multipotent stem cells that can differentiate into osteoblasts, chondrocytes and adipocytes. Because of their broader differentiation ability, a significant number of studies have been focused on MSCs for their potential applications in the repair of bone, fat tissue, cartilage, and more

significantly, bone regeneration [183-185]. Therefore, to test if MSCs can proliferate on the HAP-phage scaffold is a critical step towards real applications.

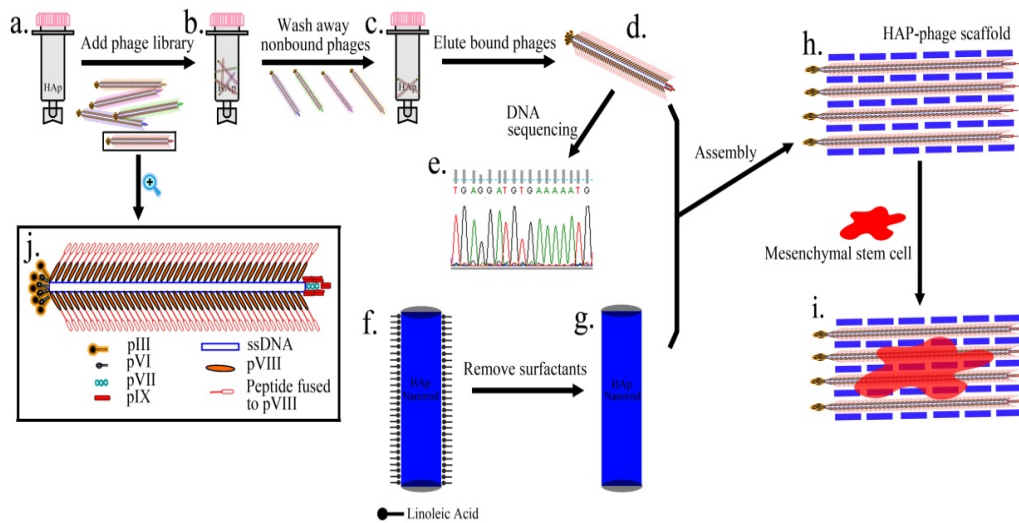


Figure 4.1 Schematic diagram of developing HAP-phage scaffold for the proliferation of mesenchymal stem cells.

4.2. Experiments

4.2.1. HAP Nanorods Synthesis

HAP nanorods were synthesized by the hydrothermal method reported by Li's group with slight modifications [186]. In brief, 0.5 g octadecylamine, 4 mL linoleic acid and 16 mL ethanol were mixed under agitation. 7.5 mL $\text{Ca}(\text{NO}_3)_2$ solution (0.5 g in 7.5 mL water) was then

added for ion-exchange process followed by adding 7.5 mL Na_3PO_4 solution (0.5 g in 7.5 mL water) for reaction. The system was sealed and hydrothermally treated at 90 °C in an oven for more than 10 hours.

4.2.2. Surfactant Removal from HAP Nanorods

50 mL ethanol was added to the mixture after reaction and then the solution was centrifuged at 10,000 g for 10 minutes. The supernatant was discarded and 400 mL NaOH-ethanol solution (95% ethanol and 5% 10 M NaOH in water) was added to suspend HAP nanorods pellet. The suspended solution was agitated at 90 °C for 24 hours to remove surfactants which were on the surface of nanorods. Then the mixture was centrifuged again at 10,000 g for 10 minutes and the pellet was re-suspended by 40 mL water. Thus surfactant-free HAP nanorods were prepared and suspended in water for using. The removing of surfactant molecules were confirmed by Raman study. Basically, several drops of surfactant-free HAP nanorods in water and surfactant-coated HAP nanorods in hexanes were dropped on a glass slide. After the samples

were dried, they were analyzed on a confocal raman microscopy. The detailed analysis can be found in results part.

4.2.3. Solutions and Typical Methods.

Phosphate buffered saline (PBS) pH 7.0 with different phosphate concentrations like 725 mM or 1000 mM . A solution made of 0.1 N HCl with glycine and bovine serum albumin (BSA) with pH 2.2 was regarded as elution buffer. Tris buffer saline (TBS) and tetracycline stock were prepared using the methods reported in the references [187, 188].

4.2.4. Hydroxyapatite Column Preparation

We prepared the HAP columns using QIAquick spin columns, which have a filter disc and an open bottom, from Pierce (product # 89868). About 5 g of HAP nanorods were placed into a beaker and washed 3-4 times by 20 mL of 10 mM phosphate buffer saline (PBS) each time. Empty QIAquick columns were weighed and then filled with ~100 μ l of the HAP suspension in 10mM PBS. The columns were centrifuged at 10,000 g for one minute to form a layer of HAP on the column filter and remove the PBS from the open bottom. The column was reweighed to get

the weight of HAP nanorods settled on the column filter. The column was washed several times using 200 μ l of PBS and centrifuged in order to make sure that the HAP loaded in the column was well settled on the filter disc.

4.2.5. Biopanning: Selection of HAP-Binding Phages

We adopted a biopanning approach by modifying to the protocol [189] and performed a selection under stringent conditions. Here, we constructed and used two types of landscape phage libraries f8/8 (2×10^{11} cfu/mL) and f8/9 (1.4×10^{11} cfu/mL) landscape phage libraries respectively. Eight and nine amino acids were displayed randomly on the major coat protein pVIII of vector f8-1 (fd-tet derivative) in f8/8 and f8/9 library, respectively. The phage libraries (f8/8 and f8/9) were first diluted to 10^9 virions/mL by diluting 25 μ l of phage library in 275 μ l of 725 mM PBS (the total volume is 300 μ l). Under such stringent conditions (\sim 725 mM), non-specific and weakly-bound phages will not bind to HAP but high affinity phages which have specific interaction with HAP can only bind to HAP nanorods. Before the process of selection, we performed depletion step by

adding the above mentioned 300 μ l phage solution to an empty column and the column was incubated at room temperature with rotation, during which the phage specific for plastic walls, rubber O-ring and filter will be attached and the rest of the unbound phages will be still in the solution. These unbound phages (depleted phage) were eluted by centrifuging the column at 10,000 g for one minute and collected. The depleted phage suspension was then added to the HAP nanorods inside the column and allowed to equilibrate with the HAP nanorods by rotating the loaded columns for 1 hour at room temperature. Then the HAP column was washed extensively for about 20 times with washing buffer (1000 mM PBS), and followed by elution buffer pH 2.0, in order to release the HAP-binding phages off HAP nanorods. The eluates were collected into tubes, neutralized with 19 μ l of a neutralizing buffer (1 mol/L Tris-HCl, pH 9.1) and stored at 4°C until titering. The selected HAP-binding phages were amplified and propagated. Finally, the specific part of the phage genome was subjected to PCR amplification and sequenced to obtain the sequences of the HAP-binding peptides.

4.2.6. Receptor Ligand Contacts (RELIC)

Selected peptides were analyzed by a bioinformatics tool known as receptor ligand contacts (RELIC) [153]. It has a suite of programs for combinatorial peptide analysis by evaluating the statistical properties of a collection of affinity-selected peptides [153, 179]. RELIC/MOTIF what we used is designed for searching for conservative motifs within the peptide population. The basic principles and applications were summarized in previous report [153, 179].

4.2.7. Specificity Determination of Selected Phages through Binding

Assay

We performed binding assay in order to determine the specificity of the selected phages and to determine which sequence among the selected ones is the best binder for HAP. Binding assay is similar to the biopanning procedure mentioned in the previous section. Briefly, the HAP columns were prepared as mentioned and loaded with the selected phage diluted in high concentrations of PBS (725 mM PBS). Under such stringent conditions, non-specific and weakly-bound phages will not bind to HAP but

strongly bound phages which have specific interaction with HA can only bind to the HAP powder. Then the column was washed first with 750 mM PBS for 20 times and then with 1000 mM PBS, followed by an elution buffer. The acid eluate was neutralized with 19 μ l of 1 mol/L Tris-HCl, pH9.1. All the eluates were tittered.

4.2.8. Interaction between HAP-Selected Phage and HAP

Powder/HAP Nanorods and Characterized by Transmission

Electron Microscopy (TEM)

A total of 20 μ L of selected phage (anti-tetracycline) infected *E. coli* K91 BlueKan cells (anti-kanamycin) was transferred into a tube with 4 mL of NZY/tetracycline (20 μ g/mL), followed by shaking overnight at 37 $^{\circ}$ C. Contaminated bacteria cells were killed because they are lack of an anti-tetracycline gene. Culture (4 mL) was transferred into 1 L of NZY/tetracycline (20 μ g/mL) in a 2.5 L flask, incubated for 12 h at 37 $^{\circ}$ C with shaking, and purified by double PEG precipitation. Purified phage solution (100 μ L; 1.4×10^{11} virions/mL) was mixed with 1 mL of HAP

powder/HAP nanorods solution (5 mg HAP powder/HAP nanorods in 1 mL water), and the mixture was incubated at room temperature for 24 hours.

4.2.9. Assembly of Selected Phage and HAP Nanorods into a

Scaffold

Fd phage displaying the HAP-binding peptide was amplified and purified by PEG purification. The final concentration of phage solution was about 4.5×10^{12} virions/mL. 20 mg HAP nanorods in 100 μ L were sonicated for 30 minutes, mixed with 500 μ L selected fd phage, and then frozen in liquid nitrogen immediately. The water in frozen mixture was sublimated in a freeze-dryer for 12 hours at -40 $^{\circ}$ C, forming the phage – HAP scaffold. The scaffold was characterized by scanning electron microscope (SEM) and the solubility in water was also tested. 20 mg HAP nanorods in 600 μ L water, 600 μ L of phage solution, and 600 μ L of wild type fd phage were processed as controls.

4.2.10. Sample Preparation for TEM and SEM Characterization

A total of 10 μ L of the mixed HAP nanorods and HAP-binding phages was placed on the formvar and carbon coated copper grid for 5

minutes, rinsed by 3 drops of distilled water, stained with 0.5% phosphotungstic acid (PTA) once, and observed under TEM (Zeiss 10). Fabricated HAP-phage scaffold was immobilized on a SEM holder with silver paste, sputter-coated with very thin gold and then characterized under SEM.

4.2.11. Harvest and Isolation of Rat MSCs

Bone marrow was obtained from femur of fisher 334. MSCs were isolated by a modification of methods previously described [190, 191]. Briefly, one volume of a bone marrow sample was mixed with two volumes of phosphate-buffered saline (PBS), and the mixture was centrifuged at 1000g for 4 minutes. The supernatant was discarded and the pellet was washed two more times with Dulbecco's Modified Eagle Medium (DMEM; GIBCO BRL, Grand Island, NY, USA). After determination of the cell viability and number using trypan blue staining following lysis of erythrocytes by the addition of 4% acetic acid, 5×10^4 /cm² nucleated cells were plated in T-25 culture flasks in DMEM (low glucose) containing: penicillin G 100 U/mL, streptomycin 100 µg/mL, amphotericin B 0.25

$\mu\text{g/mL}$, HEPES 2.4 mg/mL, NaHCO_3 3.7 mg/mL, and 10% fetal bovine serum (Invitrogen, USA) also termed standard growth medium.). The cells were incubated at 37 °C in a humidified atmosphere containing 5% CO_2 . After 3 days of culturing, the nonadherent cells were removed by changing the culture media. The adherent cells were grown to 90% confluency to obtain samples, here, defined as passage zero (P_0) cells. MSCs at P_0 were washed with PBS and detached by incubation with 0.25% trypsin-EDTA for 2 to 3 min at 37 °C. The complete medium was added to inactivate the trypsin. The cells were centrifuged at 1000g for 3 min. The medium was then removed and the cells resuspended in 2 to 5 ml of complete medium. The cells were counted using a hemacytometer and plated as P_1 in 25- cm^2 flasks at a density of 5×10^3 cells/ cm^2 . The medium was changed every 2 to 3 days and the cells were passaged every 3 to 4 days. All the cells used for the experiments were P_3 .

4.2.12. Assessment of MSCs Proliferation/Cell Viability

MSCs were plated at a density of 4×10^3 cells/well in 96-well plates in a standard growth medium for 72h. Measurement of cell viability was

done by a 3-(4,5-dimethyl thiazol-2-yl)-2,5-diphenyl tetrazolium bromide (MTT) assay. MTT was used as an indicator of cell viability as determined by its mitochondrial-dependent reduction to formazone. MTT (5 mg/ml, 20 μ l /well, Sigma, USA) was then added to the cell cultures for an additional 4 h period. The supernatant was then discarded, followed by the addition of dimethyl sulfoxide (DMSO, 150 μ l/well, Sigma, USA) and agitated for 10 min to dissolve the crystal completely. The values of OD were measured at a 490 nm wavelength on a plate reader (Biotek, USA).

4.2.13. SEM Characterization for MSCs

MSCs were seeded (5×10^3 cells) on petriplates containing coverglass. The morphology of the cells in the presence of scaffolds was assessed using scanning electron microscopy. For this, after 2 days of seeding the MSCs onto the cell-scaffold complex was washed with PBS to remove non-adherent cells and then fixed in 2.5% glutaraldehyde for 1 h at room temperature and subsequently washed twice with sodium cacodylate buffer (0.1 M, pH 7.4). The cells were fixed in osmium tetroxide solution for one hour, followed by dehydration through a series

of graded alcohol solutions and critical point drying. The dried cellular constructs were sputter coated with gold and observed under SEM (JEOL JSM-880 high resolution scanning electron microscope) at an accelerating voltage of 15 kV.

4.3. Results

4.3.1. HAP Nanorod Synthesis and Surface Modification

Hydroxyapatite presence in natural bone is in the form of nano-sized needle like crystals nucleated on collagen fibrils with their c-axis parallel to collagen fibrils. In order to mimic this form of HAP in natural bone, crystalline HAP nanorods were synthesized via the hydrothermal method reported before [186]. The synthesized HAP nanorods had a quite uniform size with a width of 10 nm and a length of 150 nm (Figure 4.2a). In addition, these HAP nanorods were in crystalline form which could be verified by electron diffraction pattern (Figure 4.2a). The inner circle of the electron diffraction pattern was corresponding to the (002) plane of HAP crystal and the outer circle was corresponding to (211) plane.

HAP nanorods synthesized from the hydrothermal method could only disperse in non-polar solvents rather than aqueous solutions. It is because that these HAP nanorods were all surrounded by a layer of surfactant (linoleic acid) [186]. The surface of HAP nanorods coated by surfactants could not mimic the surface chemistry and biological functions of HAP crystals in natural bone. In order to expose real surfaces of HAP nanorods, the surfactant layer was removed through the treatment of NaOH-ethanol solution at 90 °C for 24 hours, resulting in surfactant-free HAP nanorods. These surfactant-free HAP nanorods could be dispersed uniformly in aqueous solution for several days. In addition, the removing of surfactants was also verified by comparing raman spectra of surfactant-free HAP nanorods and surfactant-coated HAP nanorods (Figure 4.2b). The spectrum of surfactant-free HAP nanorods (black line) showed only typical peaks (V1, V2, V3, and V4 phases of PO_4^{3-}) from HAP crystals [192], while that of surfactant-coated HAP nanorods (red line) showed both typical peaks from HAP [192] and surfactant molecules (linoleic acid). Therefore, we believe that all the surfactants were removed from HAP

nanorods after the treatment of NaOH-ethanol solution, resulting in surfactant-free HAP nanorods for further use.

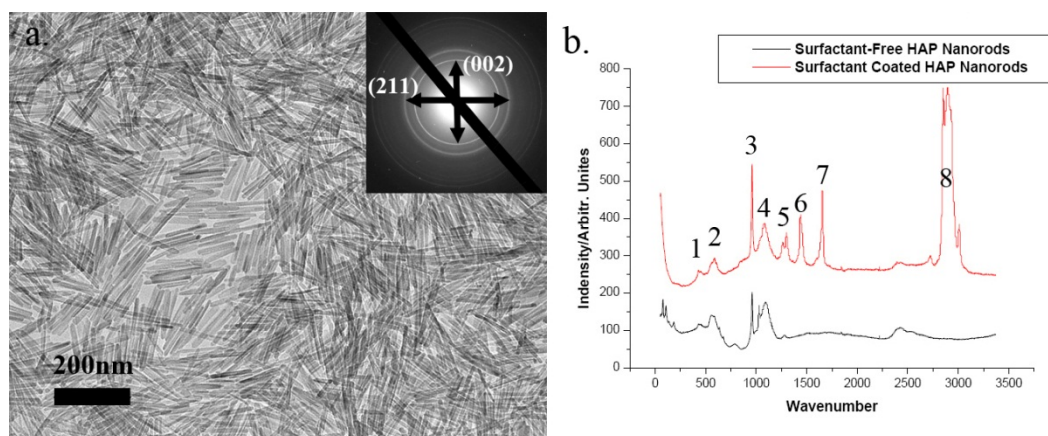


Figure 4.2 Characterizations and surface functionalization of synthesized HAP nanorods. (a) TEM and electron diffraction pattern of synthesized HAP nanorods. (b) raman spectra of surfactant-free HAP nanorods (black) and surfactant-coated HAP nanorods (red). Peak 1: V_2 (E) from PO_4^{3-} ; peak 2: V_4 (T_2) from PO_4^{3-} ; peak 3: V_1 (A_1) from PO_4^{3-} ; peak 4: V_3 (T_2) from PO_4^{3-} ; peak 5: in-plane C-H deformation from C-C groups and in-phase CH_2 twisting motion; peak 6: C-H deformation vibration; peak 7: C-C stretching vibration; peak 8: C=C-H stretching vibration.

4.3.2. Affinity-Selected Peptides

To determine the HAP-binding phage, two phage libraries were allowed to interact with the surfactant-free HAP nanorods. Non-bound and weakly bound phages were washed away using high concentration of PBS buffer. Strongly bound phages were then eluted out with elution buffer (pH=2.2). These eluted phages were allowed to infect starved *E. coli* K91

BlueKan cells and about one hundred colonies were randomly picked out for DNA sequencing (57 from 8-mer library and 54 from 9-mer library). All the selected-peptide sequences are listed in Table 4.1.

Table 4.1 Selected Peptides from Biopanning.

Peptides Selected From f8/8		Peptides Selected From f8/9	
AAASPHAS	EPPHPNPS	AAEIGPSDG	EVSETTVAP
AANASSPT	ERNDMTHV	AASESTASD	GADTADVPL
AGVSNHSQ	ESKPYEIM	AASPSDLES	GDPVAPVDS
ASSSGQEL	ESSATQHV	ADNPVAGAD	GGDDTLAA
ATSPLSRE	ESSPLERQ	ADNPVAGAD	GGPDQEMAS
DAAHEGNP	ESSSQTTP	AGSSGEGMD	GGTGDAMNM
DASRSPST	ESSSTASS	AGTDSDFVD	GILDTAEEES
DDRPSQVS	ETTSHSSP	APGGMSEAT	GPAQDQLES
DDTSRIAQ	ETTSHSSP	ASEMTNLNE	GQTAGDEPN
DETSSTA	EVTNGMG	ASNTDVGDG	GQTAGDEPN
DGSGRIPS	GADSHPGG	DESRRYGDT	GSATSESDN
DHEPDLLP	GDAPPPSM	DGAKDILED	GSDQTVSSE
DPPPALPT	GEMVDASS	DGDHGEKAD	GSELDVSSA
DQPRNALS	GEPAAIPS	DHAYPNDDT	GSNEQYANA
DRPAEAWS	GGPSEYVS	DHQNEAAAS	GSPETVSDM
DSASNTLS	GGSQPGAE	DNRPGDEFD	GSSADEMDT
DSEPSAVM	GPSPEPLP	DPHNGLDTS	GTGGEQAD
DSPDAAMP	GQNGELSV	DRDLAGSNE	GTNTSSADD
DSSNNSMP	GSETSMKL	DRTGENSSE	GTSEVADES
DSSTPSST	GSSEALTM	DSGMRTTDS	GVSGDLGAE
DTPSKSAS	GSSEALTM	DSGTGTSGD	VAGPGDSIE
DTSSTTAP	GSTDIASR	DSRAGDPTL	VEEMSGMAA
EAMTTPST	GTDPAIPE	DYKDQVDPE	VEPGGVAWD
EDTPPEGA	GTSTDVST	EDRGAETGS	VGLQSAGMS
EFSQSRIP	GVTEPPPP	EQMGVNGLD	VGQLDTGTS
EHPSQLSM	VDSTAEGS	ERGLEQSTG	VSGDSMDAS
ENFANTAP	VGPPEKPT	ESDRINDGT	VSSGSAED
ENPKPVPP	VTETYTAA		
EPALTQPT			

4.3.3. Best HAP-Binder Selections

There were 57 HAP-binding peptides from 8-mer library and 54 binding peptides from 9-mer library selected from the biopanning process. In order to pick out the best HAP-binder from these peptides, the following experiments were performed to achieve for this selection: RELIC/MOTIF program, phage binding assay, and direct interaction with HAP crystals.

The first round of selection was performed by RELIC/MOTIF program which searches for conservative motifs within the peptide population [153]. Most functional motifs within various proteins are highly conservative and these motifs can be identified by BLAST, FASTA or other bioinformatic tools [193, 194]. In a similar way, conservative motifs can also be identified by RELIC/MOTIF program within selected peptides, and these motifs may be the target-binding motifs. We performed RELIC/MOTIF against the selected peptides (Table 4.1) and found 13 groups of peptides (20 peptides) sharing conservative motifs (Figure 4.3). These 20 peptides selected by the RELIC/MOTIF program were composed of 10 8-mer peptides and 10 9-mer peptides.

DDRPSQVS EHPSQLSM	VDSTAEGS AGSSGEGMD
DERTSSTA DTSSTTAP ESSSTASS	AASESTASD AGTDSDFVD
DSSTPSST EAMTTPST	AGSSGEGMD DSGTGTSGD GSSADEMDT
DTSSTTAP ESSSTASS	AGSSGEGMD GGTGDAMNM
ESSATQHV AASESTASD	EDRGAETGS GADTADVPL
GSETSMKL AASESTASD	GSSADEMDT GTNTSSADD
GSETSMKL EVSETTVAP	

Figure 4.3 Shared motifs among selected peptides from biopanning landscape phage libraries against HAP powder. Amino acids sharing consensus motifs are highlighted (red letters: exactly the same; green letters: conservative substitutions).

The selected 20 peptides were further tested in binding assay for their relative HAP-binding specificities. In this assay, same amount of each phage with selected peptide were respectively allowed to interact with HAP nanorods at a harsh condition (0.725 M PBS). After several rounds of washing, bound phages were eluted, titered and counted

(Figure 4.4). The number of surviving phages could determine its relative HAP-binding specificity. In the study, three 8-mer peptides (ESSATQHV, ESSSTASS and DSSTPSST) and three 9-mer peptides (GTNTSSADD, AAESTASD and GGTGDAMNM) showed higher HAP-binding specificities (>700) at stringent conditions, while other peptides had relatively lower specificities (<300). These 6 peptides were picked out from the binding assay for the next round of selection.

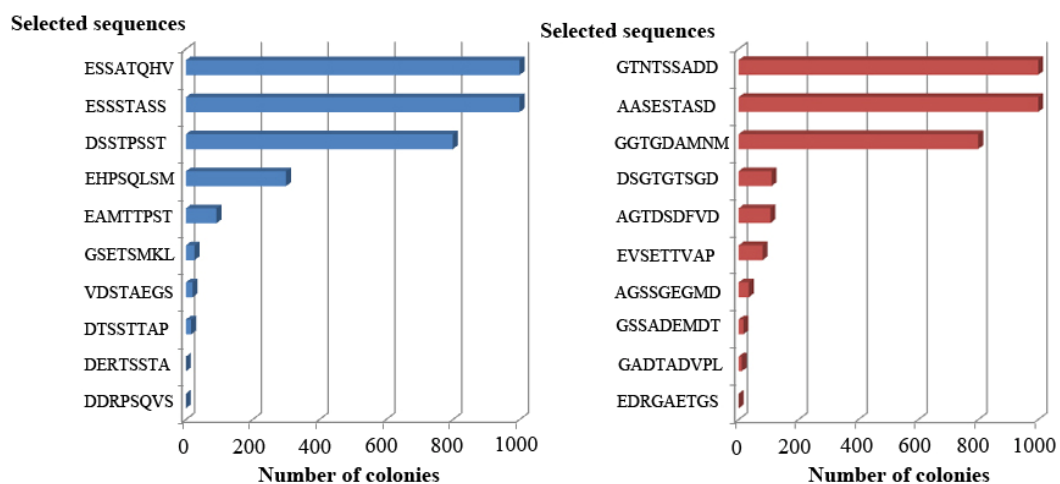


Figure 4.4 The number of colonies in acid eluted solutions in the phage-binding assay. Left chart contains selected peptides from f8/8 library and right chart contains selected peptides from f8/9 library.

From the phage binding assay, we identified 6 better HAP-binding phages (peptides). In order to select the best binder, interactions between

the HAP-selected phages and HAP crystals (Figure 4.5a) were performed and characterized under TEM. We found the phage displaying DSSTPSST was the best HAP-binder. This phage could strongly bind with HAP crystals (Figure 4.5b) and even align nano-sized crystals (Figure 4.5b). Although other 5 phages could also bind with HAP crystals, the binding affinity was not as high as DSSTPSST phage. For example, AASESTASD phage showed relatively low binding affinity with HAP crystals (Figure 4.5c). Wild type fd phage was tested as a control and it showed no interaction with HAP crystals (Figure 4.5d). This series of interaction tests indicated that 6 selected phages could bind with HAP crystals and DSSTPSST-phage is the best binder.

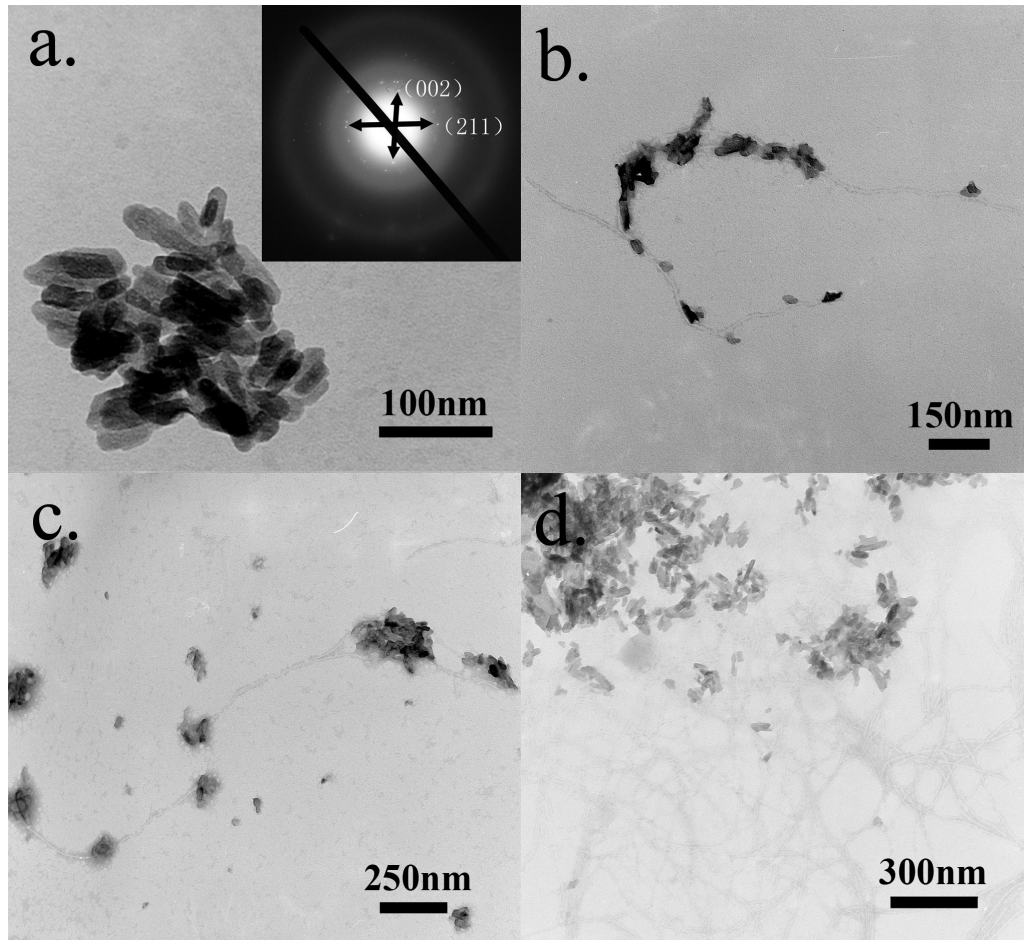


Figure 4.5 Interactions between HAP-Selected Phages and HAP Powder. (a) TEM image and electron diffraction pattern of nano-sized HAP powder. (b) Interaction between DSSTPSST-phage and HAP powder. (c) ESSSTASS-phage has relatively low binding affinity with HAP powder. (d) Wild type fd phage as control shows no interaction with HAP powder.

4.3.4. Interaction between DSSTPSST-Phage and HAP Nanorods

Testing the interaction between the DSSTPSST-phage identified as the best HAP binder and HAP nanorod is necessary. We found that when mixed together, DSSTPSST-phage and HAP nanorod interacted with each

other and HAP nanorods could even be aligned on single DSSTPSST-phage along its long axis direction (Figure 4.6b). Moreover, increasing the amount of HAP nanorods and phage in the solution resulted in a phage-nanorod bundle structure (Figure 4.6c). Wild type fd phage was tested as a control and showed no interaction with HAP nanorods (Figure 4.6d). These facts suggested that DSSTPSST-phage/peptide could interact with synthesized HAP nanorods and assemble them into linear arrays. In addition, these results also further confirmed the successful selection of HAP-binding phage from initial phage libraries.

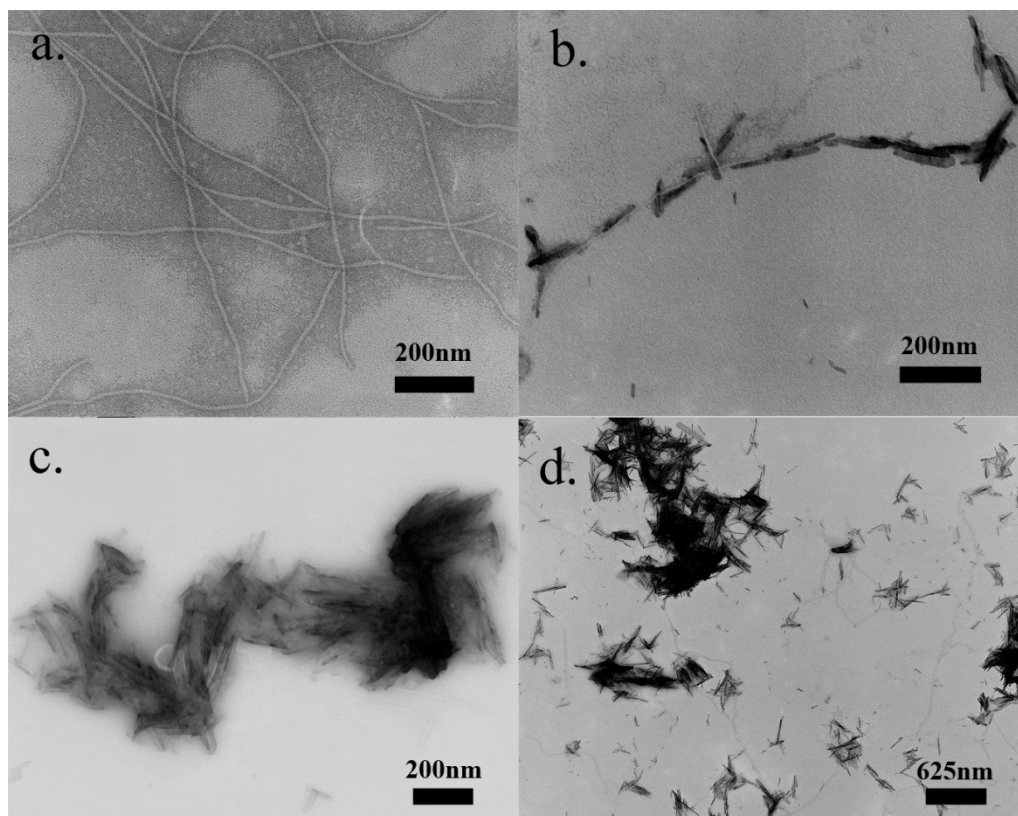


Figure 4.6 Interactions between DSSTPSST-Phages and HAP nanorods. (a) TEM image of DSSTPSST-phage. (b) HAP nanorods were aligned by single DSSTPSST phage. (c) DSSTPSST phages helped HAP nanorods to form a bundle. (d) Wild type fd phages showed no interaction with HAP nanorods. (Original images of b can be found in supporting information as figure S4).

4.3.5. DSSTPSST-Phage - HAP Nanorod Scaffold Fabrication

The fabrication of DSSTPSST-phage-HAP nanorod scaffold was achieved by a freeze-drying method. Briefly, well dispersed HAP nanorods in water were mixed with DSSTPSST-phages and then frozen in liquid nitrogen. Water from the frozen mixture was sublimated in a freeze-dryer

for 12 hours at -40 °C, yielding a phage–HAP scaffold (Figure 4.7a). At the same time, HAP nanorods without any phage, DSSTPSST-phages without HAP nanorods and wild type fd phages mixed with HAP nanorods were separately treated with the same method as 3 controls (Figure 4.7b is from HAP nanorods only; Figure 4.7c is from DSSTPSST-phages only; Figure 4.7d is from wild type fd phages mixed with HAP nanorods). The scaffold obtained from a mixture of DSSTPSST-phages and HAP nanorods had no crystal luster, no shrinking and was relatively hard (Figure 4.7a). SEM images show that the porous scaffold was composed of sheets and fibers (Figure 4.8a) and those sheets and fibers were composed of nanorods and phages (Figure 4.8bc). When adding water, this scaffold was not dissolved or dispersed in aqueous solution but maintaining its scaffold structure like hydrogels. The scaffold formed from HAP nanorods had a typical crystal luster and a slice-like morphology (Figure 4.7b). It was so fragile that any touch would make it collapse. From SEM images, slices composed of HAP nanorods were observed (Figure 4.8de). When adding water, this scaffold was dispersed immediately, leaving a solution just like the one before freezing. The scaffold formed from only DSSTPSST

phages was white and soft. When losing water, it could not maintain its original morphology and shrink (Figure 4.7c). SEM images show that this scaffold was composed of large fibers composed of phage bundles (Figure 4.8f). When adding water, the scaffold was dissolved immediately, leaving a clear solution. The product formed from the mixture of wild type phages and HAP nanorods had no integral structural but only powder (Figure 4.7d). Adding water, the powder could be dispersed immediately. These results unambiguously show that only the mixture of DSSTPSST-phage and HAP nanorod could form a complex scaffold suitable for further cell culturing.

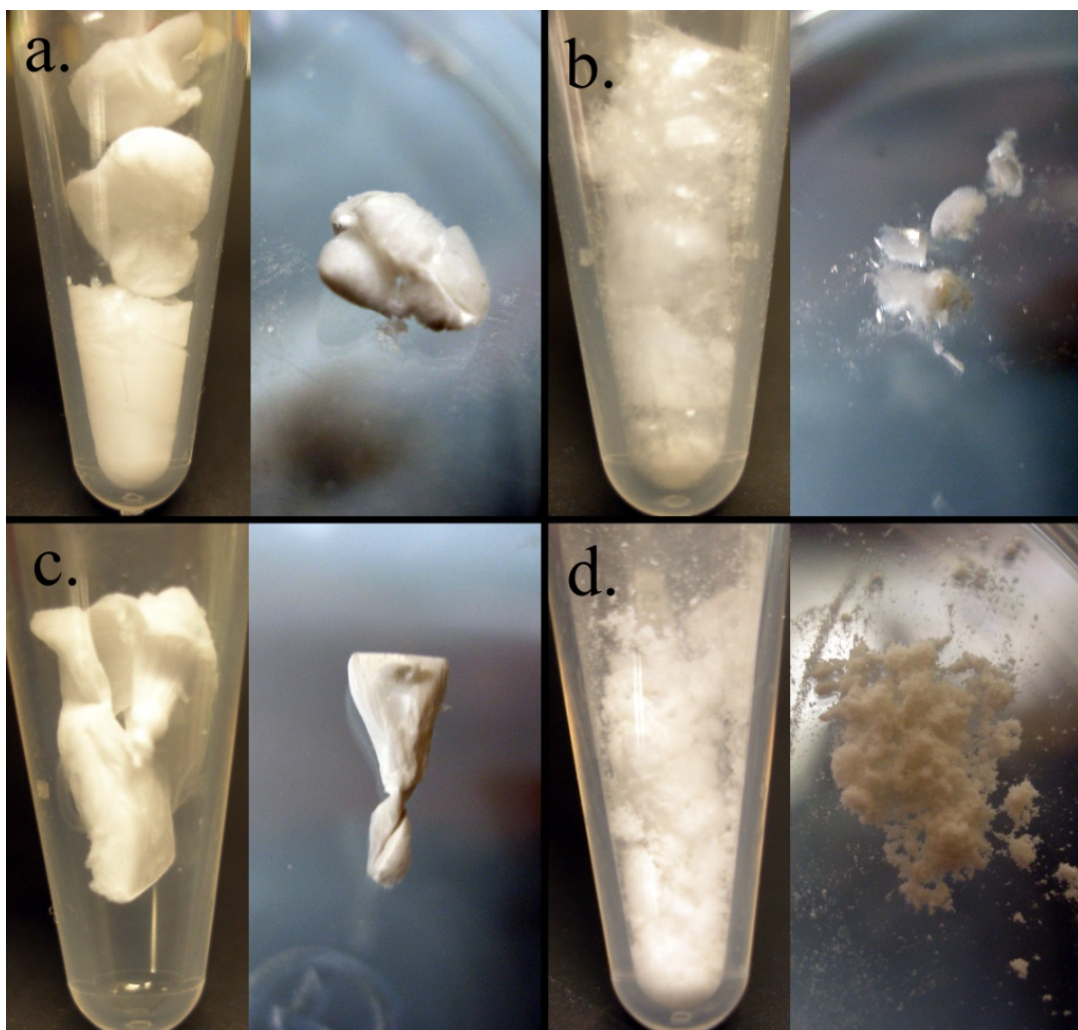


Figure 4.7 Morphologies of formed scaffolds by (a) DSSTPSST-phage with HAP nanorods, (b) HAP nanorods only, (c) DSSTPSST-phage only and (d) wild type phage with HAP nanorods.

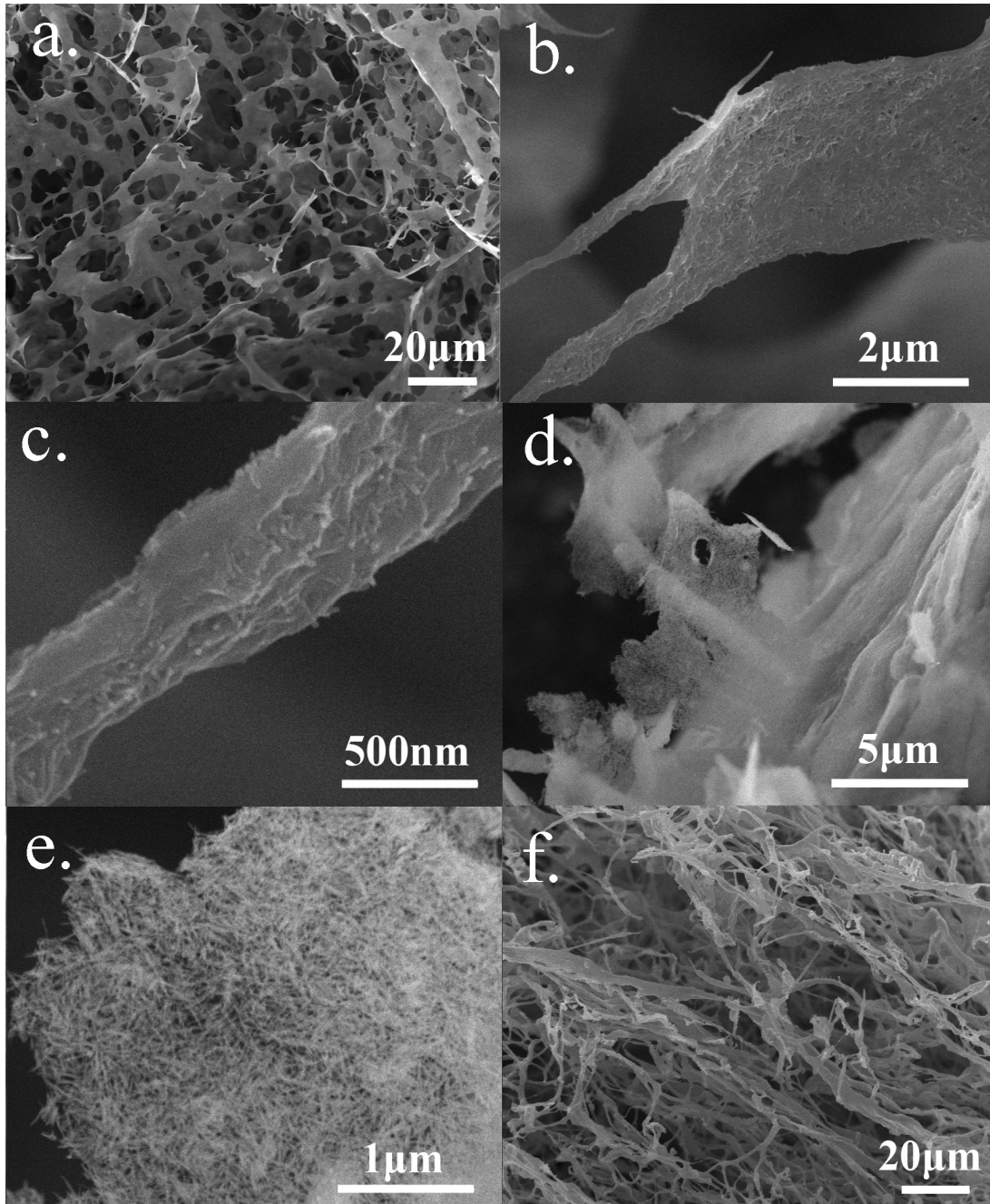


Figure 4.8 SEM images of formed scaffold from (a), (b) and (c) HAP nanorod with DSSTPSST-phage HAP nanorod; (d) and (e) HAP nanorods only; (f) DSSTPSST-phage only.

One fragment from DSSTPSST-phage-HAP nanorod scaffold was characterized under TEM for its detailed structure. In the electron diffraction pattern from figure 9a, the presence of the diffraction arcs corresponding to the 002 plane indicated the c-axis preferred orientation of HAP nanocrystals. This 002 direction (c-axis direction) shared the same direction with the long axis of HAP-phage complex (Figure 4.9a). Since the c-axis of a single HAP nanorod has the same direction with its long axis [186] (Figure 4.9c), a conclusion could be conducted that HAP nanorods in scaffolds were parallel aligned with the same direction as the long axis of HAP-phage complex. In other words, the long axis of HAP-phage complex, the long axis of HAP nanorods and c-axis of HAP nanorods shared the same direction (Figure 4.9b). These facts were consistent with the previous finding that HAP nanorods could be aligned along single DSSTPSST-phages with the same direction.

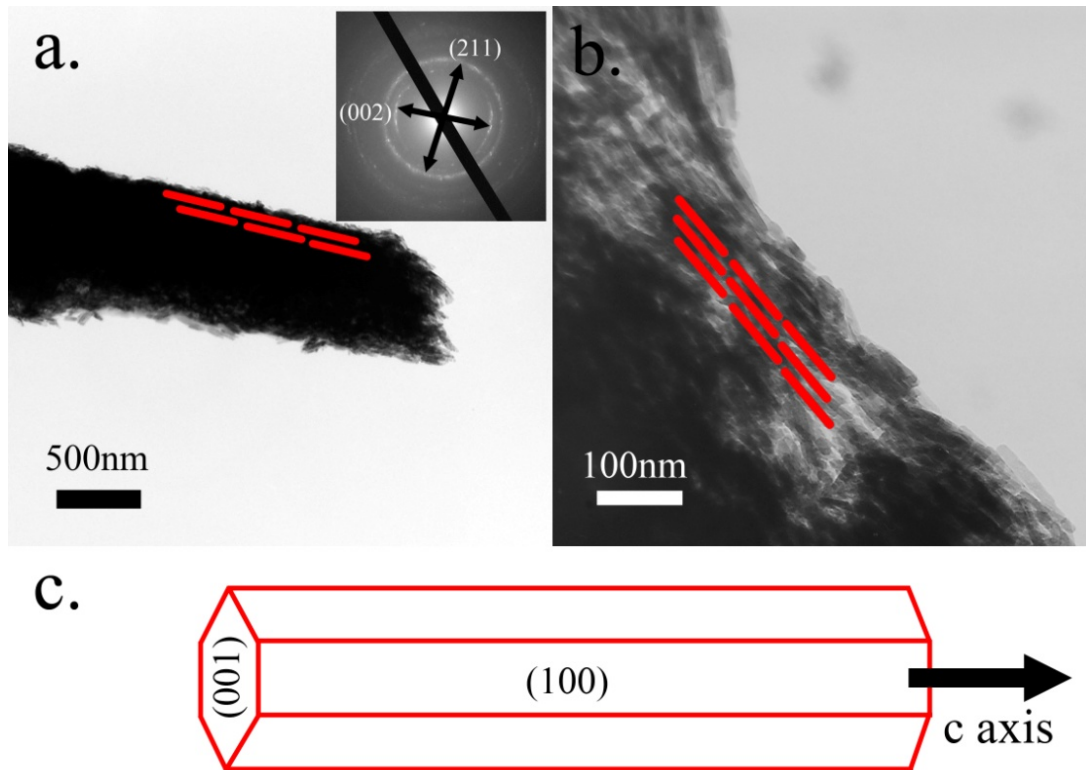


Figure 4.9 HAP nanorods were aligned by DSSTPSST-phages forming a HAP-phage complex with a c-axis preferred orientation. (a) TEM image and diffraction pattern of a fragment from HAP-phage scaffold. The presence of the diffraction arcs corresponding to the 002 plane indicated the c-axis preferred orientation of HAP-phage complex. Red rods indicating HAP nanorods show how they were aligned in scaffold. (b) High magnification image of the fragment edge. Most HAP nanorods were well-aligned. (c) A diagram of the synthesized HAP nanorod. (001) planes at the tips are perpendicular with the (100) faces on its main body. C-axis of each HAP nanorod shares the same direction of its long axis.

4.3.6. Proliferation of MSCs on the HAP-Phage Scaffold

We found MSCs could seed and proliferate on our HAP-phage scaffold and a film of HAP nanorods. From the results of MTT assays, it is

clear that MSCs grew faster on HAP-phage scaffold than on cell culture plate (control). But no significant difference was observed between the proliferation rate of MSCs on the film of HAP nanorods and control. Specifically, after culturing for 3 days, the growth rate of resident MSCs on our scaffold was quantified at OD₄₉₀ by MTT assay showing a value of 0.94 ± 0.047 which was significantly higher ($p < 0.01$) than the value (0.66 ± 0.039) from cells on cell culture plate (Figure 4.10). The quantified growth rate of resident MSCs on the film of HAP nanorods was 0.63 ± 0.019 , showing no significant difference from control (Figure 4.10). We also characterized the morphology of resident cells by SEM. MSCs were found attached to and spreaded on the scaffold (Figure 4.11). In addition, dapi was used to label the cellular nucleolus of resident MSCs, showing MSCs could grow on the scaffold with high density (Figure 4.12). The background blue was from the nonspecific adsorption of the dye onto HAP-phage scaffold. It was impossible to focus all the resident cells at the same time, indicating resident cells were not seeding on a flat layer but on a curving surface of the scaffold.

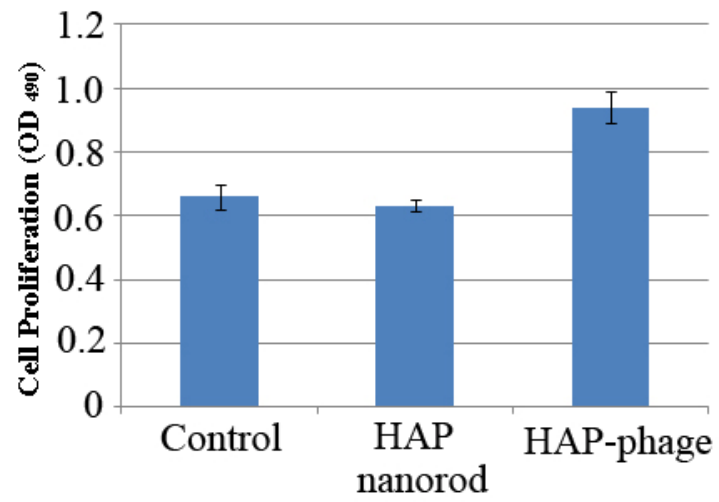


Figure 4.10 The proliferation of MSCs on cell culture plate, a film of HAP nanorods and HAP-phage scaffold.

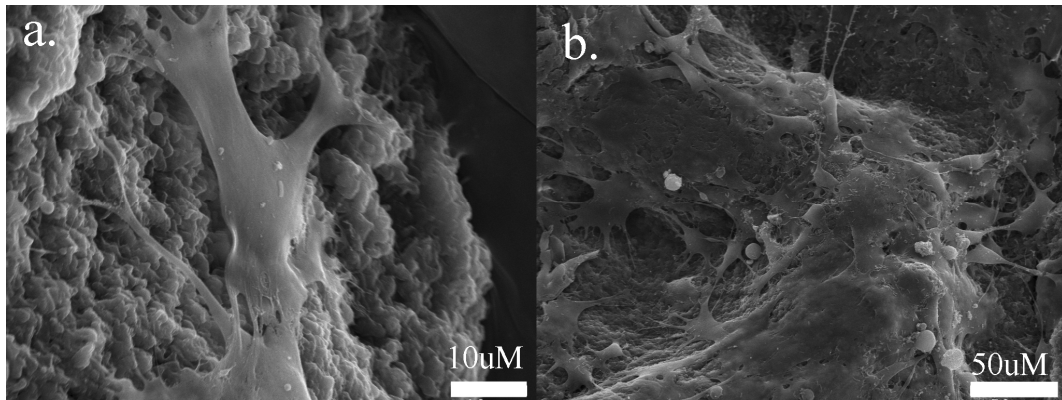


Figure 4.11 Morphologies of MSCs on HAP-phage scaffold after 3 days of culturing. (a) A single MSC on the scaffold. (b) A layer of MSCs on the scaffold.

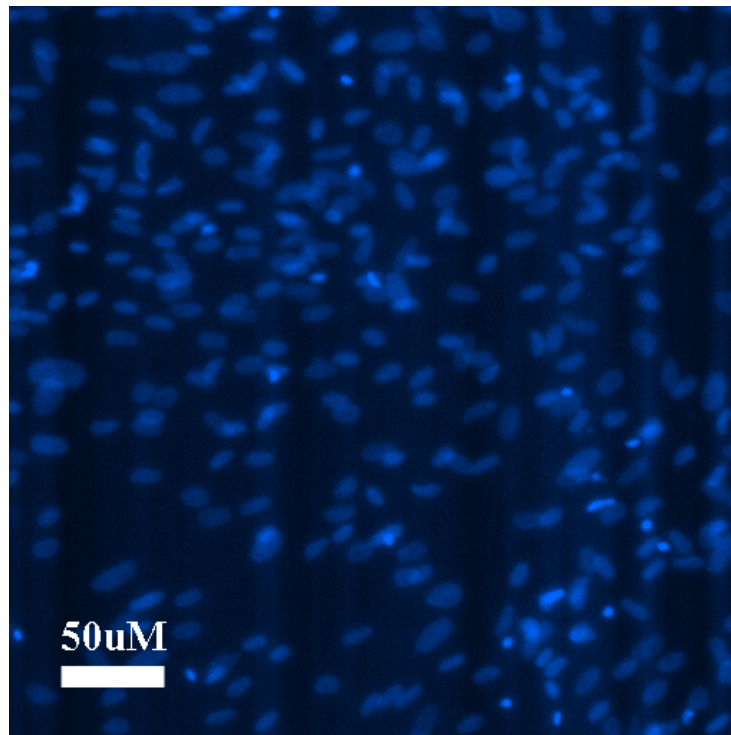


Figure 4.12 MSCs on HAP-phage scaffold. Cellular nucleolus of resident MSCs were stained by dapi.

4.4. Discussion

In order to verify the successful selection of peptides with binding affinity against HAP nanorods during the biopanning process, selected peptides were analyzed by RELIC/POPVID which could estimate the sequence diversity of a combinatorial peptide library based on the sequences obtained from a limited number of randomly sampled members of the library [153]. In principle, selected peptides with the binding affinity against the target should have a diversity value lower than randomly selected peptides from the initial library. We calculated both diversities of affinity-selected peptides and randomly selected peptides from the initial parent library by RELIC/POPVID program. For f8/8 library, our affinity-selected peptides yielded a diversity value of 0.001015 ± 0.000558 , whereas the 100 randomly selected peptides from the initial parent library yielded a diversity value of 0.009139 ± 0.004486 . For f8/9 library, our affinity-selected peptides yielded a diversity value of 0.000943 ± 0.000567 , whereas the 100 randomly selected peptides from the initial parent library yielded a diversity value of 0.011612 ± 0.007429 . Our affinity-selected peptides showed lower diversities than those in the initial libraries. This

analysis strongly supported the successful selection of peptides with binding affinity against HAP nanorods during the biopanning process.

DSSTPSST-phage was verified as the best HAP-binder from previous study, but the interaction details were still unknown. In order to have a better understanding of the detailed binding mechanism, we performed a simulation to describe this interaction. Before the simulation, it was very important to know the interaction interfaces from both HAP nanorods and DSSTPSST-phages. As reported in previous literature, every synthesized HAP nanorod is a single crystal with its c-axis/(001) direction parallel to its long axis [186]. In other words, (001) planes of HAP nanorod are perpendicular with its long axis (Figure 4.9c). Therefore, for every HAP nanorod, two tips are (001) planes and the sidewall is (100) plane which is perpendicular with (001) plane (Figure 4.9c). This conduction is also consistent with the fact that (001) direction of HAP crystal usually is the direction of crystal-growth [195-198]. Because DSSTPSST-phage interacted with the sidewall of HAP nanorods (Figure 4.6b), the interface from HAP nanorods should be (100) plane. On the

other hand, the sidewall of a DSSTPSST-phage is composed of 3900 copies of engineered pVIII coat proteins which are highly ordered with a fixed angle of 21 degree against the long axis of phage [199]. For each engineered pVIII protein, DSSTPSST peptide was displayed on its N-terminal, leaving the sequence of its N-terminal ADSSTPSSTDPAKAA [175]. Since only the N-terminal of pVIII protein can be exposed for interaction, ADSSTPSSTDPAKAA would be studied for its interaction with HAP nanorod. Some simulation results have been done by Lee from Johns Hopkins University (Figure 4.13 and 4.14)

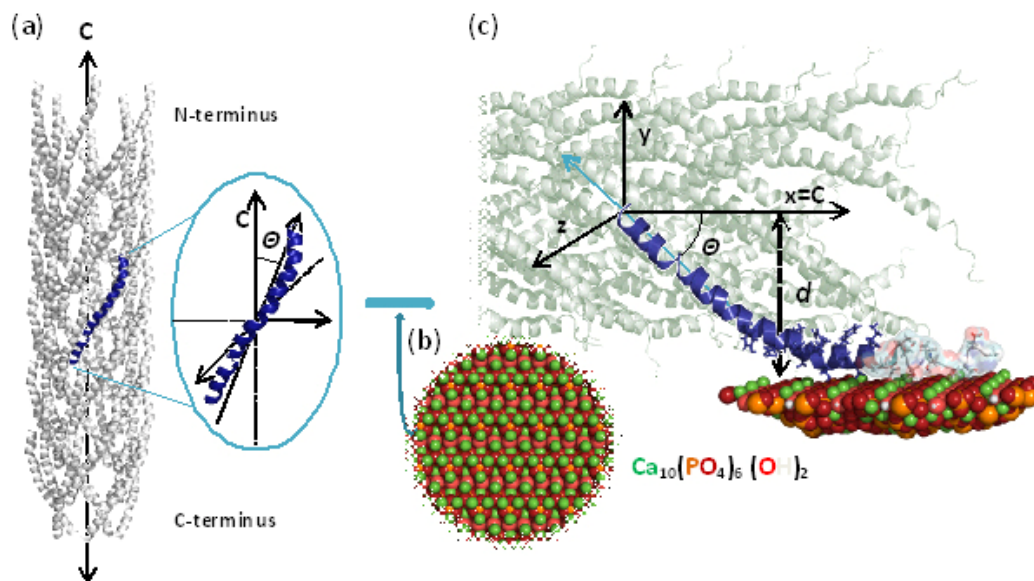
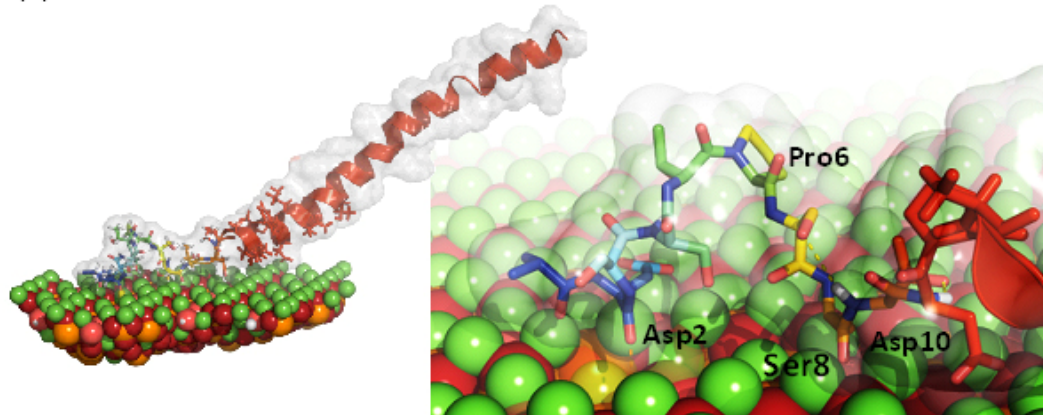


Figure 4.13 Application of geometrical constraints. (a) A view of pVIII coat proteins (PDB ID: 2HI5²), symmetrically located along the virion axis C and the helix tilt angle Θ of a single subunit. (b) The HAp (100) surface

terminating in high calcium density. (c) A model of a single subunit adsorbed to HAp surface under distance d and Θ constraints. The phage structure is included in the background (not during the actual part of the program) to visualize the model in the context of a phage aligning along HAp surface.

(a) **ADSSTPSSTD**



(b) **AESSATQHVD**

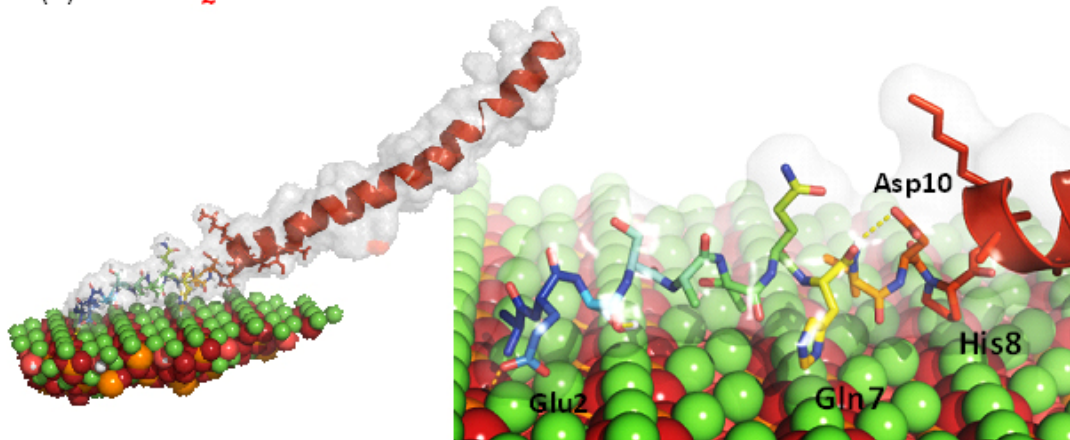


Figure 4.14 Proposed adsorbed-state protein structures. (a) For the DSSTPSST peptide, the N-terminus has a turn-like conformation with a *trans*-proline at the center (Pro6). The pyrrolidine ring is puckered. The proline is directed away from the surface while the side chains and carbonyl oxygens of other residues, especially Asp2, Ser8, and Asp12 are directed toward the HAp surface and are involved in electrostatic interaction or hydrogen bonding with the Ca^{2+} or OH^- , respectively. Orange dash lines represent protein-HAp hydrogen bonds while the yellow ones

show the protein-protein hydrogen bonds. (b) For the ESSATQHV peptide, the N-terminus is extended. While most residues have their side chains pointing toward the surface (e.g. Asp2, Gln7, and His8), the side chain of Asp10 is directed away from the interface.

Affinity-selected peptides can also be applied to identify potential target-binding domains on target-related proteins [179]. It would be interesting if we could identify potential HAP-binding domains from bone related proteins. RELIC/MATCH program was performed to align our affinity-selected peptides (listed in Table 4.1) with the whole sequences of bone related proteins (including statherin, dentin matrix protein 1, osteocalcin, osteopontin, osteonectin, bone sialoprotein and alpha-1 type I collagen) and identified HAP-binding domains on them (Table 4.2). Our identified HAP-binding domains confirmed some previously identified domains such as DSSEEK from statherin [200] and QESQSEQ from dentin matrix protein 1 [117]. These matches indicated that our biopanning method was efficient to identify HAP-binding domains on bone related proteins. In addition, ADSGSSEEK identified from osteopontin was quite similar with DSSEEK from statherin [200], showing potential HAP-binding ability. Other identified potential HAP-binding domains listed in table 4.1

were new domains which could provide additional information for people to study these bone related proteins.

Table 4.2 Identified HAP-binding domains on the bone related proteins.

Bone Related Proteins	Identified HAP-Binding Domains
Statherin	GADSSEEK
Dentin Matrix Protein 1	EDSSSQEGLQS ESRSQESQSEQD DSDSQDSSRS ESNSTGSTSSSEE
Osteocalcin	GAESSKGAA
Osteopontin	VKQADSGSSEEK
Osteonectin	DDGAEETEEE
Bone Sialoprotein	GSSDSSEENGDDSSEE EEETSNEGENNEES NGTSTNSTEAE GNGSSGEDNGE
Alpha-1 Type I Collagen	GDKGETGEQGD DVAPLDVGAPDQE

Recently, two groups have biopanned traditional tip-displayed M13 phage libraries from NEB Inc. against HAP powder and identified two

HAP-binding peptides which are SVSVGMKPSRP [71] and CMLPHHGAC [72]. Our selected HAP-binding peptide, DSSTPSST, is different from those reported peptides for several reasons. Our biopanning target is HAP nanorod rather than commercial micro-sized HAP powder used in the previous work [71, 72]. These differences in size and shape between HAP targets may affect the biopanning process and result in different results. Moreover, in our biopanning process, we used high salt (750mM–1M) PBS buffer as washing buffer instead of traditional washing buffer which contains 0.1% Tween 20. This switching could ensure a strong bonding of the selected phage with HAP nanorods in the following cell culturing process. But this switching may also change the cut-off value of selection in washing process, leading to a distinct result. Besides HAP targets and washing buffer, another possible reason is that we performed the biopanning using landscape phage libraries which are quite different from traditional tip-displayed phage libraries in both displayed locations and inserted random peptides [175]. For assembling HAP nanorod and phage into a bone biomaterial, landscape phage library is superior to the widely used tip-displayed phage libraries for two reasons. First, the

selected HAP-binding phages from landscape phage library have thousands of copies of HAP-binding peptides along the length of the phage while the HAP-binding phage identified by the tip-displayed phage library has only up to five copies of binding peptides at the tip of the phage [71, 72]. Second, to mimic the feature that HAP is assembled along the collagen fibers, the use of the landscape phage library will directly result in the production of phage with HAP-binding peptide along the length of phage, which can be further used as a template to assemble HAP nanorods along the sidewall of phage to form building blocks for further assembly into a bone scaffold. Therefore, using HAP nanorod as the selection target, using high salt PBS buffer as the washing buffer and applying landscape phage library resulted in a different HAP-binding peptide/phage from reported ones.

In fabricated HAP-phage scaffolds, the long axis of HAP-phage complex, the long axis of HAP nanorods and the c-axis of HAP nanorods have the same direction (Figure 4.9). This alignment and packing of HAP nanorods with DSSTPSST-phages greatly mimicked the lowest level of

hierarchy of nature bone that HAP crystals are nucleated and grown within collagen fibrils with their c-axis preferentially parallel to the collagen fibrils. Several groups have co-mineralized HAP with peptides or collagen molecules to mimic the structure of natural bone [107, 201]. However, to the best of our knowledge, no successful mimicking of the basic structure of nature bone assembled from pre-synthesized nano-scaled HAP crystals and polymers have been reported. This strategy not only resulted in a scaffold for supporting cellular proliferation but also provided a novel way to mimic the lowest level of hierarchy of nature bone.

In our work, the proliferation rate of MSCs measured on HAP nanorods without phage was comparable with control (on cell culture plate) (Figure 4.10). It suggested that our synthesized HAP crystallized nanorod with a nano-scaled size (10×150nm) was an excellent inorganic candidate for the proliferation of MSCs. This result was consistent with the previous findings that cellular viability and proliferation of MSCs measured on nano-sized HAP particles (typically 20±5, 40±10 and 80±12 in diameter) were greater than on conventional HAP [202] and even comparable with control

under certain HAP/cell ratio [203]. When cultured on the HAP nanorod-DSSTPSST-phage scaffold, the proliferation of resident MSCs were significantly promoted (Figure 4.10). This promotion was not due to the DSSTPSST-phage itself, because the proliferation of resident MSCs on phage film without HAP was found significantly lower than control. We believe this promotion of the cellular proliferation was ascribed to the alignment and packing of HAP nanorods by DSSTPSST-phage which mimicked the lowest level of hierarchy of nature bone (Figure 4.9). This conclusion was in accordance with the previous finding that the degree of the ordering of surface nano-structures could affect the adhesion, proliferation and differentiation of resident cells [204]. Therefore, these facts suggest that crystallized HAP nanorods with a well-aligned ordering could enhance the proliferation rate of resident MSCs.

Traditional biomaterials for bone healing include bone grafts, polymers, ceramics, metals and combinations of polymers and ceramics [90-96]. Our work represents the first attempt to apply a bottom-up approach from nanotechnology to the fabrication of bone scaffold which

greatly mimicked the lowest level of hierarchy of nature bone. Compared with other bone related biomaterials, our fabricated scaffold assembled from HAP nanorod and its binding phage shows some advantages. First, compared with the conventional micro-sized HAP ceramics, nanophase HAP structures have better mechanical properties [205, 206], higher stabilization during the formation process in the biological milieu, and stronger surface interactions with the host cell/tissue [207]. In addition, hydroxyapatite presence in natural bone is in the form of nano-sized needle like crystals nucleated and grown on collagen fibrils with their c-axis parallel to collagen fibrils [101, 108, 208, 209], so nanophase HAP structures, especially HAP nanorods, can mimic this structure in natural bone. Second, fd phage, a collagen-mimicking biomolecular nanofiber, is superior to other synthetic or natural nanofibers for its chemical stability [45], error-free mass production [45, 48], high surface density (as high as 300-400 m²/g) [45], non-toxicity in human body [210, 211] and matured display technique [173]. Third, based on phage display technique, several peptides can be displayed on the outer surface of one single phage simultaneously, making it possible for an individual nanofiber to present

both HAP-binding peptide and signaling peptide on surface (double display) [46, 47, 174]. The biomimetic scaffold assembled from fd phage can favor both HAP binding and cellular functions. Fourth, this HAP-phage scaffold could mimic the lowest level of hierarchy of nature bone and efficiently promote the viability, adhesion and proliferation of resident MSCs. Fifth, the alignment of HAP nanorods by selected binding phage is a very universal method which can be applied to align other inorganic nanorods for a broad variety of applications. These facts can be considered as important advantages of assembling HAP nanorod and its binding phage to form a scaffold for bone repair. On the other hand, it was very time-consuming to obtain large quantity of selected phages for a large scaffold. For practical applications, the needed time for several grams of phages will be even longer. This is perhaps the main limitation of the scaffold described in this work. We plan to use fermentor to optimize the phage yield and overcome this limitation.

4.5. Conclusion

In summary, we selected some HAP-binding phages by biopanning landscape phage libraries against HAP nanorods. The best HAP-binding phage, DSSTPSST-phage, was picked out and allowed to assemble with HAP nanorods into a novel scaffold by freeze-dry method. In the building blots of the scaffold, HAP nanorods were aligned and packed by HAP-binding phages, mimicking the lowest level of hierarchy of nature bone. This new scaffold assembled from HAP nanorods and HAP-binding phages could efficiently support and promote MSCs seeding and proliferation on it.

Chapter 5 Controlled Growth and Differentiation of Mesenchymal Stem Cells on M13 Bacteriophage Films

5.1. Introduction

Tissue engineering involves a system with specific biochemical functions and cells within an artificially-created scaffold. Finding a proper artificially-created scaffold is vital for achieving engineered tissues. Cellular behaviors depend on substrate surface topography and surface chemistry. Therefore, an effective scaffold includes a well-organized structure that allows cellular adhesion, growth and proliferation and a signaling environment that regulates resident cells' behavior [212-215]. The native extracellular matrix (ECM) contains fibrils ranging from tens of nanometers to micrometers in scale. These fibrils are responsible for the structural support provided to resident cells, and their organized structure guides tissue morphogenesis and remodeling [216]. To mimic this native ECM fibril structure, people have fabricated various nanofibrous scaffolds from biological and synthetic polymers. These scaffolds have tremendous potential for use in tissue engineering applications [217]. The main

advantage of using nanofibers is their larger surface area to volume ratio which allows for greater attachment of ECM ligands and growth factors onto fiber surfaces [218, 219]. Some groups have demonstrated that the patterning of nanofibers could easily be fabricated to affect cellular processes [220, 221]. However, a facile way to introduce signaling motifs onto the fiber surface for controlling cellular processes is still not available.

The M13 bacteriophage is a flexible nanofiber with a width of 6.9 nm and a length of 880 nm. As for its structure, a single stranded DNA is packed into a protein shell composed of 2700 copies of major coat proteins (pVIII) and 5 copies of minor coat proteins (pIII, pVI, pVII, and pIX) at both tips. The beauty of phage display technology is that the surface chemistry can easily be controlled by genetically displaying foreign functional peptides on phage major coat proteins. At high concentrations, both wild type and engineered phages can self-assemble into long-range ordered micro-filamentous structures that effectively mimic native ECM fibrils [222]. Recently, aligned nano-fibrillar structures built from phages have been exploited as novel tissue regenerating materials for controlling

macroscopic cellular behaviors [223, 224]. Some investigations have shown that genetically engineered phage nanofibers can serve as targeting vehicles for delivering drugs and imaging probes for human medical treatments [225, 226]. Currently, there have been no reports of toxic effects found to be caused by phage on mammalian cells. This may be due to the specificity against their host bacterial cells rather than mammalian cells [225, 227]. These facts suggest that phage is a promising candidate for forming cell-supporting scaffolds.

MSCs are multipotent stem cells that can differentiate into osteoblasts, chondrocytes and adipocytes. Because of their broader differentiation ability, a significant number of studies have been focused on MSCs for their potential applications in the repair of bone, fat tissue, cartilage, and more significantly, bone regeneration. [183-185]. By investigating the cellular behavior of MSCs cultured in vitro on a specifically functionalized scaffold, it would be possible to provide a better understanding of the effects that the local niche may have on the stem cell response as well as obtain a strategy for directing the formation of bone in

vivo. So far, it has not been reported that MSCs are capable of growing and differentiating on the phage scaffold. In this work, we employed wild type (WT-) and genetically engineered M13 phages to form films for supporting MSC proliferation and differentiation. For engineered phages, two peptides (PdpLeprrevce and YGFGG) were displayed on the sidewalls of phages. For convenience, the phage displaying PdpLeprrevce is labeled as PD-phage and the phage displaying YGFGG as yg-phage. The PdpLeprrevce peptide is an anionic HAP-binding peptide selected from a biopanning process and YGFGG is the core domain of the typical cell growth peptide known as OGP. Our results indicate that incorporating genetically engineered phages into a complicated scaffold is a feasible method for controlling surface topography and surface chemistry, offering a promising model system for the study of tissue generation and cell differentiation niches.

5.2. Experiments

5.2.1. Display of Peptides on M13 Phage.

We used standard phage display technology to fuse foreign peptides (PdpLeprrevce and YGFGG) to the N-terminus of the major coat proteins (pVIII) of M13 phage. Briefly, the oligonucleotides encoding PdpLeprrevce and YGFGG were amplified by PCR using a replicative form of DNA (RF DNA) as a template. The PCR products were purified using a QIAGEN PCR product purification kit. The purified DNA was digested with both *Nco*I and *Hind*III restriction enzymes and isolated by electrophoresis in a 0.5xTBE buffer and extracted from the agarose gel using a QIAGEN gel DNA extraction kit. The purified PCR products and linear vectors were ligated together at 25°C for 10 minutes using T4 ligase from NEB. The ligation products were then transfected into competent *E. coli* TG1 cells prepared by the CaCl₂ method. 100 µl of transfected bacteria was spread onto an SOB plate containing suitable antibiotics. A well separated clone from the plate was then inoculated into a 3 ml 2xYT broth and incubated at 250 rpm at 37°C. The recombinant phagemid DNA

was isolated using a QIAgen miniprep plasmid extraction kit and followed by sequencing.

5.2.2. Engineered Phage Propagation and Purification.

The phage displaying PdpLeprrevce (pd-phage) and YGFGG (YG-phage) on the major coat was amplified by incubating the respective phage suspension with an *E. coli* TG1 strain. Briefly, two tubes of a 5 ml bacterial culture was incubated with the phages in a 1 liter LB medium in a shaking incubator at 37⁰C overnight. Antibiotics including chloramphenicol (35 µg/ml), tetracycline (35 µg/ml), and kanamycin (70 µg/ml) were used for the selection of the respective plasmid and strains. The overnight culture was first centrifuged at 2400 g for 20 min at 4⁰C. The supernatant was then collected and re-centrifuged at 6700 g for 20 min at 4⁰C. Then a PEG/NaCl solution was added and the suspension was stored in a refrigerator overnight. Phage precipitates were collected at 10100 g for 60 min at 4⁰C, redissolved in TBS buffer and centrifuged at 10100 g for 10 min until clear.

5.2.3. Harvest and Isolation of Rat MSCs.

Bone marrow was obtained from femur of fisher 334. MSCs were isolated by a modification of methods previously described [190, 191]. Briefly, one volume of a bone marrow sample was mixed with two volumes of phosphate-buffered saline (PBS), and the mixture was centrifuged at 1000g for 4 minutes. The supernatant was discarded and the pellet was washed two more times with Dulbecco's Modified Eagle Medium (DMEM; GIBCO BRL, Grand Island, NY, USA). After determination of the cell viability and number using trypan blue staining following lysis of erythrocytes by the addition of 4% acetic acid, 5×10^4 /cm² nucleated cells were plated in T-25 culture flasks in DMEM (low glucose) containing: penicillin G 100 U/mL, streptomycin 100 µg/mL, amphotericin B 0.25 µg/mL, HEPES 2.4 mg/mL, NaHCO₃ 3.7 mg/mL, and 10% fetal bovine serum (Invitrogen, USA) also termed standard growth medium.). The cells were incubated at 37 °C in a humidified atmosphere containing 5% CO₂. After 3 days of culturing, the nonadherent cells were removed by changing the culture media. The adherent cells were grown to 90% confluency to obtain samples, here, defined as passage zero (P₀) cells.

MSCs at P₀ were washed with PBS and detached by incubation with 0.25% trypsin-EDTA for 2 to 3 min at 37 °C. The complete medium was added to inactivate the trypsin. The cells were centrifuged at 1000g for 3 min. The medium was then removed and the cells resuspended in 2 to 5 ml of complete medium. The cells were counted using a hemacytometer and plated as P₁ in 25-cm² flasks at a density of 5×10³ cells/cm². The medium was changed every 2 to 3 days and the cells were passaged every 3 to 4 days. All the cells used for the experiments were P₃.

5.2.4. Phage Film Fabrication

A multilayered phage film was generated using the ESA technique described by Luo et al. [228] with few modifications. The pre-cleaned glass chips were soaked into a poly-lysine solution for 30 min allowing for the adsorption of the first cationic polyelectrolyte layer onto the chips. Subsequently, the chips were washed in ultra-pure water (5 min, continuous water flow) and dried under a pressurized air stream. Then the glass chips were alternately soaked into a phage solution (10¹⁴, 10¹³, 10¹² pfu/ml) and the poly-lysine solution for 7 min each with

intermediate washing in ultra-pure water (5 min, continuous water flow) and drying under a pressurized air stream. The build-up cycle of the multilayered phage-coatings was repeated until a total of 4 double-layers were reached. Last, a final layer of phage was coated as the solution-exposed surface.

5.2.5. Methylthiazoletetrazolium (MTT) Assay.

The cells were plated at a density of 4×10^3 cells/well in 96-well plates in a standard growth medium for 72h. Measurement of cell viability was done by a 3-(4,5-dimethyl thiazol-2-yl)-2,5-diphenyl tetrazolium bromide (MTT) assay. MTT was used as an indicator of cell viability as determined by its mitochondrial-dependent reduction to formazone. MTT (5 mg/ml, 20 μ l /well, Sigma, USA) was then added to the cell cultures for an additional 4 h period. The supernatant was then discarded, followed by the addition of dimethyl sulfoxide (DMSO, 150 μ l/well, Sigma, USA) and agitated for 10 min to dissolve the crystal completely. The values of OD were measured at a 490 nm wavelength on a plate reader (Biotek, USA).

5.2.6. Scanning Electron Microscopy (SEM) for Substrate and Cell

Morphological Examination.

Initial cells were added onto the phage film at a density of 1×10^4 cell/mL. After culturing for 24 hours, the cells on the phage film were washed with 1× PBS, fixed with 2.5% glutaraldehyde in 0.1× PBS for 1 h and washed three times with 1× PBS times. The cells were then dehydrated in a graded series of ethanol (50, 70, 90, and 100%) for 30 min each and left in 100% ethanol until they were totally dried by a supercritical point CO₂. The dried samples were sputter-coated with very thin gold for SEM characterization. The morphology of the phage film as well as the resident cells was monitored by SEM (XL30, FEI Corporation).

5.2.7. Immunofluorescence of Actin and Osteopontin/Osteocalcin.

After 2 weeks of culture in osteogenic media which can induce the differentiation of MSCs into osteoblast cells, the cells on the phage film substrates were fixed in 70% ethanol in 1× PBS for 15 min at room temperature. Once fixed, the cells were washed twice with 1× wash buffer (1× PBS containing 0.05% Tween-20). To permeabilize the cells and 0.1%

Triton X-100 in 1× PBS solution was added for 10 min. The cells were washed twice with a wash buffer. Then, the samples were incubated for 1 h at room temperature in 5% BSA/1× PBS followed by the addition of antiosteopontin (OPN) antibody (1:1000, abcam Biotechnology)/antiosteocalcin (OCN) antibody (1:1000, abcam Biotechnology), and incubated overnight at 4 °C. After incubation, the cells were washed 3 times for 5 min each wash with a 1× wash buffer. Goat anti-rabbit IgG-TRITC (1:500, Santa Cruz Biotechnology) and FITC-conjugated phalloidin (1:40, Invitrogen) in 1× PBS was added for double staining and the cells were incubated again for 1 h at room temperature. The cells were washed 3 times with a 1× wash buffer for 5 min each wash. Then, the samples were stained by DAPI (1:1000, Chemicon) for nucleus staining. The samples were then inverted onto coverslips, mounted, visualized, and photographed by a fluorescence microscope (DM IRB, Leica Microsystems).

5.2.8. Mineralized Bone Matrix Formation Assay

The cells were plated at a density of 4×10^3 cells / well in 96-well plates and coated with varying types of phage. The medium was changed every three or four days and allowed to grow for 2 weeks. Mineralized nodules were stained with Alizarin red S [229]. The dye taken up by extracellular calcium deposits was dissolved in 0.1N sodium hydroxide and quantified spectrophotometrically at 548 nm.

5.2.9. Statistical Analysis

Data was analyzed using SPSS 10.0 statistical software (SPSS 10.0 for windows). One-way-ANOVA and post hoc multiple comparison tests were both performed. Each value represents a mean \pm standard error (SE) in all the figures. A significant level set at 0.05 was defined for the differences between the groups.

5.3. Results

5.3.1. Characterization of the Phage Film

The functional versatility of phage is programmed by their shape, surface chemistry, and displayed peptides, all of which can be controlled

via chemical modification or genetic engineering. Its controllable surface chemistry allows use of phage as a bio-template for directing the nucleation and growth of various inorganic crystals and organic polymers [27, 222]. Its long-rod shape (880 nm by 6.6 nm) and monodispersity drive them to self-assemble into highly controlled periodic nanostructures [222, 223]. Recently, the ability to align resident cells has been integrated into the design of scaffolds for tissue engineering. One promising solution is to introduce topographic micro-grooved structures onto scaffolds. It has been reported that the surface, with a specific groove depth and periodicity, can induce qualitative cell alignment [230-232]. Compared to the disordered surfaces of bio-films generated by other virus particles [233], phage assemblies are much more promising for serving as scaffolds to inducing cell alignment.

In this study, we used the typical layer by layer technique to generate WT-phage films [228]. Positive charged polylysine molecules were employed to modify the chip surface and crosslink negatively charged phage layers. The fabricated film had a slightly rough surface with

alternating phage bundles and grooves. The paralleled phage bundles were distanced apart by grooves (Figure 5.1), giving a microtextured surface morphology. In addition, their sizes could be controlled using different concentrations of phage solution. Specifically, the surface of the phage film generated with a high concentration of phage (10^{14} pfu/ml) showed deeper grooves, bigger bundles and a more ordered pattern than those generated with a lower concentration (10^{12} pfu/ml) (Figure 5.1).

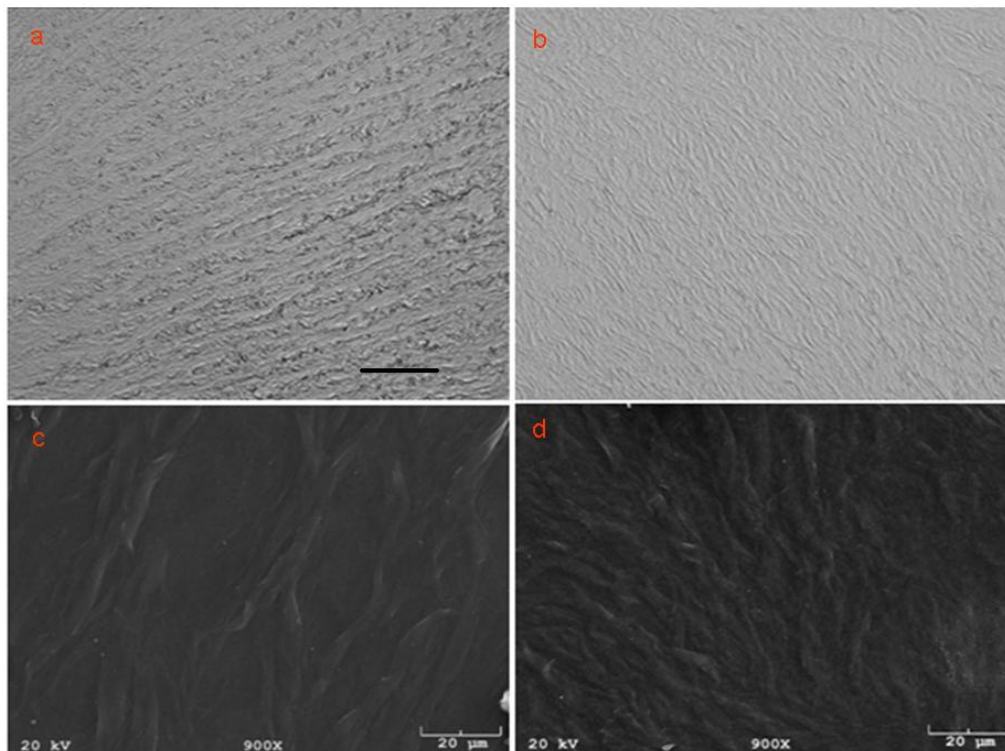


Figure 5.1 M13 phage film obtained at different concentrations (10^{12} , 10^{14} pfu/ml) of phage assembly. The viral films generated large areas with a

high level of organization, with an overall multiplex orientation of the arrays. (a,b,: Optical images, scale bar 200px; c,d: SEM images)

Traditional thin films formed solely from charges are not stable for long periods of time in a culture media which contain plenty of ions. In this study, however, we found that our multi-layer structure could keep the phage film relatively stable in a culture medium for more than 14 days. Engineered phage based films were also synthesized via layer by layer technology and showed the same surface morphology as the WT-phage film. Therefore, we successfully prepared a stable 2-dimensional phage scaffold made with the WT-phage or engineered phage with sufficient parallel grooves on its surface.

5.3.2. Morphology of MSCs on Phage Films.

Preliminary experiments show that grooved and microtextured surfaces can provide directional cues for the morphogenesis of osteoblasts with a preferred direction via a phenomenon known as “contact guidance” [234]. Qualitative cell alignment can be achieved on grooves with a width of 500nm and a depth of 150nm [235-237]. Up to

now, most studies of cell orientation on the surface grooves have been mainly focused on scaffolds built by polymers [238-241]. Only a few successful cases of bio-fiber induced cell alignment have been reported. Phage is a bio-fiber and protein polymer which can form a textured surface with grooves. In order to test what changes could be brought to resident MSCs by phage films, we systemically studied the morphology varieties of MSCs on phage films prepared by varying phages (WT-, PD-, YG-phage) and phage concentrations (10^{14} , 10^{13} , and 10^{12} pfu/ml).

Generally speaking, on both WT-phage and engineered phage (PD- and YG-phage) films, MSCs were significantly stretched and aligned along the phage bundles (Figure 5.2, 5.3, 5.6 and 5.7) leading to a spindle-like cellular morphology. From the SEM images, we can see that the cellular ECM spread mainly on phage bundles, which directed the elongation and alignment of MSCs. However, not all resident MSCs have the exact same morphology. With different phage concentrations and fused peptides (WT/PD/YG), slight variations in the morphologies of resident cells could be found. Specifically, we found that the film

generated with a higher concentration of phage induced a higher stretching degree of order of resident MSCs than with a lower concentration (Figure 5.4 and 5.5). The MSCs on the film made from 10^{14} pfu/ml of WT phage was highly ordered with a spindle-like structure while cells on the film made from 10^{12} pfu/ml of phage were less ordered with a relatively spread morphology (Figure 5.4 and 5.5). Besides phage concentration, fused foreign peptides can also affect cell morphology. MSCs seeded on the PD-phage film have more filopodia and are more spread than cells attached on the WT-phage film or YG-phage film (Figure 5.6, 5.7).

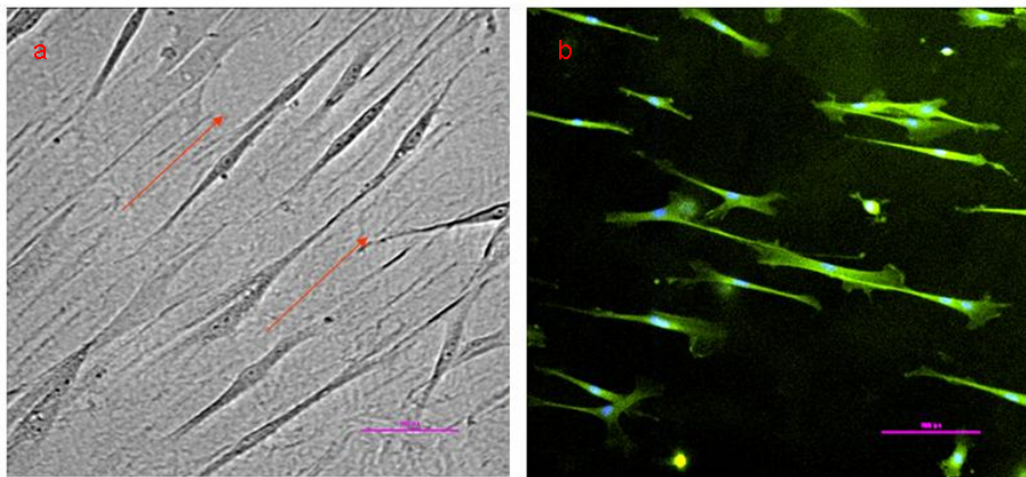


Figure 5.2 The cells elongated along one direction, radiated from the centre of the film. DAPI (blue), Phalloidin (green).

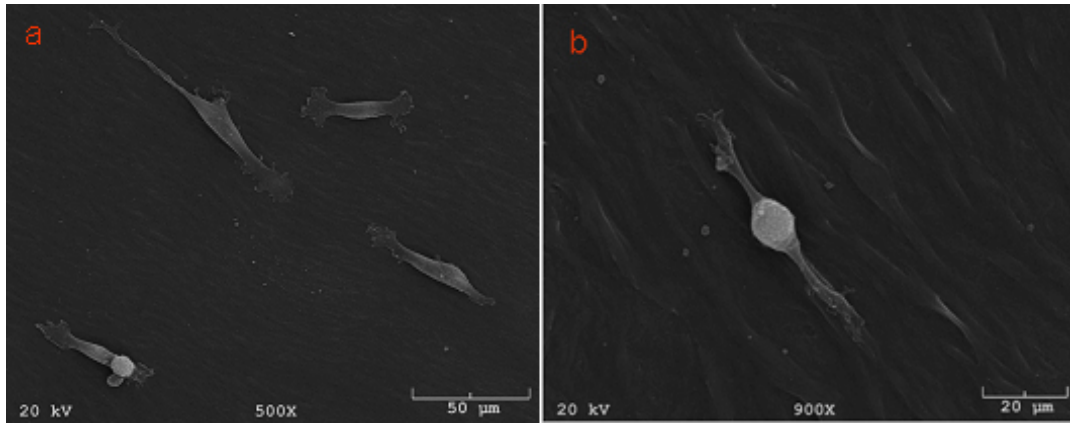


Figure 5.3 An orderly arrangement of cells where the phage bundles are consistent with the orderly nature. a) The phage film was consisted with the phage bundles, b) MSC were elongated on the phage film and attached on the phage bundles. Red arrow shows the phage bundles.

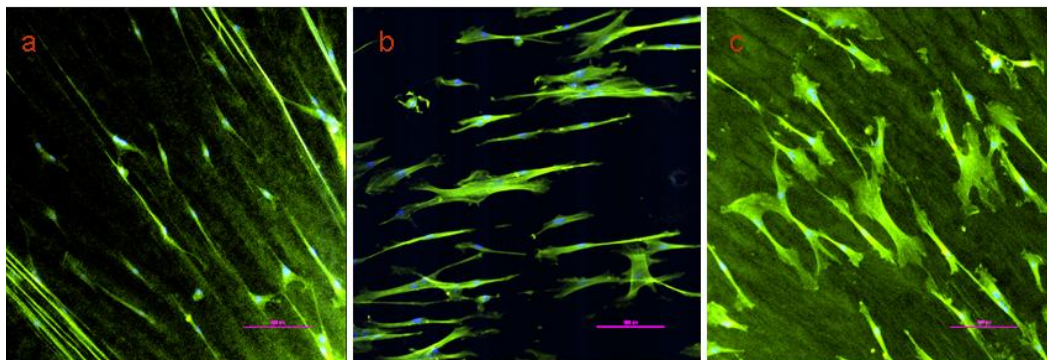


Figure 5.4 The films which were generated with different concentrations (10^{14} , 10^{13} , 10^{12} pfu/ml) of phage can affect the cell alignment and cell stretching degree of order. MSC were arranged at a higher degree of order and extremely stretched at the higher concentration (a) of phage(10^{14} pfu/ml) form, the film compared to the cells, seeded on the film generated at a low concentration (c) of phage(10^{12} pfu/ml). DAPI (blue)

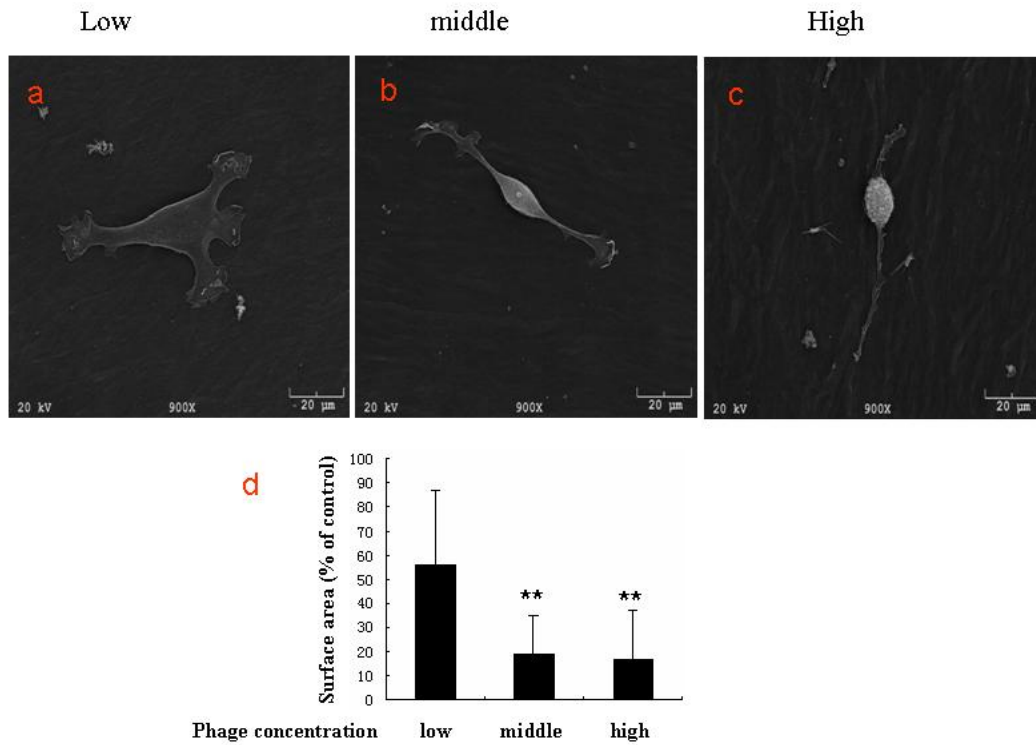


Figure 5.5 The surface area of MSCs cultured on the phage films generated at different concentrations of phage (10^{14} , 10^{13} , 10^{12} pfu/ml). Limited amounts of cells spread out and extraordinary cell elongation was induced at a high concentration of phage film (c). (* $p < 0.05$, ** $p < 0.01$)

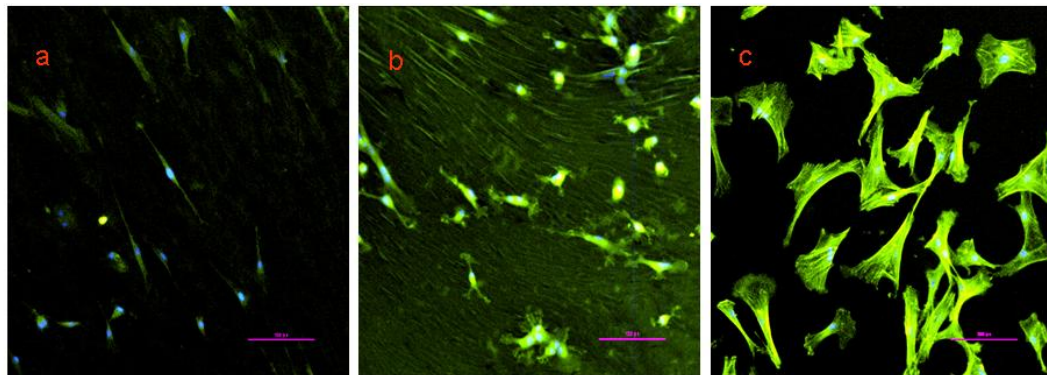


Figure 5.6 MSCs culture on the type of substrates. a) MSCs cultured on the film generated by the wild phage. The cells were elongated and aligned. b) MSCs which were cultured on the film generated by the engineering phage (PdpLeprrvce). The cells were also arranged at a higher degree of order, but displayed multiple pseudopods compared to those on the wild type film (b) and control (c). DAPI (blue), phalloidin (green).

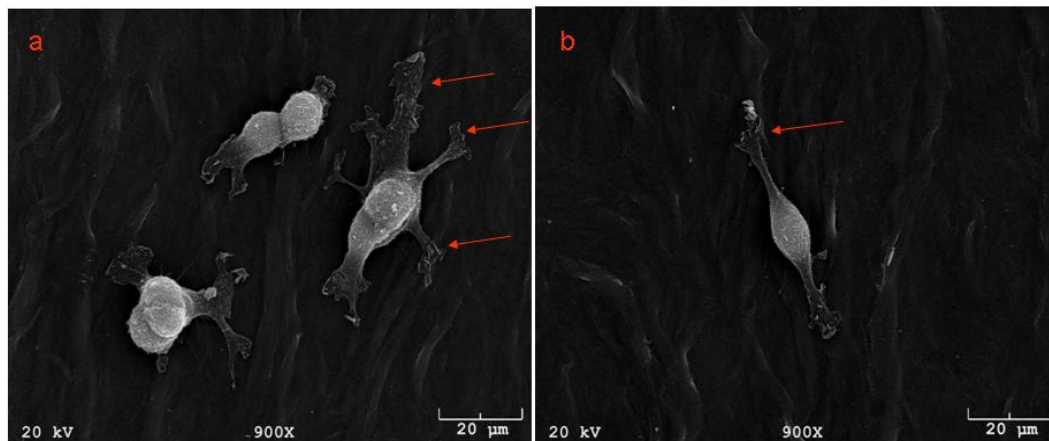


Figure 5.7 a) MSCs cultured on a phage film modified with peptide (PdpLeprrvce). The cells show multiple pseudopods attached to the phage bundles (shown with red arrow) compared to the cells on the wild type film.

5.3.3. Proliferation of MSCs on Phage Film.

It is indispensable for a successful scaffold to support the healthy growth of resident cells. We found that MSCs could proliferate on both WT-phage assembled films and engineered phage assembled films (Figure 5.8). However, the growth rate of the MSCs on phage films

depended on both the phage concentration as well as the peptides displayed on the side wall of phage. After culturing for 3 days and assaying by the MTT method, MSCs seeded on regular plates without phage films showing a higher growth rate than cells located on phage films ($P < 0.01$, $P < 0.01$) (Figure 8). As the concentration of phages increased, the measured OD_{490} value decreased (10^{12} pfu/ml group vs 10^{14} pfu/ml group, $P < 0.05$; 10^{13} pfu/ml group vs 10^{14} pfu/ml group, $P < 0.01$), indicating that the growth rate of resident MSCs decreased. By monitoring the growth of MSCs on WT-, PD- and YG-phage films, we noticed that MSCs on the YG-phage film grew faster than on WT- ($P < 0.01$) or PD-phage ($P < 0.05$, $P < 0.05$) films, however, there is no significant difference between the growth rate of MSCs on WT- and PD-phage films (Figure 5.8).

5.3.4. Differentiation of MSCs on Phage Film.

MSCs can differentiate into several functional cells, such as bone, cartilage, and fat cells. Specific differentiation of resident MSCs towards bone is a hot topic in bone tissue engineering. Therefore, we wanted to test if MSCs could specifically differentiate into osteoblasts on our phage

films. It has been well documented that the specific differentiation of MSCs towards osteoblasts can be characterized by monitoring the increased expression of osteopontin (OPN) and osteocalcin (OCN) [242]. As one member of the bone proteins, OPN serves as a bridge to link cells and hydroxyapatite minerals through its RGD and polyaspartate sequences [243]. OCN is known as being the most sensitive signal for osteoblast differentiation and mineralization. It is expressed during the post-proliferative period, i.e. the ECM maturation period, reaching its maximum expression during mineralization, accumulating in the mineralized bone [244].

In this study, phage films were able to up-regulate the expression of OPN and OCN in resident MSCs under osteogenic media. After culturing for 2 weeks, MSCs seeded on phage films expressed greater OPN and OCN in the cytoplasm (Figure 5.9 b, c, e and f) compared to MSCs that were not on phage films (Figure 5.9 a and d). No significant difference in OCN expression was observed in respective MSCs on the WT-phage film or PD-phage film under osteogenic media (Figure 5.9 e and f). Some

MSCs that were cultured on the PD-phage film for 2 weeks under osteogenic media were found to aggregate into nodules with OPN presented at the periphery (Figure 5.9 c and f). This suggests that these nodule-forming cells were matured osteoblast.

Calcium-containing mineral deposits in the ECM are also markers for testing bone formation. To further support the immune staining results, mineralized calcium-containing matrices prepared under the same conditions were stained using Alizarin red S and quantitatively characterized by a spectrophotometer at OD 548. Figure 5.10 shows both the quantitative and qualitative evidence that the phage films significantly promoted calcium deposition in mineralized nodules. Almost 1.5 times more calcium-containing matrix could be obtained from MSCs on phage films than without phage ($p < 0.01$, $p < 0.01$). However, no significant quantitative difference was observed between MSCs on the WT-phage and PD-phage films. From the above results, we can conclude that the phage films can stimulate the MSCs to differentiate towards osteoblast cells under osteogenic media.

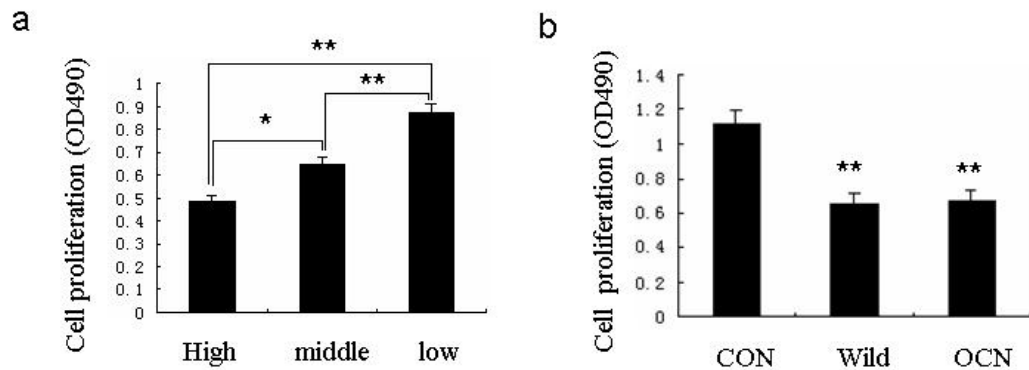


Figure 5.8 MTT assay results. a) MSCs cultured at the low concentration (10^{12} pfu/ml) of phage film grew faster than the cells at the higher concentration (10^{14} pfu/ml) of film. b) MSCs that seeded on the phage film grew slower than those on the glass slides. (* $p < 0.05$, ** $p < 0.01$)

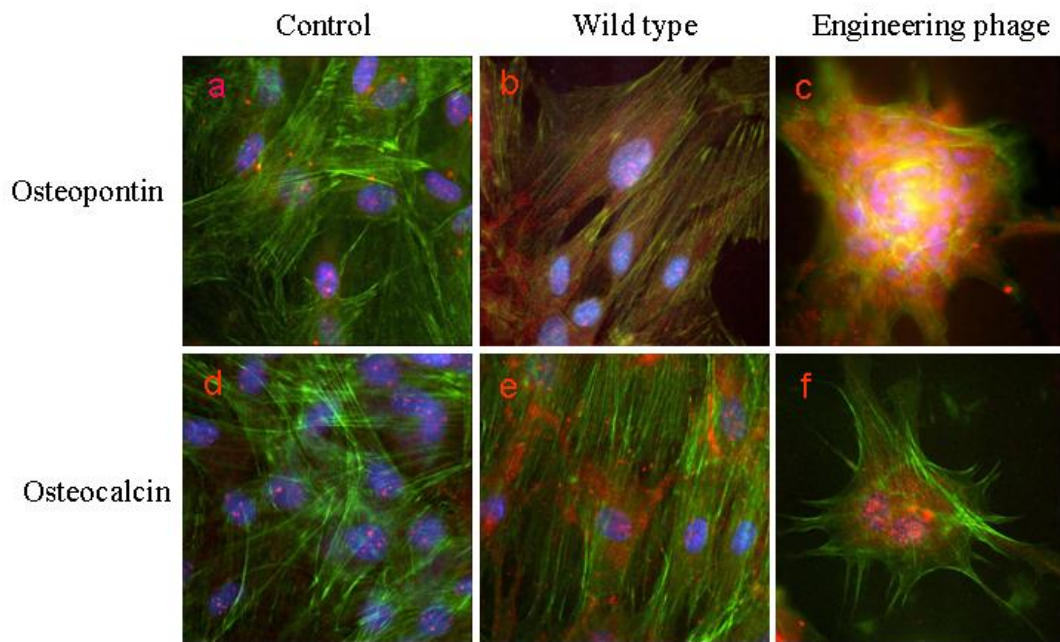


Figure 5.9 The phage film could up-regulate osteocalcin and osteopontin expression compared to the control. The phage film which was modified with the peptide (PDPLEPRREVCE) could stimulate MSC aggregation to form a calcified nodule-like substance. DAPI (blue), Phalloidin (green). Osteopontin and Osteocalcin (red), (Magnification 400x oil)

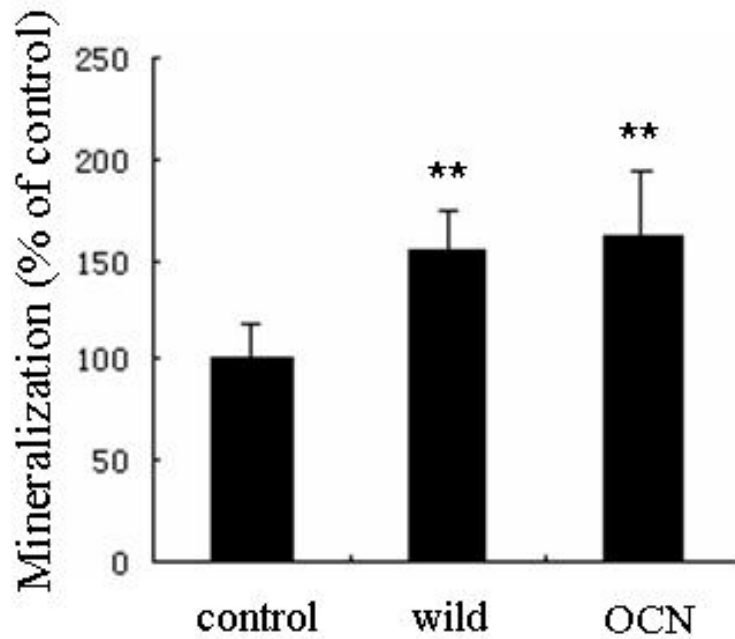
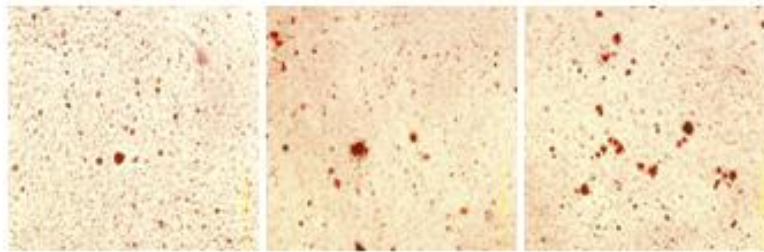


Figure 5.10 Mineralization assayed by Alizarin red S at 14days. ** $p < 0.01$ (Image magnification 100 \times)

5.4. Discussion

Natural filamentous phages are identical protein fibers with negative charges on their surfaces. Their monodispersity in water is unlike any available commercial rod-like colloid or polymer. With certain high concentrations, phages exhibit a cholesteric phase in which all phages are

aligned parallel. On the other hand, it is well known that divalent metal ions or positively charged polymers can laterally aggregate protein rods by cross-linking neighboring fibers. One example is that polylysine can induce the formation of F-actin paracrystal. For phage film fabrication, surface modified polylysine was first dynamically adsorbed onto a glass surface on which a nearby thin layer with free polylysine was formed. Next, free phages were added onto the surface. Electrostatic interactions pulled a large number of free phages close to the polylysine surface, forming a thin layer of highly concentrated phages overlapped with the free-polylysine layer. In this overlapped layer, phages with a relative high local concentration formed a cholesteric phase and were cross-linked by free polylysine leading to parallel phage-polylysine bundles on the surface. Therefore, the parallel bundles observed under SEM were actually phage-polylysine complexes. In this study, we found that the surface of the phage film generated with a high concentration of phage (10^{14} pfu/ml) exhibited deeper grooves, bigger bundles and a more ordered pattern than those generated from a lower concentration (10^{12} pfu/ml). First, it is clear that at a higher concentration, a greater amount of phages were cross-linked by

polylysine on the surface, resulting in larger bundles. Second, grooves were formed between the phage bundles, so deeper grooves corresponded with larger phage bundles induced by a higher phage concentration. Third, with an increasing concentration, phages were exhibited from the isotropic phase to the cholesteric phase. Therefore, phages with a high concentration were more parallel and ordered than at a lower concentration and phage bundles from a high concentration were correspondingly more parallel and ordered.

As we know, cellular morphology depends on both surface topography and chemistry of the scaffolds they live on. In our work, the surface topography of the formed phage films was controlled by the phage concentration; while the surface chemistry was determined by the particular peptide displayed on phage surfaces. Therefore, we can control the morphology of resident MSCs on phage film in our genetically programmable phage involved substrate system by varying phage concentrations and displayed peptides:

1) In our work, MSCs were found to be significantly stretched and aligned along parallel phage bundles (Figure 5.2, 5.3, 5.6 and 5.7) leading to linear cellular shapes. This phenomenon of the orientation and alignment of cells on a micro-groove-like pattern is usually known as contact guidance. Since contact guidance was first discovered around 60 years ago, it has been intensively studied to gain a better understanding of its mechanism. Several possibilities have been proposed including the selective distribution of ECM proteins on the surface, the formation of focal adhesion and the aggravation and alignment of the cytoskeleton (F-actin and microtubule). As we know, ECM proteins usually serve as a carpet for helping cells to adhere and spread onto substrates [245, 246]. The selective distribution of ECM protein aggregates can induce changes in cell morphology and orientation. On our phage films, most of the ECM protein aggregates were found solely attached to phage bundles, which induced the elongation of resident MSCs along these phage bundles. Since the phage film generated with a high concentration of phage (10^{14} pfu/ml) exhibited deeper grooves,

bigger bundles and a more ordered pattern than those generated from a lower concentration (10^{12} pfu/ml), the distribution of ECM proteins on it showed a more unevenly ordered pattern resulting in better ordering and alignment of resident MSCs. In addition, the investigation of the influence of groove-depth on contact guidance has also revealed that deeper grooves could induce higher cellular orientation. Therefore, the building phage concentration could determine the depth of surface grooves and the degree of ordering of phage bundles, both of which could further determine the degree of elongation and alignment of resident MSCs.

- 2) MSCs seeded on the PD-phage film had more filopodia and were more spread out than cells attached on to the WT-phage film or YG-phage film (Figure 5.6 and 5.7). PD-phage was more negatively charged than WT-phage and YG-phage verified from their respective zeta potentials which were determined to be -35mv (PD-phage), -27mv (WT-phage), and -26mv (YG-phage). On the more negatively charged PD-phage film, resident MSCs maintained a

stand-off position from the substrate supported by numerous filopodia (Figure 5.7a) which agrees with other reports. Since filopodia only attached to the sidewalls of phage bundles (supporting information), in order to obtain more supporting points from the substrate, MSCs had to send out more filopodia onto neighboring phage bundles which forced cells to spread across several bundles. For lesser charged WT- and YG-phage films, each MSC could sufficiently attach and align along only one or two phage bundles leading to a spindle-like morphology and fewer filopodia (Figure 5.7b). Therefore, the displayed peptide could determine the surface chemistry of phage film, which could further affect the cellular morphology.

In our experiment, the growth rate of the MSCs on phage films depended on both the building-phage concentration as well as the fused functional peptides (Figure 5.8). As the concentration of building-phages increased (control, 10^{12} pfu/ml, 10^{13} pfu/ml and 10^{14} pfu/ml), the growth rate of resident MSCs decreased (Figure 5.8a). This decrease of proliferation

rate is in agreement with the literature. Specifically, with a microtextured surface, our phage films could restrict cell spreading in one direction, change cell morphology and arrest the cell cycle, resulting in a decrease of proliferation rate of resident MSCs against control MSCs. As previously mentioned, the phage film generated with a high concentration of phage (10^{14} pfu/ml) exhibited deeper grooves and bigger bundles than those generated from a lower concentration (10^{12} pfu/ml). And these deeper grooves and larger bundles could create a higher level of restriction of cell spreading in one direction leading to a lower growth rate of resident cells. Therefore, we could conveniently regulate the cell proliferate rate by varying the building-phage concentration in this phage template system. Besides building-phage concentration, fused functional peptides could also affect the cellular growth rate. We found that MSCs on the YG-phage film grew faster than on WT- or PD-phage films. The YGFGG peptide is the functional domain of the OGP peptide which typically promotes the growth of osteoblastic, fibroblastic and bone marrow stromal cells. It is not surprising that the YG-phage film could accelerate the growth rate of resident MSCs compared with WT- and PD-phage films.

In this work, phage films were able to accelerate the differentiation of resident MSCs towards osteoblast cells which was possibly due to the contact guidance of phage bundles. As we know, when stem cells are busy adhering and growing, their other functions such as differentiation are expected to be depressed; whereas in a stressing condition, they tend to differentiate into a specific lineage to accommodate this stress. Physical stresses from the substrate morphology and topography are able to enhance the differentiation ability of stem cells into a specific cell lineage [247-250]. Yim et al. found that contact guidance can accelerate the differentiation of MSCs on the micro-grooved surface, and the promotion was directly proportional to the degree of contact guidance. Our findings are consistent with the above previous conclusions that: control MSCs on plastic plates grew faster but differentiate slower; while MSCs on phage films grew slower but differentiated into osteoblast cells faster.

The potential advantages of using phage as building blocks are the control of their surface chemistry via genetic modifications. This property can offer further promising opportunities for the study of tissue generation

and cell differentiation niches. Different cellular behaviors were observed in resident MSCs attached on phage films assembled from WT-phage and engineered phages, which are summarized in table 1. Two specific differences could be found: 1) MSCs seeded on the PD-phage film had more filopodia and were spread out more than cells attached on to the WT-phage film or YG-phage film; 2) MSCs on the YG-phage film grew faster than on either the WT- or PD-phage films. As previously mentioned, the sidewall of the phage is composed of 2700 copies of pVIII proteins, so the surface chemistry of the phage is completely dependent on the solution-exposed domain of the pVIII protein. Displaying PdpLeprrevce peptides (containing negatively charged 1 Asp and 3 Glu) onto the solution-exposed domains of its 2700 copies of pVIII protein, makes PD-phage more anionic than both WT-phage and YG-phage (displaying YGFGG peptide). The surface chemistry difference has also been verified from their respective zeta potentials which were determined to be -35mv (PD-phage), -27mv (WT-phage), and -26mv (YG-phage). On the more negatively charged PD-phage film, resident MSCs maintained a stand-off position from the substrate supported by numerous filopodia (Figure 5.7a)

which agrees with other reports. Since filopodia only attached to the sidewalls of phage bundles, in order to obtain more supporting points from the substrate, MSCs had to send out more filopodia onto neighboring phage bundles which forced cells to spread across several bundles. For lesser charged WT- and YG-phage films, each MSC could sufficiently attach and align along only one or two phage bundles leading to a spindle-like morphology and fewer filopodia (Figure 5.7b). The YGFGG peptide is the functional domain of the OGP peptide which typically promotes the growth of osteoblastic, fibroblastic and bone marrow stromal cells. It is not surprising that the YG-phage film could accelerate the growth rate of resident MSCs compared with WT- and PD-phage films. However, the growth rate of MSCs on the YG-phage film was still lower than cells on polypropylene, the positive control. This suggests that even with cell growth peptide, cells on phage films still grow slower than on traditional polypropylene plates. No significant difference in OCN and OPN expression was observed between the MSCs on the WT-phage film and PD-phage film under osteogenic media (Figure 5.9 e and f). We'll import

more peptides into this system to study cell differentiation niches in the future studies.

5.5. Conclusion

We employed wild type and genetically engineered M13 phages to form films for supporting MSC proliferation and differentiation. M13 phage films can not only be employed as 2-dimensional scaffolds for MSC proliferation and differentiation but also as an ideal model for the study of tissue generation and cell differentiation niches. These films are ideal for the following reasons: 1) cells can grow on phage films; 2) the phage film is able to induce contact guidance; 3) the surface topography is controllable by using different concentrations of phage; 4) the surface chemistry such as surface charges, can be programmed through genetic modifications; 5) introducing functional peptides like OGP into the substrate film is easy to achieve, providing a facile approach for studying cell differentiation niches. As for in vitro cell culturing, cellular morphology, proliferation and differentiation are the two main factors that affect are

surface topography and surface chemistry. Both of them could be controlled in our genetically programmable phage substrate system.

Chapter 6 Novel Colloidal Crystals Self-Assembled from Rodlike

Bacterial Pili Particles

6.1. Introduction

Colloidal crystals are three-dimensional (3D) periodic arrays self-assembled from colloidal particles in suspension. They have important applications in the synthesis of ordered nanostructures and production of light elements, especially photonic crystals [251]. Besides those applications, they serve as a particularly attractive experimental system for fundamental studies of crystal growth [252]. Up to now, most fabricated colloidal crystals were assembled from spherical colloidal particles [253]. So far, no rodlike colloidal particles have been used for the formation of colloidal crystals. However, in nature, some rodlike molecules such as actin-filaments in muscle cells self-assemble to perform important functions [254]. Here, we report the self-assembly of rodlike type 1 bacterial pili particles into colloidal crystals and their use in biotemplated nanomaterials synthesis.

Type 1 bacterial pilus is a rigid, straight, naturally occurring protein nanorod (6-7 nm wide and 1-2 μm long) that can be detached from bacterial cells [79]. It is helically assembled from more than 3000 copies of protein subunit called fimA with 27 subunits in 8 turns. It has an anionic surface with isoelectric point of 3.92 [87]. Its biological function is to assist the adhesion of bacteria to solid surface. Although self-assembly behavior of pili was observed occasionally long time ago [87], 3D crystals made of multiple layers of pili have never been reported. Herein, we report a reproducible approach to the formation of colloidal crystals from rodlike type 1 bacterial pili by varying the chemical compositions and concentrations of inducer molecules in aqueous pili solutions (Figure 6.1).

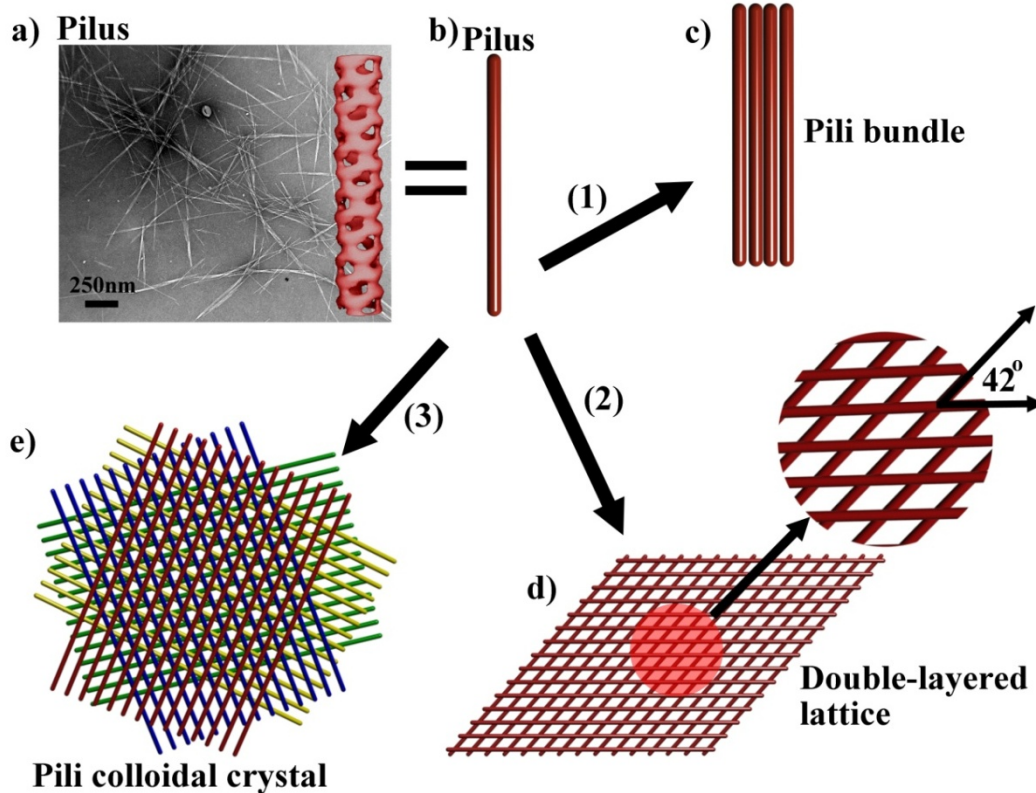


Figure 6.1 Self-assembly of pili into 1D bundles, 2D lattices and 3D crystals. a) TEM image and 3D model (modified from [79]) of pili. b) Pilus. c) pili bundles. d) double-layered pili lattice. The neighboring layers of pili have a fixed angle of 42° . e) A 4-layered pili crystal. A green layer of parallel pili was formed, followed by the assembly of a yellow layer of pili on top of the green layer with a twist angle of 42° . After that, a blue and red layer are deposited in turn on top of the yellow layer and blue layer with the neighboring layer twisted at the same angle of 42° , resulting in the formation of a 4-layered crystal. Inducing agents include (1) $>160\text{mM}$ hexamethylenediamine; (2) 80mM hexamethylenediamine; (3) 80mM pimelic acid or 1,3-propanedisulfonic acid.

6.2. Experiments, Results, and Discussion

In order to induce the self-assembly, pili solution was diluted to a concentration of $OD_{280}=0.25$ in specific aqueous solutions (Table 6.1) and allowed for incubation at 4 °C. In the presence of a high concentration of hexamethylenediamine molecules (>160 mM), pili solution became cloudy within 1 h because pili were self-assembled into bundle structures in which pili were parallel aligned (Figure 6.1c and 6.2a). After pili were incubated in a lower concentration (80 mM) of hexamethylenediamine, the solution was clear in the first 2 days and became cloudy after 3 days, suggesting pili slowly self-assembled into large aggregates. On day 7, precipitates appeared in the solution, indicating a continuous growth of pili assemblies. TEM examination revealed the formation of double-layered pili lattices which were made up of two twisted individual layers. Each layer is made of parallel pili and pili from the two adjacent layers are at a fixed angle of 42° (Figure 6.1d and 6.2b). The center-to-center distance between the neighboring pili in the same layer was about 13 nm.

In the presence of 80 mM pimelic acid, the pili solution stayed clear until day 6. After day 6, the solution became cloudy and small precipitates appeared due to the formation of highly ordered pili crystals (Figure 6.1e and 6.2c). The colloidal crystals were made up of at least 4 alternately twisted layers of parallel pili with the neighboring layers having a fixed angle of 42° (Figure 6.1e and 6.2d). This highly ordered crystal structure, made of vertically stacked layers of pili with a twist angle of 42° between neighboring layers, could be verified by the 2D fast Fourier transform (2D-FFT) image (Figure 6.2c-d). In a 5-layered lattice, the angle between the direction of pili in layer 1 and the direction of pili in layer 5 is only about 12° which makes them almost overlapped in TEM images. Therefore, when the number of layers is more than 4 in pili crystals, it is difficult to identify the number of layers by simply using 2D TEM imaging (Figure 6.2d). But FFT image can be used to identify the number of pili layers. The FFT image (inset in Figure 6.2d) shows a total of 17 layers of pili in the crystal with a fixed twist angle of 42° between neighboring layers.

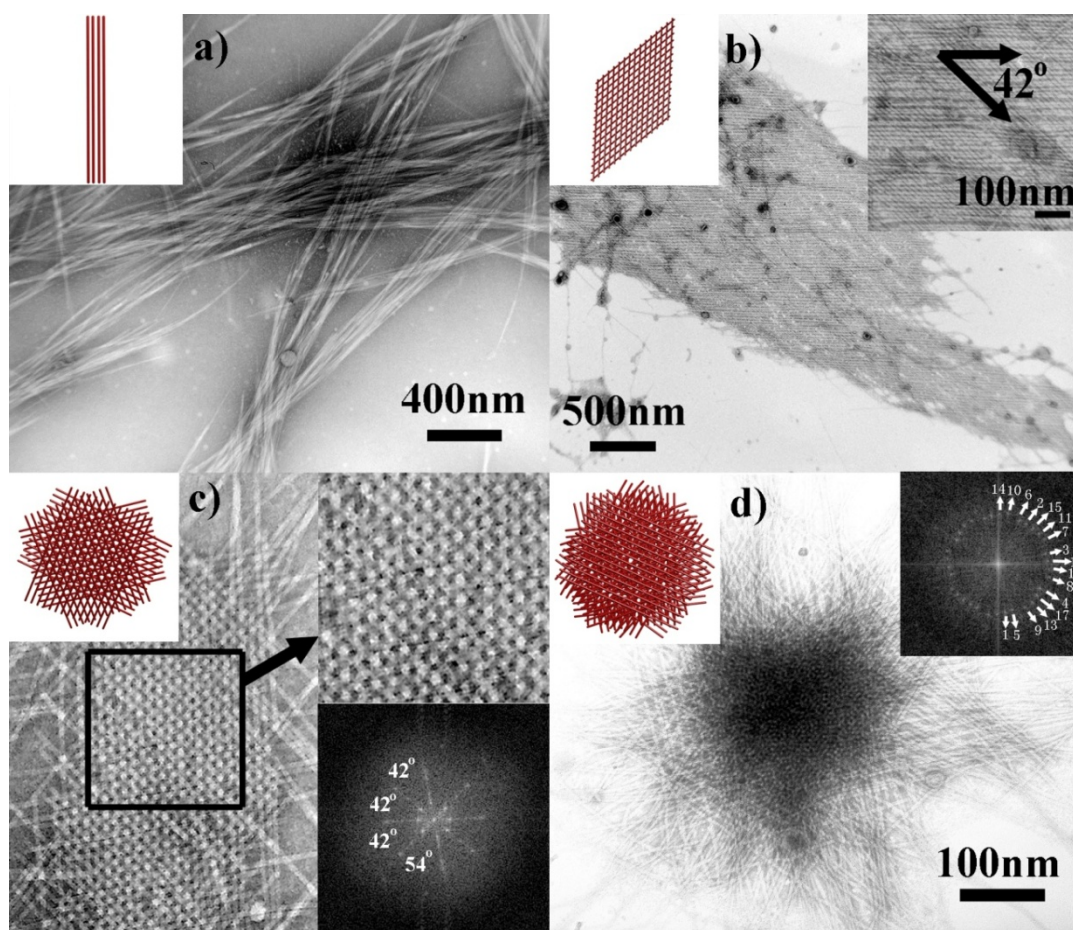


Figure 6.2 TEM images of pili assemblies. a) bundles. b) A double-layered lattice with a fixed twist angle of 42° between two layers. c) A 4-layered crystal. FFT (inset) of selected area confirms the highly ordered structure and the twist angle between neighboring layers. d) A 17-layered pili crystal. FFT (inset) confirms there are 17 layers of pili in the crystal with fixed twist angle of 42° between adjacent layers. The spot corresponding to each layer is marked in the 2D-FFT image.

Our work shows that the careful choice of inducers in the pili solution can control the self-assembled nanostructures (Table 6.1). First, we found pili could self-assemble only in the presence of Mg^{2+} ,

hexamethylenediamine, pimelic acid or 1,3-propanedisulfonic acid, but could not in the presence of other species we tested (Table 6.1). Besides Mg^{2+} , those successful assembly-inducers have either positively or negatively charged two distal ends connected by a long central carbon chain. Molecules with two neutral ends (1,4-bis(2-hydroxyethyl)piperazine) or with one neutral end and one negative end (HEPES) or even with one positive end and one negative end (6-aminocaproic acid) could not induce the assembly of pili. These facts suggest that only molecules with the same charges on both sides could induce the assembly of pili. Second, the concentrations of the inducers in pili solutions could control whether the self-assembled nanostructures to be 1D bundles, 2D lattices or 3D crystals. High concentration of multivalent positively charged inducers (Mg^{2+} and hexamethylenediamine) could induce the self-assembly of pili into bundles very fast by electrostatic interactions (within 1 h). Double-layered pili lattices were formed in a 80 mM hexamethylenediamine solution after a longer incubation (3 days). Here, only with a proper concentration, hexamethylenediamine could induce the formation of double-layered pili lattices. If the concentration was too high, only bundles

were produced; and if the concentration was too low, no assemblies were observed. Therefore, we believe the formation of double-layered pili lattices resulted from the addition of a proper amount of divalent positively charged long-chain ions which slowly and loosely cross-linked the anionic pili from neighboring layers (3 days). Such mechanisms were consistent with those in the assembly of F-actins [255].

Multi-layered 3D pili crystals could never be induced in hexamethylenediamine solution no matter how long we incubated the system or what concentration we used. They were formed in the presence of either 80 mM pimelic acid (7 days) or 80 mM 1,3-propanedisulfonic acid (20 days) (Table 6.1), both of which have negative charges (-COOH/-SO₃H) at two distal ends of the inducer molecules. These inducer molecules could not electrostatically attract pili like hexamethylenediamine. Instead, they slowly precipitated pili by a combination of possible activities such as competition with pili for water, hydrophobic exclusion of pili and lowering the solution dielectric constant [256]. Since they couldn't interact with pili directly, the nucleation and growth of pili crystals were relatively

slower. Compared to 1,3-propanedisulfonic acid, pimelic acid has a better precipitating efficiency, so the growth rate of pili in its solution (7 days) was faster than in 1,3-propanedisulfonic acid solution (20 days). To the best of our knowledge, these two reagents have never been used in inducing colloidal crystals before.

We also found pili crystals grew in a layer-by-layer fashion [257] through 2D nucleation on surfaces (Figure 6.3a). This 2D nucleation strongly slowed the rate at which crystal growth occurred [258]. Pili could still be crystallized into crystals with M13 phage as a contaminant (Figure 6.3b) which have similar diameter (7 nm) and length (1 μ m) as pili. This fact suggested that there were specific interactions between neighboring pili layers which make them recognizable with each other and the presence of M13 phage could not disturb the assembly of pili into 3D crystals. In order to test the importance of molecular recognition between pili in the process of crystallization, bacterial flagella and M13 phages which do not have recognition between themselves were incubated under

the same condition. As expected, no crystals were formed from flagella or M13 phages (Figure 6.3c and d).

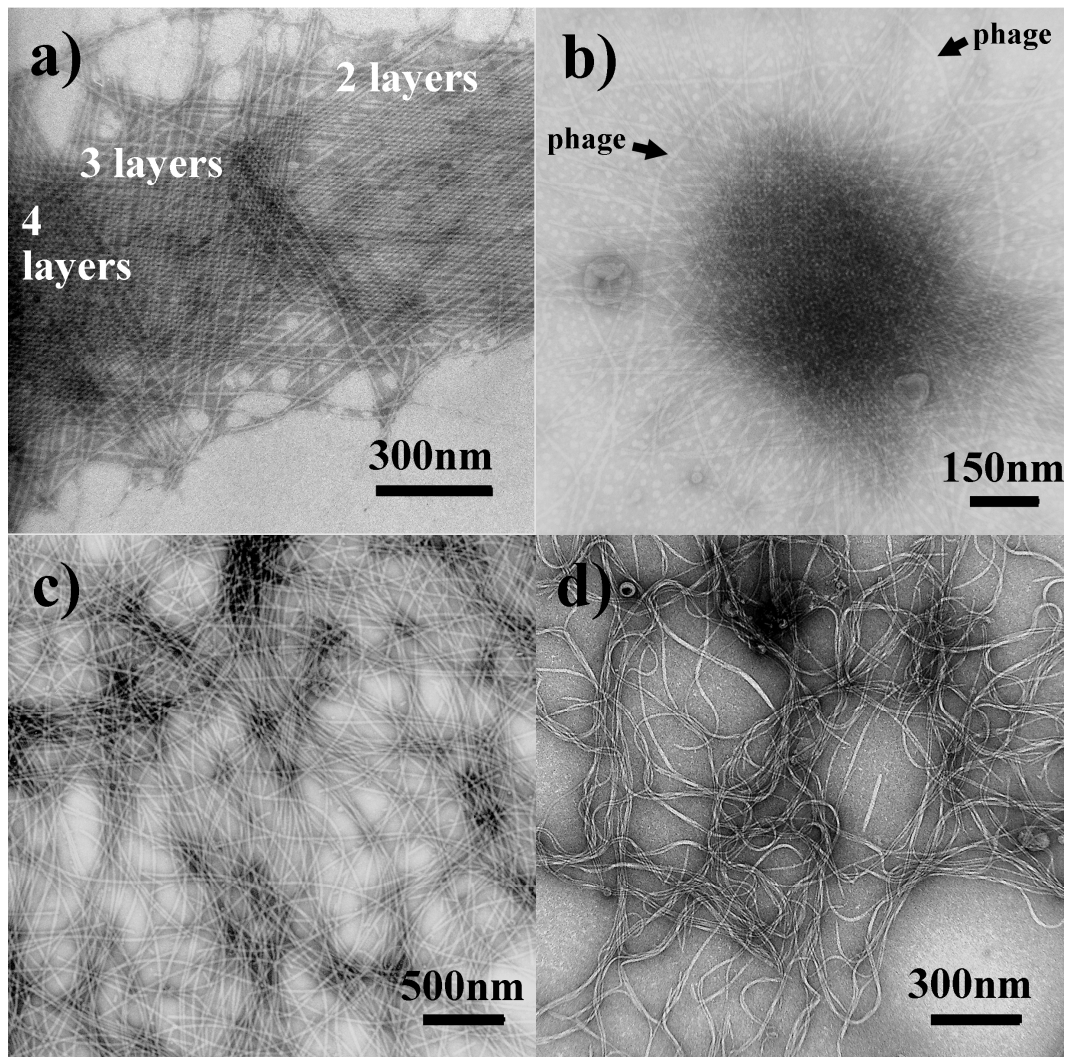


Figure 6.3 a) Evidence showing that the crystallization of pili took place in a layer-by-layer fashion. b) Pili were crystallized into crystals with M13 phage as a contaminant. c) Bacterial flagella after incubation in 80 mM pimelic acid. d) Phages after incubation in 80 mM pimelic acid.

We believe the molecular recognition driving the formation of the pili crystals arises from the molecular structures of pili. On each pilus, there are a set of alternating ridges and grooves with a pitch angle of 21° (Figure 6.5a). When pili self-assemble with each other, the ridges of pilus A must make an interlocking fit into corresponding grooves of pilus B. And this can happen only when pili A and B are at an angle of $2 \times 21^\circ = 42^\circ$ (Figure 6.5b). This angle is same as the twist angle of 42° found in double-layered lattices or multiple layered crystals. This molecular structure based recognition favor the nucleation and growth of pili crystals. The molecular structure directed self-assembly was also observed in F-actin [259].

Our study suggests that there are several requirements for the synthesis of colloidal crystals from rodlike particles. First, weak but specific interactions between rodlike colloidal particles are necessary. Otherwise, only bundle structures will be formed instead of highly ordered crystals. An example is that phage fibers can only form parallel bundles in the presence of same inducers. Second, rodlike particles should be

straight and rigid. Phages are semi-flexible and flagella are not straight, so they could not form highly ordered structures. Third, special inducer molecules are needed (Table 6.1). These requirements can guide us to synthesize new colloidal crystals from rodlike colloidal particles.

Pili bundles, double-layered lattices and multi-layered crystals are well-organized biotemplates (Figure 6.2) for nanosynthesis. Here silica was selected as a model inorganic nanomaterial for this purpose. Specifically, all pili assemblies were fixed in 1% glutaraldehyde solution and then 3-aminopropyltriethoxysilane (APTES) and tetraethyl orthosilicate (TEOS) were then added in turn under stirring so that silica could uniformly be coated onto them [260]. Specifically, APTES (2×10^{-3} mmol) was added to fixed pili assemblies solution. The solution was gently mixed on a vortex mixer. Then, it was put into an ice-water bath for 3–5 min. To this solution, TEOS (2.5×10^{-2} mmol) was added under stirring for at least 3 min. The mixed solution in a reaction tube was left in an ice-water bath for around 15 min or until white precipitates appeared (in 15–20 min). The reaction tube was then left at room temperature for around 8

hours. The products were purified by centrifugation at 4500g for 10 min and washed with ethanol and water for several times. Silica-pili hybrid nanorods with multi channels, nanorhombuses and nanoflowers were produced by using pili bundles, double-layered pili lattice and multi-layered pili crystals as templates, respectively (Figure 6.4). Silica coatings were confirmed by the energy dispersive X-ray (EDX) analysis (Figure 6.4d). The fabricated 2D silica nanorhombuses and 3D silica nanoflower have ordered pili lattice inside, which could be easily removed by calcinations for further applications.

Before silica precursors were added, pili assemblies were first fixed and cross-linked by glutaraldehyde so that glutaraldehyde molecules reacted with amino groups from pili but not carboxyl groups. Therefore, the remaining carboxyl groups turned pili surface to be highly negative so that APTES could easily absorb onto pili assemblies. The close contact of APTES with the pili surface enhances the hydrolysis of APTES to form silicic acid, which functions as nuclei for subsequent silica growth [260]. After the addition of TEOS, polycondensation of TEOS and the growth of

silica will be based on the silica nuclei on the pili surface, ultimately resulting in the formation of pili-silica hybrids.

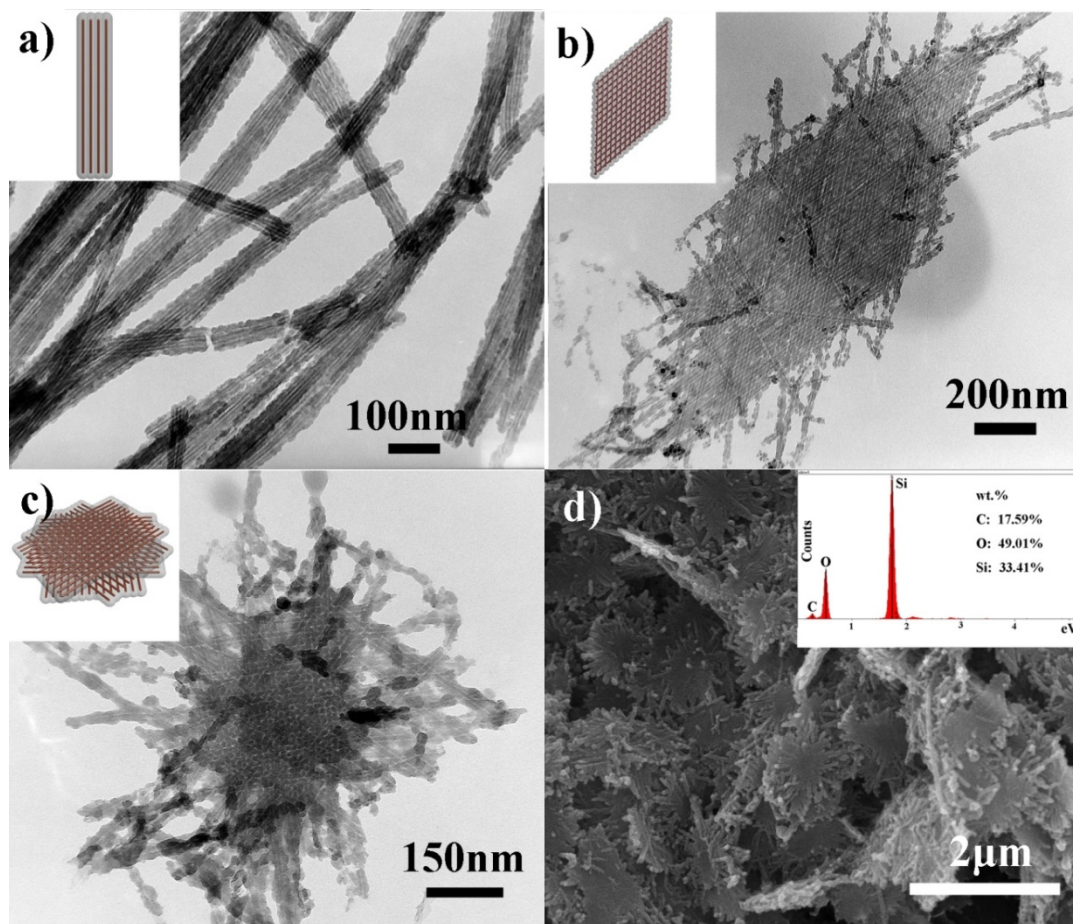

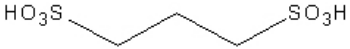

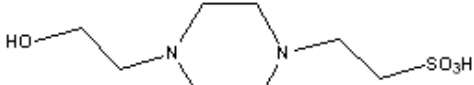
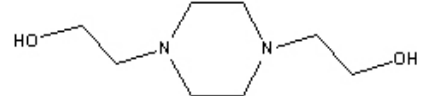



Figure 6.4 Silica-pili composites formed by templating silica nucleation on pili assemblies. a) Silica coated pili bundles. b) A fragment of a silica coated double-layered pili lattice. c) A silica coated multi-layered pili crystal. d) SEM image and EDX analysis of composites from c). EDX analysis (inset) shows elemental composition of Si and O with a proper wt%: O%=49.01%, Si%=33.41%.

Table 6.1 Chemical compositions of the aqueous solutions of pili were tried for the assembly of pili into 1D bundles, 2D double-layered lattices and 3D multi-layered lattices. Pili concentration was kept constant at $OD_{280}=0.25$. “-” indicates no corresponding structures are formed.

Reagents	Bundle	Double layered lattice	Multi-layered lattice
 Hexamethylene-diamine	>160mM (1 day)	80mM (4 days)	-
 1,3-propanedisulfonic acid	-	Few 80mM (20 days)	80mM (20 days)
 Pimelic acid	-	Few 80mM (7 days)	80mM (7 days)
 HEPES	-	-	-
 1,4-bis(2-hydroxyethyl)piperazine	-	-	-
 6-aminocaproic acid	-	-	-
Mg^{2+} Magnesium ion	>50mM (10min)	-	-

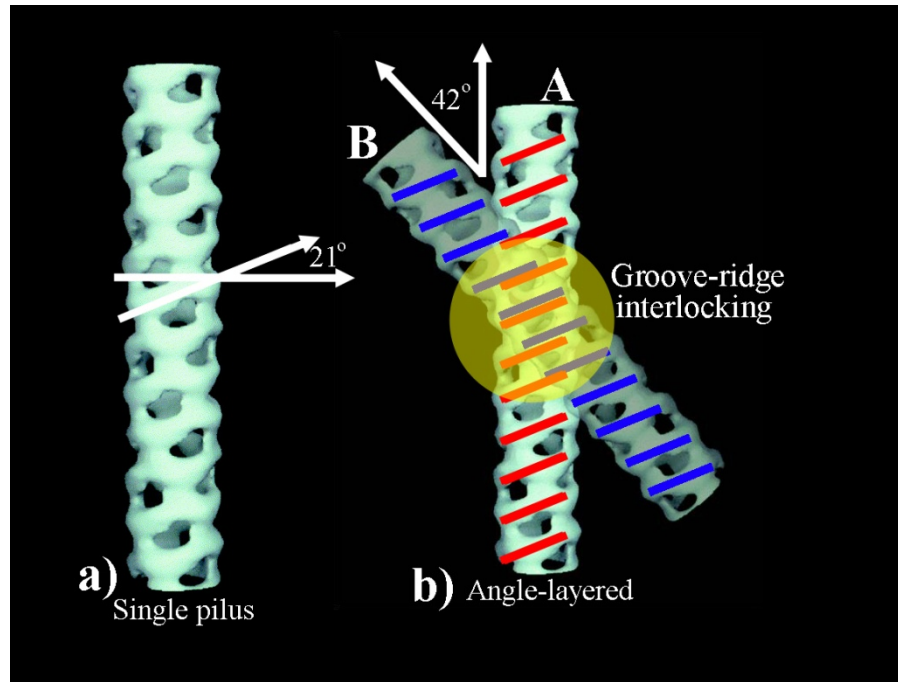


Figure 6.5 a) Single pilus with a set of alternating ridges and grooves with a pitch angle of 21° . b) When crossing angle between pili A and B is 42° , the ridges of pilus A can make a reasonable interlocking fit into corresponding grooves of pilus B. Images are modified from [79].

6.3. Conclusions

In summary, for the first time, we reproducibly generate colloidal crystals from rodlike pili particles and demonstrated their use as novel biotemplates for the synthesis of inorganic nanomaterials. The pili crystals were composed of multi-layers of pili with highly ordered hierarchical structures which were precisely controlled by the molecular recognition between neighboring pili layers. The pili bundles, double-layered lattices and multi-layered pili crystals are free-standing and stable, and could serve as templates for the organization and assembly of inorganic nanomaterials. The novel inorganic nanomaterials synthesized on these templates could find potential applications in photonics, nanomedicine and biosensing.

Chapter 7 Summary of Results and Future Directions

7.1. Summary of Results

In recent years, biological macromolecules have been exploited as the most promising templates for the development of novel nanostructures and nanomaterials. In the previous chapters, the use of spider silks, bacteriophage, and bacterial pili as biological templates for nanosynthesis or medical applications are discussed.

In Chapter 2, 4 and 5, we found spider silks and engineered bacteriophage are promising collagen fiber substitutes for the fabrication of bone regeneration scaffold. Both of them can interact with nano-scaled hydroxyapatite crystals and support the proliferation of resident bone cells.

Chapter 2 demonstrates that HAP crystals can be nucleated and grown on the natural spider dragline silks with a preferred orientation. The resultant biomineralized silk may serve as a building block that can be assembled into a larger material that has the potential for application as a bone implant and tissue engineering scaffold. This work also indicates that natural spider silk contains protein domains that can nucleate HAP and

the beta sheets in the silk protein can induce the oriented nucleation of HAP crystals. We believe that the oriented growth of HAP is a result of silk protein-mediated nucleation dominated by crystal plane matching, stereochemistry matching, and electrostatic interactions.

Chapter 4 describes an identification of HAP-binding phages by biopanning landscape phage libraries against HAP nanorods. The best HAP-binding phage, DSSTPSST-phage, can assemble with HAP nanorods into a novel scaffold by freeze-dry method. In the building blocks of the scaffold, HAP nanorods were aligned and packed by HAP-binding phages, mimicking the lowest level of hierarchy of nature bone. This scaffold assembled from HAP nanorods and HAP-binding phages could efficiently support and promote MSCs seeding and proliferation on it.

Chapter 5 demonstrates that phage films assembled from wild type or genetically engineered M13 phages can support MSC proliferation and differentiation. And the M13 phage films are also an ideal model for the study of tissue generation and cell differentiation niches. These films are ideal for the following reasons: 1) cells can grow on phage films; 2) the

phage film is able to induce contact guidance; 3) the surface topography is controllable by using different concentrations of phage; 4) the surface chemistry such as surface charges, can be programmed through genetic modifications; 5) introducing functional peptides like OGP into the substrate film is easy to achieve, providing a facile approach for studying cell differentiation niches. As for in vitro cell culturing, cellular morphology, proliferation and differentiation are the two main factors that affect are surface topography and surface chemistry. Both of them could be controlled in our genetically programmable phage substrate system.

Phage display-based biopanning process is a powerful tool for identifying target-binding peptides and studying protein-protein interactions. Hydroxyapatite-binding and microtubule-binding peptides are identified in Chapter 3 and 4 respectively by using landscape phage libraries. Microtubule-MAPs interactions were also studied in Chapter 3.

In Chapter 3, a biopanning of a landscape phage library against the purified tubulins was performed to study the interactions between MAPs and microtubules. RELIC was applied to align the affinity-selected

peptides identified in biopanning with the sequences of different MAPs and thus identify the microtubule-binding domains of these MAPs. Based on our data, some known microtubule-binding domains are confirmed and many new domains on the MAPs are identified, which can play important roles in the binding interaction between MAPs and microtubules.

Chapter 5 describes the generation of colloidal crystals from rodlike pili particles and demonstrates their use as novel biotemplates for the synthesis of inorganic nanomaterials. The pili crystals are composed of multi-layers of pili with highly ordered hierarchical structures which are precisely controlled by the molecular recognition between neighboring pili layers. The pili bundles, double-layered lattices and multi-layered pili crystals are free-standing and stable, and could serve as templates for the organization and assembly of inorganic nanomaterials.

7.2. Future Directions

7.2.1. Tissue Engineering Scaffold for Bone Regeneration

An ideal engineered bone scaffold should be biocompatible, mimicking natural bone structures, and highly porous. It has appropriate

surface chemistry for cellular attachment, differentiation, and proliferation, good mechanical properties, and controlled degradation. Hydroxyapatite is considered as the best bioceramic for its excellent biocompatibility and the ability to enhance cellular adhesion and proliferation. However, it lacks the osteoinductivity and chemical cues for bone cell differentiation. A biopolymer which can provide both osteoinductivity and chemical cues is needed to incorporate with hydroxyapatite to form a bioactive composite material. Spider silks and filamentous phages are chosen in my work as potential biopolymers because specific designed peptides can be genetically displayed on their surfaces. By this way, they can easily induce functional peptides into scaffolds which may provide needed osteoinductivity and chemical cues. Chapter 2 and 4 describe spider silks and phage can bind or nucleate hydroxyapatite to form bioactive composite material for cellular adhesion and proliferation. Chapter 5 shows foreign peptides can be induced into scaffold and effect the proliferation and differentiation of resident bone cells. Based on all these work, the following work could be performed: (1) displaying specific peptides which have osteoinductivity and chemical cues on the

phage/spider silk surfaces and allowing these engineered phage/spider silks assemble with hydroxyapatite nanorods into a bone scaffold. Bone cells can proliferate and differentiate on such scaffold and an animal test is also anticipated for bone regeneration. (2) The potential advantages of using phage as building blocks are the control of their surface chemistry via genetic modifications which may offer further promising opportunities for the study of tissue generation and cell differentiation niches. (3) Both spider silks and engineered phages can be used to assemble with hydroxyapatite crystals for scaffold generation. Such scaffold has both good mechanical properties and genetically tunable surfaces which may be more promising for being applied into practical applications.

7.2.2. Phage Display Technique for Protein-Protein Interaction

Studies.

Chapter 2 describes how to take advantage of phage display technique as a general method to study protein-protein interactions. Compared with other methods, it has many advantages: (1) Interacting proteins of the target are even not needed to study the interactions. For

new proteins, it is always a good way to predict their interacting proteins while other methods mentioned above can only passively confirm proposed interacting proteins. (2) The selected peptides can provide insight into the minimum composition requirements for binding to the targets. The size of phage-display-selected binding domains is much smaller than the results from traditional biological methods. (3) Phage display biopanning is not time-consuming and is cost-effective. The biopanning just needs several weeks of experiments and is supported by bioinformatics software such as RELIC. The selected peptides against one target can be used in the study of all target-interacting proteins. However, the identified binding sites based on this way are not experimentally confirmed. Follow-up experiments are needed to study such interactions. Therefore, a reasonable way for studying protein-protein interactions is to use the potential binding sites identified from biopanning process to narrow the target binding domains and direct practical experiments.

7.2.3. Microtubule-Binding Phages as an Anti-Cancer Drug.

The microtubule-binding phages identified in Chapter 2 can interact with free tubulins just like tau proteins. This interaction can interfere with the regular assembly of microtubules *in vitro*. As we know, a lot of microtubule binding molecules can be treated as anti-cancer drugs to kill cancer cells by disturbing the regular functions of microtubules in cellular mitosis. It is also very possible that our identified tubulin-binding phage can be introduced into cancer cells as a drug to interfere with the microtubule assembly *in vivo*. Moreover, double or triple display of different peptides on a single phage fiber can also be achieved so that microtubule-binding peptides and cancer cell targeting peptides can be displayed simultaneously on a single phage. Such phages may specifically enter into cancer cells and kill them by disturbing the regular functions of microtubules. They are expected to be more powerful than traditional anti-cancer drugs which will kill both healthy and cancer cells.

7.2.4. Pili Colloidal Crystals for the Fabrication of Photonic Crystals.

Photonic crystals are artificial structures with a periodically varying refractive index. The scale of periodicity in the refractive index determines the frequency of the electromagnetic waves that can be manipulated. Colloidal crystals are a branch of artificial photonic crystals. However, the fabrication of three-dimensional photonic crystals at x-ray wavelengths is extremely difficult because of the small sizes involved. Only naturally occurring structures and biological organisms can provide a scaffold for realization of three-dimensional crystals with very small dimensions. The synthesized pili colloidal crystals (Chapter 6) have highly ordered structures and nano-sized periodicity. If we bury the pili crystals into another material such as silica and calcinate pili fibers under a high temperature, the remaining silica-air structure will have a periodically varying refractive index which may lead to a novel photonic crystal.

Bibliography of References

1. Daniel, M.C. and D. Astruc, *Gold nanoparticles: Assembly, supramolecular chemistry, quantum-size-related properties, and applications toward biology, catalysis, and nanotechnology*. Chemical Reviews, 2004. **104**(1): p. 293-346.
2. Sargent, E.H., *Infrared quantum dots*. Advanced Materials, 2005. **17**(5): p. 515-522.
3. Tasis, D., et al., *Chemistry of carbon nanotubes*. Chemical Reviews, 2006. **106**(3): p. 1105-1136.
4. Lu, A.H., E.L. Salabas, and F. Schuth, *Magnetic nanoparticles: Synthesis, protection, functionalization, and application*. Angewandte Chemie-International Edition, 2007. **46**(8): p. 1222-1244.
5. Liang, W.J., et al., *Kondo resonance in a single-molecule transistor*. Nature, 2002. **417**(6890): p. 725-729.
6. Klein, D.L., et al., *A single-electron transistor made from a cadmium selenide nanocrystal*. Nature, 1997. **389**(6652): p. 699-701.
7. Huang, Y., et al., *Logic gates and computation from assembled nanowire building blocks*. Science, 2001. **294**(5545): p. 1313-1317.
8. Lazzari, M. and M.A. Lopez-Quintela, *Block copolymers as a tool for nanomaterial fabrication*. Advanced Materials, 2003. **15**(19): p. 1583-1594.
9. Varghese, R. and H.A. Wagenknecht, *DNA as a supramolecular framework for the helical arrangements of chromophores: towards*

photoactive DNA-based nanomaterials. Chemical Communications, 2009(19): p. 2615-2624.

10. Merzlyak, A. and S.W. Lee, *Phage as templates for hybrid materials and mediators for nanomaterial synthesis*. Current Opinion in Chemical Biology, 2006. **10**(3): p. 246-252.
11. Tang, S., et al., *Protein-mediated nanocrystal assembly for flash memory fabrication*. Ieee Transactions on Electron Devices, 2007. **54**(3): p. 433-438.
12. Belcher, A.M., et al., *Virus-based genetic toolkit for the directed synthesis of magnetic and semiconducting nanowires*. Abstracts of Papers of the American Chemical Society, 2004. **228**: p. U542-U542.
13. Mao, C.B., et al., *Virus-based toolkit for the directed synthesis of magnetic and semiconducting nanowires*. Science, 2004. **303**(5655): p. 213-217.
14. Mao, C.B., et al., *Viral assembly of oriented quantum dot nanowires*. Proceedings of the National Academy of Sciences of the United States of America, 2003. **100**(12): p. 6946-6951.
15. Sharma, J., et al., *Control of Self-Assembly of DNA Tubules Through Integration of Gold Nanoparticles*. Science, 2009. **323**(5910): p. 112-116.
16. Cao, B. and C. Mao, *Oriented Nucleation of Hydroxylapatite Crystals on Spider Dragline Silks*. Langmuir, 2007.
17. Lin, C.X., et al., *Mirror Image DNA Nanostructures for Chiral Supramolecular Assemblies*. Nano Letters, 2009. **9**(1): p. 433-436.

18. Lee, Y.J., et al., *Fabricating Genetically Engineered High-Power Lithium-Ion Batteries Using Multiple Virus Genes*. *Science*, 2009. **324**(5930): p. 1051-1055.
19. Liu, A.H., G. Abbineni, and C.B. Moo, *Nanocomposite Films Assembled from Genetically Engineered Filamentous Viruses and Gold Nanoparticles: Nanoarchitecture- and Humidity-Tunable Surface Plasmon Resonance Spectra*. *Advanced Materials*, 2009. **21**(9): p. 1001-+.
20. Scheibel, T., *Spider silks: recombinant synthesis, assembly, spinning, and engineering of synthetic proteins*. *Microb Cell Fact*, 2004. **3**(1): p. 14.
21. Kluge, J.A., et al., *Spider silks and their applications*. *Trends in Biotechnology*, 2008. **26**(5): p. 244-251.
22. Riekkel, C., et al., *Aspects of X-ray diffraction on single spider fibers*. *Int J Biol Macromol*, 1999. **24**(2-3): p. 179-86.
23. Wang, Y.Z., et al., *Cartilage tissue engineering with silk scaffolds and human articular chondrocytes*. *Biomaterials*, 2006. **27**(25): p. 4434-4442.
24. Hakimi, O., et al., *Modulation of cell growth on exposure to silkworm and spider silk fibers*. *Journal of Biomedical Materials Research Part A*, 2010. **92A**(4): p. 1366-1372.
25. Mayes, E.L., F. Vollrath, and S. Mann, *Fabrication of magnetic spider silk and other silk-fiber composites using inorganic nanoparticles*. *Advanced Materials*, 1998. **10**(10): p. 801-805.
26. Lazaris, A., et al., *Spider silk fibers spun from soluble recombinant silk produced in mammalian cells*. *Science*, 2002. **295**(5554): p. 472-476.

27. Whaley, S.R., et al., *Selection of peptides with semiconductor binding specificity for directed nanocrystal assembly*. Nature, 2000. **405**(6787): p. 665-668.
28. Lee, S.W., et al., *Ordering of quantum dots using genetically engineered viruses*. Science, 2002. **296**(5569): p. 892-895.
29. Lee, S.W., S.K. Lee, and A.M. Belcher, *Virus-based alignment of inorganic, organic, and biological nanosized materials*. Advanced Materials, 2003. **15**(9): p. 689-692.
30. Mao, C.B., J.F. Qi, and A.M. Belcher, *Building quantum dots into solids with well-defined shapes*. Advanced Functional Materials, 2003. **13**(8): p. 648-656.
31. Flynn, C.E., et al., *Synthesis and organization of nanoscale II-VI semiconductor materials using evolved peptide specificity and viral capsid assembly*. Journal of Materials Chemistry, 2003. **13**(10): p. 2414-2421.
32. Flynn, C.E., et al., *Viruses as vehicles for growth, organization and assembly of materials*. Acta Materialia, 2003. **51**(19): p. 5867-5880.
33. Nam, K.T., et al., *Genetically driven assembly of nanorings based on the M13 virus*. Nano Letters, 2004. **4**(1): p. 23-27.
34. Ni, J.P., et al., *Molecular orientation of a ZnS-nanocrystal-modified M13 virus on a silicon substrate*. Journal of Polymer Science Part B-Polymer Physics, 2004. **42**(4): p. 629-635.
35. Jaffar, S., et al., *Layer-by-layer surface modification and patterned electrostatic deposition of quantum dots*. Nano Letters, 2004. **4**(8): p. 1421-1425.

36. Sweeney, R.Y., et al., *Bacterial biosynthesis of cadmium sulfide nanocrystals*. *Chemistry & Biology*, 2004. **11**(11): p. 1553-1559.
37. Huang, Y., et al., *Programmable assembly of nanoarchitectures using genetically engineered viruses*. *Nano Letters*, 2005. **5**(7): p. 1429-1434.
38. Lee, S.K., D.S. Yun, and A.M. Belcher, *Cobalt ion mediated self-assembly of genetically engineered bacteriophage for biomimetic Co-Pt hybrid material*. *Biomacromolecules*, 2006. **7**(1): p. 14-17.
39. Bhaviripudi, S., et al., *Synthesis, characterization, and optical properties of ordered arrays of III-nitride nanocrystals*. *Nano Letters*, 2007. **7**(11): p. 3512-3517.
40. Nam, K.T., et al., *Stamped microbattery electrodes based on self-assembled M13 viruses*. *Proceedings of the National Academy of Sciences of the United States of America*, 2008. **105**(45): p. 17227-17231.
41. Nam, K.T., *Virus-enabled synthesis and assembly of nanowires for lithium ion battery electrodes (vol 312, pg 885, 2006)*. *Science*, 2008. **322**(5898): p. 44-44.
42. Nam, K.T., et al., *Virus-enabled synthesis and assembly of nanowires for lithium ion battery electrodes*. *Science*, 2006. **312**(5775): p. 885-888.
43. Souza, G.R., et al., *Networks of gold nanoparticles and bacteriophage as biological sensors and cell-targeting agents*. *Proceedings of the National Academy of Sciences of the United States of America*, 2006. **103**(5): p. 1215-1220.
44. Smith, G.P. and V.A. Petrenko, *Phage display*. *Chemical Reviews*, 1997. **97**(2): p. 391-410.

45. Petrenko, V.A. and V.J. Vodyanoy, *Phage display for detection of biological threat agents*. Journal of Microbiological Methods, 2003. **53**(2): p. 253-262.
46. Stubbs, J.T., et al., *Characterization of native and recombinant bone sialoprotein: Delineation of the mineral-binding and cell adhesion domains and structural analysis of the RGD domain*. Journal of Bone and Mineral Research, 1997. **12**(8): p. 1210-1222.
47. Sawyer, A.A., et al., *The effect of the addition of a polyglutamate motif to RGD on peptide tethering to hydroxyapatite and the promotion of mesenchymal stem cell adhesion*. Biomaterials, 2005. **26**(34): p. 7046-7056.
48. Dogic, Z. and S. Fraden, *Ordered phases of filamentous viruses*. Current Opinion in Colloid & Interface Science, 2006. **11**(1): p. 47-55.
49. Lee, S.W., B.M. Wood, and A.M. Belcher, *Chiral smectic C structures of virus-based films*. Langmuir, 2003. **19**(5): p. 1592-1598.
50. Tang, J.X. and S. Fraden, *Isotropic-Cholesteric Phase-Transition in Colloidal Suspensions of Filamentous Bacteriophage-Fd*. Liquid Crystals, 1995. **19**(4): p. 459-467.
51. Dogic, Z. and S. Fraden, *Cholesteric phase in virus suspensions*. Langmuir, 2000. **16**(20): p. 7820-7824.
52. Kehoe, J.W. and B.K. Kay, *Filamentous phage display in the new millennium*. Chemical Reviews, 2005. **105**(11): p. 4056-4072.
53. Petrenko, V.A., et al., *A library of organic landscapes on filamentous phage*. Protein Engineering, 1996. **9**(9): p. 797-801.

54. Estephan, E., et al., *Tailoring GaN semiconductor surfaces with biomolecules*. Journal of Physical Chemistry B, 2008. **112**(29): p. 8799-8805.
55. Naik, R.R., et al., *Biomimetic synthesis and patterning of silver nanoparticles*. Nat Mater, 2002. **1**(3): p. 169-72.
56. Naik, R.R., et al., *Peptide templates for nanoparticle synthesis derived from polymerase chain reaction-driven phage display*. Advanced Functional Materials, 2004. **14**(1): p. 25-30.
57. Seker, U.O.S., et al., *Adsorption behavior of linear and cyclic genetically engineered platinum binding peptides*. Langmuir, 2007. **23**(15): p. 7895-7900.
58. Sarikaya, M., et al., *Molecular biomimetics: nanotechnology through biology*. Nature Materials, 2003. **2**(9): p. 577-585.
59. Sano, K.I. and K. Shiba, *A hexapeptide motif that electrostatically binds to the surface of titanium*. Journal of the American Chemical Society, 2003. **125**(47): p. 14234-14235.
60. Li, Y.J., G.P. Whyburn, and Y. Huang, *Specific Peptide Regulated Synthesis of Ultrasmall Platinum Nanocrystals*. Journal of the American Chemical Society, 2009. **131**(44): p. 15998-+.
61. Naik, R.R., et al., *Silica-precipitating peptides isolated from a combinatorial phage display peptide library*. Journal of Nanoscience and Nanotechnology, 2002. **2**(1): p. 95-100.
62. Oren, E.E., et al., *A novel knowledge-based approach to design inorganic-binding peptides*. Bioinformatics, 2007. **23**(21): p. 2816-2822.

63. Gaskin, D.J.H., K. Starck, and E.N. Vulfson, *Identification of inorganic crystal-specific sequences using phage display combinatorial library of short peptides: A feasibility study*. Biotechnology Letters, 2000. **22**(15): p. 1211-1216.
64. Li, C.M., G.D. Botsaris, and D.L. Kaplan, *Selective in vitro effect of peptides on calcium carbonate crystallization*. Crystal Growth & Design, 2002. **2**(5): p. 387-393.
65. Dickerson, M.B., et al., *Identification and design of peptides for the rapid, high-yield formation of nanoparticulate TiO₂ from aqueous solutions at room temperature*. Chemistry of Materials, 2008. **20**(4): p. 1578-1584.
66. Umetsu, M., et al., *Bioassisted room-temperature immobilization and mineralization of zinc oxide - The structural ordering of ZnO nanoparticles into a flower-type morphology*. Advanced Materials, 2005. **17**(21): p. 2571-+.
67. Reiss, B.D., et al., *Biological routes to metal alloy ferromagnetic nanostructures*. Nano Letters, 2004. **4**(6): p. 1127-1132.
68. Ahmad, G., et al., *Rapid bioenabled formation of ferroelectric BaTiO₃ at room temperature from an aqueous salt solution at near neutral pH*. Journal of the American Chemical Society, 2008. **130**(1): p. 4-+.
69. Ahmad, G., et al., *Rapid, room-temperature formation of crystalline calcium molybdate phosphor microparticles via peptide-induced precipitation*. Advanced Materials, 2006. **18**(13): p. 1759-+.
70. Klem, M.T., et al., *Bio-inspired synthesis of protein-encapsulated CoPt nanoparticles*. Advanced Functional Materials, 2005. **15**(9): p. 1489-1494.

71. Roy, M.D., et al., *Identification of a highly specific hydroxyapatite-binding peptide using phage display*. *Advanced Materials*, 2008. **20**(10): p. 1830-+.
72. Gungormus, M., et al., *Regulation of in vitro calcium phosphate mineralization by combinatorially selected hydroxyapatite-binding peptides*. *Biomacromolecules*, 2008. **9**(3): p. 966-973.
73. Segvich, S.J., H.C. Smith, and D.H. Kohn, *The adsorption of preferential binding peptides to apatite-based materials*. *Biomaterials*, 2009. **30**(7): p. 1287-1298.
74. Dickerson, M.B., et al., *Identification of peptides that promote the rapid precipitation of germania nanoparticle networks via use of a peptide display library*. *Chemical Communications*, 2004(15): p. 1776-1777.
75. Wang, S.Q., et al., *Peptides with selective affinity for carbon nanotubes*. *Nature Materials*, 2003. **2**(3): p. 196-200.
76. Kase, D., et al., *Affinity selection of peptide phage libraries against single-wall carbon nanohorns identifies a peptide aptamer with conformational variability*. *Langmuir*, 2004. **20**(20): p. 8939-8941.
77. Morita, Y., et al., *A screening of phage displayed peptides for the recognition of fullerene (C60)*. *Journal of Molecular Catalysis B-Enzymatic*, 2004. **28**(4-6): p. 185-190.
78. Capitani, G., et al., *Structural and functional insights into the assembly of type 1 pili from Escherichia coli*. *Microbes and Infection*, 2006. **8**(8): p. 2284-2290.
79. Hahn, E., et al., *Exploring the 3D molecular architecture of Escherichia coli type 1 pili*. *Journal of Molecular Biology*, 2002. **323**(5): p. 845-857.

80. Nishiyama, M., et al., *Identification and characterization of the chaperone-subunit complex-binding domain from the type 1 pilus assembly platform FimD*. *Journal of Molecular Biology*, 2003. **330**(3): p. 513-525.
81. Choudhury, D., et al., *X-ray structure of the FimC-FimH chaperone-adhesin complex from uropathogenic Escherichia coli*. *Science*, 1999. **285**(5430): p. 1061-1066.
82. Klemm, P. and M.A. Schembri, *Fimbrial surface display systems in bacteria: from vaccines to random libraries*. *Microbiology-Uk*, 2000. **146**: p. 3025-3032.
83. Klemm, P., *The Fima Gene Encoding the Type-1 Fimbrial Subunit of Escherichia-Coli - Nucleotide-Sequence and Primary Structure of the Protein*. *European Journal of Biochemistry*, 1984. **143**(2): p. 395-399.
84. Schilling, J.D., M.A. Mulvey, and S.J. Hultgren, *Structure and function of Escherichia coli type 1 pili: New insight into the pathogenesis of urinary tract infections*. *Journal of Infectious Diseases*, 2001. **183**: p. S36-S40.
85. Lee, S.W., A.W. Way, and E.G. Osen, *Purification and Subunit Heterogeneity of Pili of Bordetella-Bronchiseptica*. *Infection and Immunity*, 1986. **51**(2): p. 586-593.
86. Blom, J., G.A. Hansen, and F.M. Poulsen, *Morphology of Cells and Hemagglutinogens of Bordetella Species - Resolution of Substructural Units in Fimbriae of Bordetella-Pertussis*. *Infection and Immunity*, 1983. **42**(1): p. 308-317.
87. Brinton, C.C., *Structure Function Synthesis and Genetic Control of Bacterial Pili and a Molecular Model for DNA and Rna Transport in Gram Negative Bacteria*. *Transactions of the New York Academy of Sciences*, 1965. **27**(8): p. 1003-&.

88. Steven, A.C., et al., *Helical Structure of Bordetella-Pertussis Fimbriae*. Journal of Bacteriology, 1986. **167**(3): p. 968-974.
89. Murugan, R. and S. Ramakrishna, *Nanoengineered biomimetic bone-building blocks*. Molecular Building Blocks for Nanotechnology: From Diamondoids to Nanoscale Materials and Applications, 2007. **109**: p. 301-352.
90. Burg, K.J.L., S. Porter, and J.F. Kellam, *Biomaterial developments for bone tissue engineering*. Biomaterials, 2000. **21**(23): p. 2347-2359.
91. Rice, M.A., et al., *Cell-based therapies and tissue engineering*. Otolaryngologic Clinics of North America, 2005. **38**(2): p. 199-+.
92. Liu, X.H. and P.X. Ma, *Polymeric scaffolds for bone tissue engineering*. Annals of Biomedical Engineering, 2004. **32**(3): p. 477-486.
93. Meinel, L., et al., *Silk implants for the healing of critical size bone defects*. Bone, 2005. **37**(5): p. 688-698.
94. Huang, L.H., et al., *Synthesis and characterization of electroactive and biodegradable ABA block copolymer of polylactide and aniline pentamer*. Biomaterials, 2007. **28**(10): p. 1741-1751.
95. Ma, P.X., *Biomimetic materials for tissue engineering*. Advanced Drug Delivery Reviews, 2008. **60**(2): p. 184-198.
96. Stevens, B., et al., *A review of materials, fabrication to enhance bone regeneration in methods, and strategies used engineered bone tissues*. Journal of Biomedical Materials Research Part B-Applied Biomaterials, 2008. **85B**(2): p. 573-582.

97. Hench, L.L., *Bioceramics - from Concept to Clinic*. Journal of the American Ceramic Society, 1991. **74**(7): p. 1487-1510.
98. Taton, T.A., *Nanotechnology - Boning up on biology*. Nature, 2001. **412**(6846): p. 491-492.
99. Addadi, L., et al., *Mollusk shell formation: A source of new concepts for understanding biomineralization processes*. Chemistry-a European Journal, 2006. **12**(4): p. 981-987.
100. Akasaka, T., et al., *Apatite formation on carbon nanotubes*. Materials Science & Engineering C-Biomimetic and Supramolecular Systems, 2006. **26**(4): p. 675-678.
101. Mann, S., *Molecular Recognition in Biomineralization*. Nature, 1988. **332**(6160): p. 119-124.
102. Mao, C.B., et al., *Oriented growth of phosphates on polycrystalline titanium in a process mimicking biomineralization*. Journal of Crystal Growth, 1999. **206**(4): p. 308-321.
103. Mao, C.B., et al., *Oriented growth of hydroxyapatite on (0001) textured titanium with functionalized self-assembled silane monolayer as template*. Journal of Materials Chemistry, 1998. **8**(12): p. 2795-2801.
104. Mao, C.B., et al., *The functionalization of titanium with EDTA to induce biomimetic mineralization of hydroxyapatite*. Journal of Materials Chemistry, 1999. **9**(10): p. 2573-2582.
105. Shaw, W.J., et al., *Determination of statherin N-terminal peptide conformation on hydroxyapatite crystals*. Journal of the American Chemical Society, 2000. **122**(8): p. 1709-1716.

106. DeOliveira, D.B. and R.A. Laursen, *Control of calcite crystal morphology by a peptide designed to bind to a specific surface*. Journal of the American Chemical Society, 1997. **119**(44): p. 10627-10631.
107. Hartgerink, J.D., E. Beniash, and S.I. Stupp, *Self-assembly and mineralization of peptide-amphiphile nanofibers*. Science, 2001. **294**(5547): p. 1684-1688.
108. Weiner, S. and H.D. Wagner, *The material bone: Structure mechanical function relations*. Annual Review of Materials Science, 1998. **28**: p. 271-298.
109. Roveri, N., et al., *Biologically inspired growth of hydroxyapatite nanocrystals inside self-assembled collagen fibers*. Materials Science & Engineering C-Biomimetic and Supramolecular Systems, 2003. **23**(3): p. 441-446.
110. Xu, M. and R.V. Lewis, *Structure of a Protein Superfiber - Spider Dragline Silk*. Proceedings of the National Academy of Sciences of the United States of America, 1990. **87**(18): p. 7120-7124.
111. Meinel, L., et al., *Engineering bone-like tissue in vitro using human bone marrow stem cells and silk scaffolds*. Journal of Biomedical Materials Research Part A, 2004. **71A**(1): p. 25-34.
112. Kino, R., et al., *Deposition of bone-like apatite on modified silk fibroin films from simulated body fluid*. Journal of Applied Polymer Science, 2006. **99**(5): p. 2822-2830.
113. Gatesy, J., et al., *Extreme diversity, conservation, and convergence of spider silk fibroin sequences*. Science, 2001. **291**(5513): p. 2603-2605.

114. Hinman, M.B., J.A. Jones, and R.V. Lewis, *Synthetic spider silk: a modular fiber*. Trends in Biotechnology, 2000. **18**(9): p. 374-379.
115. Simmons, A.H., C.A. Michal, and L.W. Jelinski, *Molecular orientation and two-component nature of the crystalline fraction of spider dragline silk*. Science, 1996. **271**(5245): p. 84-87.
116. Falini, G., et al., *Oriented crystallization of vaterite in collagenous matrices*. Chemistry-a European Journal, 1998. **4**(6): p. 1048-1052.
117. He, G., et al., *Nucleation of apatite crystals in vitro by self-assembled dentin matrix protein, 1*. Nature Materials, 2003. **2**(8): p. 552-558.
118. Thiel, B.L., D.D. Kunkel, and C. Viney, *Physical and Chemical Microstructure of Spider Dragline - a Study by Analytical Transmission Electron-Microscopy*. Biopolymers, 1994. **34**(8): p. 1089-1097.
119. Silverstone, L.M., et al., *Remineralization of Natural and Artificial Lesions in Human Dental Enamel In vitro - Effect of Calcium-Concentration of the Calcifying Fluid*. Caries Research, 1981. **15**(2): p. 138-&.
120. van Beek, J.D., et al., *The molecular structure of spider dragline silk: Folding and orientation of the protein backbone*. Proceedings of the National Academy of Sciences of the United States of America, 2002. **99**(16): p. 10266-10271.
121. Posner, A.S., J.M. Stutman, and E.R. Lippincott, *Hydrogen-Bonding in Calcium-Deficient Hydroxyapatites*. Nature, 1960. **188**(4749): p. 486-487.
122. Scatena, L.F., M.G. Brown, and G.L. Richmond, *Water at hydrophobic surfaces: Weak hydrogen bonding and strong orientation effects*. Science, 2001. **292**(5518): p. 908-912.

123. Newton, M.D., *Theoretical Aspects of the Oh...O Hydrogen-Bond and Its Role in Structural and Kinetic Phenomena*. Acta Crystallographica Section B-Structural Science, 1983. **39**(Feb): p. 104-113.
124. Mandelkow, E.M. and E. Mandelkow, *Tau in Alzheimer's disease*. Trends Cell Biol, 1998. **8**(11): p. 425-7.
125. Amos, L.A., *Microtubule structure and its stabilisation*. Org Biomol Chem, 2004. **2**(15): p. 2153-60.
126. Nogales, E., *Structural insights into microtubule function*. Annu Rev Biochem, 2000. **69**: p. 277-302.
127. Nogales, E., et al., *High-resolution model of the microtubule*. Cell, 1999. **96**(1): p. 79-88.
128. Nogales, E., S.G. Wolf, and K.H. Downing, *Structure of the alpha beta tubulin dimer by electron crystallography*. Nature, 1998. **391**(6663): p. 199-203.
129. Wang, H.W. and E. Nogales, *Nucleotide-dependent bending flexibility of tubulin regulates microtubule assembly*. Nature, 2005. **435**(7044): p. 911-5.
130. Sillen, A., et al., *NMR investigation of the interaction between the neuronal protein Tau and the microtubules*. Biochemistry, 2007. **46**(11): p. 3055-3064.
131. Avila, J., et al., *Role of tau protein in both physiological and pathological conditions*. Physiological Reviews, 2004. **84**(2): p. 361-384.

132. Makrides, V., et al., *Evidence for two distinct binding sites for tau on microtubules*. Proceedings of the National Academy of Sciences of the United States of America, 2004. **101**(17): p. 6746-6751.
133. Ross, J.L., et al., *Tau induces cooperative Taxol binding to microtubules*. Proceedings of the National Academy of Sciences of the United States of America, 2004. **101**(35): p. 12910-12915.
134. Kar, S., et al., *Repeat motifs of tau bind to the insides of microtubules in the absence of taxol*. Embo Journal, 2003. **22**(1): p. 70-77.
135. Santarella, R.A., et al., *Surface-decoration of microtubules by human Tau*. Journal of Molecular Biology, 2004. **339**(3): p. 539-553.
136. Al-Bassam, J., et al., *MAP2 and tau bind longitudinally along the outer ridges of microtubule protofilaments*. Journal of Cell Biology, 2002. **157**(7): p. 1187-1196.
137. Samsonov, A., et al., *Tau interaction with microtubules in vivo*. J Cell Sci, 2004. **117**(Pt 25): p. 6129-41.
138. Dehmelt, L. and S. Halpain, *The MAP2/Tau family of microtubule-associated proteins*. Genome Biology, 2005. **6**(1): p. -.
139. Halpain, S. and L. Dehmelt, *The MAP1 family of microtubule-associated proteins*. Genome Biol, 2006. **7**(6): p. 224.
140. Orban-Nemeth, Z., et al., *Microtubule-associated protein 1S, a short and ubiquitously expressed member of the microtubule-associated protein 1 family*. Journal of Biological Chemistry, 2005. **280**(3): p. 2257-2265.

141. Hammarback, J.A., et al., *Map1b Is Encoded as a Polyprotein That Is Processed to Form a Complex N-Terminal Microtubule-Binding Domain*. *Neuron*, 1991. **7**(1): p. 129-139.
142. Mann, S.S. and J.A. Hammarback, *Molecular characterization of light chain 3. A microtubule binding subunit of MAP1A and MAP1B*. *J Biol Chem*, 1994. **269**(15): p. 11492-7.
143. Noiges, R., et al., *Microtubule-associated protein 1A (MAP1A) and MAP1B: light chains determine distinct functional properties*. *J Neurosci*, 2002. **22**(6): p. 2106-14.
144. Vaillant, A.R., et al., *Characterization of the microtubule-binding domain of microtubule-associated protein 1A and its effects on microtubule dynamics*. *J Biol Chem*, 1998. **273**(22): p. 13973-81.
145. Cravchik, A., D. Reddy, and A. Matus, *Identification of a novel microtubule-binding domain in microtubule-associated protein 1A (MAP1A)*. *J Cell Sci*, 1994. **107 (Pt 3)**: p. 661-72.
146. Noble, M., S.A. Lewis, and N.J. Cowan, *The microtubule binding domain of microtubule-associated protein MAP1B contains a repeated sequence motif unrelated to that of MAP2 and tau*. *J Cell Biol*, 1989. **109**(6 Pt 2): p. 3367-76.
147. Aizawa, H., et al., *A common amino acid sequence in 190-kDa microtubule-associated protein and tau for the promotion of microtubule assembly*. *J Biol Chem*, 1989. **264**(10): p. 5885-90.
148. Lewis, S.A., D.H. Wang, and N.J. Cowan, *Microtubule-associated protein MAP2 shares a microtubule binding motif with tau protein*. *Science*, 1988. **242**(4880): p. 936-9.

149. Carter, D.M., et al., *Phage display reveals multiple contact sites between FhuA, an outer membrane receptor of Escherichia coli, and TonB*. Journal of Molecular Biology, 2006. **357**(1): p. 236-251.
150. Rodi, D.J., L. Makowski, and B.K. Kay, *One from column A and two from column B: the benefits of phage display in molecular-recognition studies*. Current Opinion in Chemical Biology, 2002. **6**(1): p. 92-96.
151. Brigati, J., et al., *Diagnostic probes for Bacillus anthracis spores selected from a landscape phage library*. Clinical Chemistry, 2004. **50**(10): p. 1899-1906.
152. Petrenko, V.A. and G.P. Smith, *Phages from landscape libraries as substitute antibodies*. Protein Engineering, 2000. **13**(8): p. 589-592.
153. Mandava, S., et al., *RELIC - A bioinformatics server for combinatorial peptide analysis and identification of protein-ligand interaction sites*. Proteomics, 2004. **4**(5): p. 1439-1460.
154. Makowski, L. and A. Soares, *Estimating the diversity of peptide populations from limited sequence data*. Bioinformatics, 2003. **19**(4): p. 483-489.
155. Rodi, D.J., A.S. Soares, and L. Makowski, *Quantitative assessment of peptide sequence diversity in M13 combinatorial peptide phage display libraries*. Journal of Molecular Biology, 2002. **322**(5): p. 1039-1052.
156. Zucconi, A., et al., *Selection of ligands by panning of domain libraries displayed on phage lambda reveals new potential partners of synaptotjanin 1*. Journal of Molecular Biology, 2001. **307**(5): p. 1329-1339.
157. Iannolo, G., et al., *Construction, exploitation and evolution of a new peptide library displayed at high density by fusion to the major coat*

- protein of filamentous phage*. Biological Chemistry, 1997. **378**(6): p. 517-521.
158. Zauner, W., et al., *Identification of two distinct microtubule binding domains on recombinant rat MAP 1B*. Eur J Cell Biol, 1992. **57**(1): p. 66-74.
159. Mukrasch, M.D., et al., *The "jaws" of the Tau-microtubule interaction*. Journal of Biological Chemistry, 2007. **282**(16): p. 12230-12239.
160. Goode, B.L., et al., *Functional interactions between the proline-rich and repeat regions of tau enhance microtubule binding and assembly*. Molecular Biology of the Cell, 1997. **8**(2): p. 353-65.
161. Butner, K.A. and M.W. Kirschner, *Tau-Protein Binds to Microtubules through a Flexible Array of Distributed Weak Sites*. Journal of Cell Biology, 1991. **115**(3): p. 717-730.
162. Goode, B.L. and S.C. Feinstein, *Identification of a Novel Microtubule-Binding and Assembly Domain in the Developmentally-Regulated Inter-Repeat Region of Tau*. Journal of Cell Biology, 1994. **124**(5): p. 769-782.
163. Hammarback, J.A., et al., *MAP1B is encoded as a polyprotein that is processed to form a complex N-terminal microtubule-binding domain*. Neuron, 1991. **7**(1): p. 129-39.
164. Riederer, B.M., *Microtubule-associated protein 1B, a growth-associated and phosphorylated scaffold protein*. Brain Res Bull, 2007. **71**(6): p. 541-58.
165. Bondallaz, P., et al., *The control of microtubule stability in vitro and in transfected cells by MAP1B and SCG10*. Cell Motil Cytoskeleton, 2006. **63**(11): p. 681-95.

166. West, R.R., K.M. Tenbarger, and J.B. Olmsted, *A Model for Microtubule-Associated Protein-4 Structure - Domains Defined by Comparisons of Human, Mouse, and Bovine Sequences*. Journal of Biological Chemistry, 1991. **266**(32): p. 21886-21896.
167. Aizawa, H., et al., *Functional Analyses of the Domain-Structure of Microtubule-Associated Protein-4 (Map-U)*. Journal of Biological Chemistry, 1991. **266**(15): p. 9841-9846.
168. Ferralli, J., T. Doll, and A. Matus, *Sequence-Analysis of Map2 Function in Living Cells*. Journal of Cell Science, 1994. **107**: p. 3115-3125.
169. Tokuraku, K., et al., *Microtubule-binding property of microtubule-associated protein 2 differs from that of microtubule-associated protein 4 and tau*. European Journal of Biochemistry, 1999. **264**(3): p. 996-1001.
170. Coffey, R.L., et al., *Exploring the Microtubule-Binding Region of Bovine Microtubule-Associated Protein-2 (Map-2) - Cdna Sequencing, Bacterial Expression, and Site-Directed Mutagenesis*. Biochemistry, 1994. **33**(45): p. 13199-13207.
171. Coffey, R.L. and D.L. Purich, *Noncooperative Binding of the Map-2 Microtubule-Binding Region to Microtubules*. Journal of Biological Chemistry, 1995. **270**(3): p. 1035-1040.
172. Sidhu, S.S. and F.A. Fellouse, *Synthetic therapeutic antibodies*. Nature Chemical Biology, 2006. **2**(12): p. 682-688.
173. Smith, G.P. and V.A. Petrenko, *Phage display [Review]*. Chem Rev. 1997. **97**: p. 391-410.

174. Sato, M. and T.J. Webster, *Nanobiotechnology: implications for the future of nanotechnology in orthopedic applications*. Expert Review of Medical Devices, 2004. **1**(1): p. 105-114.
175. Petrenko, V.A., et al., *A library of organic landscapes on filamentous phage*. Protein Eng., 1996. **9**: p. 797-801.
176. Smith, G.P. and V.A. Petrenko, *Phage Display*. Chem Rev, 1997. **97**(2): p. 391-410.
177. Kehoe, J.W. and B.K. Kay, *Filamentous phage display in the new millennium*. Chem Rev, 2005. **105**(11): p. 4056-72.
178. Smith, G.P., *Filamentous Fusion Phage - Novel Expression Vectors That Display Cloned Antigens on the Virion Surface*. Science, 1985. **228**(4705): p. 1315-1317.
179. Cao, B.R. and C.B. Mao, *Identification of Microtubule-Binding Domains on Microtubule-Associated Proteins by Major Coat Phage Display Technique*. Biomacromolecules, 2009. **10**(3): p. 555-564.
180. Petrenko, V.A. and V.J. Vodyanoy, *Phage display for detection of biological threat agents*. J Microbiol Methods, 2003. **53**(2): p. 253-62.
181. Petrenko, V.A. and G.P. Smith, *Phages from landscape libraries as substitute antibodies*. Protein Eng, 2000. **13**(8): p. 589-92.
182. Brigati, J.R. and V.A. Petrenko, *Thermostability of landscape phage probes*. Anal Bioanal Chem, 2005. **382**(6): p. 1346-50.
183. Youn, J., et al., *Identification and Characterization of Phenotypic Markers of Human Mesenchymal Stem Cell-Derived Corneal Limbal Epithelial*

Cells. Tissue Engineering and Regenerative Medicine, 2010. **7**(1): p. 87-92.

184. Bakhshi, T., et al., *Mesenchymal stem cells from the Wharton's jelly of umbilical cord segments provide stromal support for the maintenance of cord blood hematopoietic stem cells during long-term ex vivo culture*. *Transfusion*, 2008. **48**(12): p. 2638-2644.
185. Bochev, I., et al., *Mesenchymal stem cells from human bone marrow or adipose tissue differently modulate mitogen-stimulated B-cell immunoglobulin production in vitro*. *Cell Biology International*, 2008. **32**(4): p. 384-393.
186. Wang, X., et al., *Liquid-solid-solution synthesis of biomedical hydroxyapatite nanorods*. *Advanced Materials*, 2006. **18**(15): p. 2031-+.
187. Yu, J. and G.P. Smith, *Affinity maturation of phage-displayed peptide ligands*. *Methods Enzymol* 1996. **267**: p. 3-27.
188. Smith, G.P. and J.K. Scott, *Libraries of peptides and proteins displayed on filamentous phage*. *Methods Enzymol.*, 1993(217): p. 228-257.
189. Smith, G.P. and T.R. Gingrich, *Hydroxyapatite chromatography of phage-display virions* *Biotechniques* 2005. **39**(6): p. 879-884.
190. Holzer, G., T.A. Einhorn, and R.J. Majeska, *Estrogen regulation of growth and alkaline phosphatase expression by cultured human bone marrow stromal cells*. *Journal of Orthopaedic Research*, 2002. **20**(2): p. 281-288.
191. Mastrogiacomo, M., R. Cancedda, and R. Quarto, *Effect of different growth factors on the chondrogenic potential of human bone marrow stromal cells*. *Osteoarthritis and Cartilage*, 2001. **9**: p. S36-S40.

192. Walters, M.A., et al., *A Raman and Infrared Spectroscopic Investigation of Biological Hydroxyapatite*. Journal of Inorganic Biochemistry, 1990. **39**(3): p. 193-200.
193. Pearson, W.R. and D.J. Lipman, *Improved Tools for Biological Sequence Comparison*. Proceedings of the National Academy of Sciences of the United States of America, 1988. **85**(8): p. 2444-2448.
194. Altschul, S.F., et al., *Basic Local Alignment Search Tool*. Journal of Molecular Biology, 1990. **215**(3): p. 403-410.
195. Hoang, Q.Q., et al., *Bone recognition mechanism of porcine osteocalcin from crystal structure*. Nature, 2003. **425**(6961): p. 977-980.
196. Raghunathan, V., et al., *Homonuclear and heteronuclear NMR studies of a statherin fragment bound to hydroxyapatite crystals*. Journal of Physical Chemistry B, 2006. **110**(18): p. 9324-9332.
197. Dong, X.L., et al., *Understanding adsorption-desorption dynamics of BMP-2 on hydroxyapatite (001) surface*. Biophysical Journal, 2007. **93**(3): p. 750-759.
198. Makrodimitris, K., et al., *Structure prediction of protein-solid surface interactions reveals a molecular recognition motif of statherin for hydroxyapatite*. Journal of the American Chemical Society, 2007. **129**(44): p. 13713-13722.
199. Wang, Y.A., et al., *The structure of a filamentous bacteriophage*. Journal of Molecular Biology, 2006. **361**(2): p. 209-215.
200. Long, J.R., et al., *A peptide that inhibits hydroxyapatite growth is in an extended conformation on the crystal surface*. Proceedings of the

National Academy of Sciences of the United States of America, 1998.
95(21): p. 12083-12087.

201. Nassif, N., et al., *Self-Assembled Collagen-Apatite Matrix with Bone-like Hierarchy*. Chemistry of Materials, 2010. **22**(11): p. 3307-3309.
202. Cai, Y.R., et al., *Role of hydroxyapatite nanoparticle size in bone cell proliferation*. Journal of Materials Chemistry, 2007. **17**(36): p. 3780-3787.
203. Liu, Y.K., et al., *In vitro effects of nanophase hydroxyapatite particles on proliferation and osteogenic differentiation of bone marrow-derived mesenchymal stem cells*. Journal of Biomedical Materials Research Part A, 2009. **90A**(4): p. 1083-1091.
204. Dalby, M.J., et al., *The control of human mesenchymal cell differentiation using nanoscale symmetry and disorder*. Nature Materials, 2007. **6**(12): p. 997-1003.
205. Suchanek, W., et al., *Processing and mechanical properties of hydroxyapatite reinforced with hydroxyapatite whiskers*. Biomaterials, 1996. **17**(17): p. 1715-1723.
206. Suchanek, W., et al., *Hydroxyapatite/hydroxyapatite-whisker composites without sintering additives: Mechanical properties and microstructural evolution*. Journal of the American Ceramic Society, 1997. **80**(11): p. 2805-2813.
207. Cai, Y.R. and R.K. Tang, *Calcium phosphate nanoparticles in biomineralization and biomaterials*. Journal of Materials Chemistry, 2008. **18**(32): p. 3775-3787.

208. Berman, A., et al., *Total Alignment of Calcite at Acidic Polydiacetylene Films - Cooperativity at the Organic-Inorganic Interface*. *Science*, 1995. **269**(5223): p. 515-518.
209. Traub, W., T. Arad, and S. Weiner, *3-Dimensional Ordered Distribution of Crystals in Turkey Tendon Collagen-Fibers*. *Proceedings of the National Academy of Sciences of the United States of America*, 1989. **86**(24): p. 9822-9826.
210. Krag, D.N., et al., *Selection of tumor-binding ligands in cancer patients with phage display libraries (vol 66, pg 7724, 2006)*. *Cancer Research*, 2006. **66**(17): p. 8925-8925.
211. Shukla, G.S. and D.N. Krag, *Selection of tumor-targeting agents on freshly excised human breast tumors using a phage display library*. *Oncology Reports*, 2005. **13**(4): p. 757-764.
212. Ma, P.X. and R.Y. Zhang, *Synthetic nano-scale fibrous extracellular matrix*. *Journal of Biomedical Materials Research*, 1999. **46**(1): p. 60-72.
213. Hirano, Y. and D.J. Mooney, *Peptide and protein presenting materials for tissue engineering*. *Advanced Materials*, 2004. **16**(1): p. 17-25.
214. Romanov, V., D.B. Durand, and V.A. Petrenko, *Phage display selection of peptides that affect prostate carcinoma cells attachment and invasion*. *Prostate* 2001. **47**: p. 239-51.
215. Li, C.M., et al., *Electrospun silk-BMP-2 scaffolds for bone tissue engineering*. *Biomaterials*, 2006. **27**(16): p. 3115-3124.
216. Patel, S., et al., *Bioactive nanofibers: Synergistic effects of nanotopography and chemical signaling on cell guidance*. *Nano Letters*, 2007. **7**(7): p. 2122-2128.

217. Lee, C.H., et al., *Nanofiber alignment and direction of mechanical strain affect the ECM production of human ACL fibroblast*. *Biomaterials*, 2005. **26**(11): p. 1261-1270.
218. Theisen, C., et al., *Influence of nanofibers on growth and gene expression of human tendon derived fibroblast*. *Biomedical Engineering Online*, 2010. **9**: p. -.
219. Beachley, V. and X.J. Wen, *Fabrication of nanofiber reinforced protein structures for tissue engineering*. *Materials Science & Engineering C-Materials for Biological Applications*, 2009. **29**(8): p. 2448-2453.
220. Lim, J.Y. and H.J. Donahue, *Cell sensing and response to micro- and nanostructured surfaces produced by chemical and topographic patterning*. *Tissue Engineering*, 2007. **13**(8): p. 1879-1891.
221. Flemming, R.G., et al., *Effects of synthetic micro- and nano-structured surfaces on cell behavior*. *Biomaterials*, 1999. **20**(6): p. 573-588.
222. Yoo, P.J., et al., *Spontaneous assembly of viruses on multilayered polymer surfaces*. *Nature Materials*, 2006. **5**(3): p. 234-240.
223. Rong, J.H., et al., *Oriented cell growth on self-assembled bacteriophage M13 thin films*. *Chemical Communications*, 2008(41): p. 5185-5187.
224. Merzlyak, A., S. Indrakanti, and S.W. Lee, *Genetically Engineered Nanofiber-Like Viruses For Tissue Regenerating Materials*. *Nano Letters*, 2009. **9**(2): p. 846-852.
225. Ren, Y., S.M. Wong, and L.Y. Lim, *Folic acid-conjugated protein cages of a plant virus: A novel delivery platform for doxorubicin*. *Bioconjugate Chemistry*, 2007. **18**(3): p. 836-843.

226. Lee, L.A. and Q. Wang, *Adaptations of nanoscale viruses and other protein cages for medical applications*. *Nanomedicine-Nanotechnology Biology and Medicine*, 2006. **2**(3): p. 137-149.
227. Frenkel, D. and B. Solomon, *Filamentous phage as vector-mediated antibody delivery to the brain*. *Proceedings of the National Academy of Sciences of the United States of America*, 2002. **99**(8): p. 5675-5679.
228. van den Beucken, J.J.J.P., et al., *Fabrication, characterization, and biological assessment of multilayered DNA-coatings for biomaterial purposes*. *Biomaterials*, 2006. **27**(5): p. 691-701.
229. Zhu, H.B., et al., *Osteogenic actions of the osteogenic growth peptide on bovine marrow mesenchymal stromal cells in culture*. *Veterinarni Medicina*, 2008. **53**(9): p. 501-509.
230. Wang, J.H.C., et al., *Cell orientation determines the alignment of cell-produced collagenous matrix*. *Journal of Biomechanics*, 2003. **36**(1): p. 97-102.
231. Friedl, P., K.S. Zanker, and E.B. Brocker, *Cell migration strategies in 3-D extracellular matrix: Differences in morphology, cell matrix interactions, and integrin function*. *Microscopy Research and Technique*, 1998. **43**(5): p. 369-378.
232. Yin, Z., et al., *The regulation of tendon stem cell differentiation by the alignment of nanofibers*. *Biomaterials*, 2010. **31**(8): p. 2163-2175.
233. Kaur, G., et al., *The promotion of osteoblastic differentiation of rat bone marrow stromal cells by a polyvalent plant mosaic virus*. *Biomaterials*, 2008. **29**(30): p. 4074-4081.

234. Weiss, P., *EXPERIMENTS ON CELL AND AXON ORIENTATION INVITRO - THE ROLE OF COLLOIDAL EXUDATES IN TISSUE ORGANIZATION*. Journal of Experimental Zoology, 1945. **100**(3): p. 353-386.
235. Oakley, C., N.A.F. Jaeger, and D.M. Brunette, *Sensitivity of fibroblasts and their cytoskeletons to substratum topographies: Topographic guidance and topographic compensation by micromachined grooves of different dimensions*. Experimental Cell Research, 1997. **234**(2): p. 413-424.
236. Miller, C., et al., *Oriented Schwann cell growth on micropatterned biodegradable polymer substrates*. Biomaterials, 2001. **22**(11): p. 1263-1269.
237. Sarkar, S., et al., *Fabrication of a layered microstructured polycaprolactone construct for 3-D tissue engineering*. Journal of Biomaterials Science-Polymer Edition, 2008. **19**(10): p. 1347-1362.
238. Matthews, J.A., et al., *Electrospinning of collagen nanofibers*. Biomacromolecules, 2002. **3**(2): p. 232-238.
239. Min, B.M., et al., *Electrospinning of silk fibroin nanofibers and its effect on the adhesion and spreading of normal human keratinocytes and fibroblasts in vitro*. Biomaterials, 2004. **25**(7-8): p. 1289-1297.
240. Wnek, G.E., et al., *Electrospinning of nanofiber fibrinogen structures*. Nano Letters, 2003. **3**(2): p. 213-216.
241. Boland, E.D., et al., *Electrospinning collagen and elastin: Preliminary vascular tissue engineering*. Frontiers in Bioscience, 2004. **9**: p. 1422-1432.

242. Rahnert, J., et al., *The role of nitric oxide in the mechanical repression of RANKL in bone stromal cells*. Bone, 2008. **43**(1): p. 48-54.
243. Bhadang, K.A., et al., *Biological responses of human osteoblasts and osteoclasts to flame-sprayed coatings of hydroxyapatite and fluorapatite blends*. Acta Biomaterialia, 2010. **6**(4): p. 1575-1583.
244. Tang, N., et al., *BMP-9-induced osteogenic differentiation of mesenchymal progenitors requires functional canonical Wnt/beta-catenin signalling*. Journal of Cellular and Molecular Medicine, 2009. **13**(8B): p. 2448-2464.
245. Subramanian, A., U.M. Krishnan, and S. Sethuraman, *Development of biomaterial scaffold for nerve tissue engineering: Biomaterial mediated neural regeneration*. Journal of Biomedical Science, 2009. **16**.
246. Tapia, J.M., et al., *Interrelation between cells and extracellular polymeric substances (EPS) from Acidiphilium 3.2Sup(5) on carbon surfaces*. Biohydrometallurgy: A Meeting Point between Microbial Ecology, Metal Recovery Processes and Environmental Remediation, 2009. **71-73**: p. 287-290.
247. Kulangara, K. and K.W. Leong, *Substrate topography shapes cell function*. Soft Matter, 2009. **5**(21): p. 4072-4076.
248. Gerecht, S., et al., *The effect of actin disrupting agents on contact guidance of human embryonic stem cells*. Biomaterials, 2007. **28**(28): p. 4068-4077.
249. Recknor, J.B., D.S. Sakaguchi, and S.K. Mallapragada, *Directed growth and selective differentiation of neural progenitor cells on micropatterned polymer substrates*. Biomaterials, 2006. **27**(22): p. 4098-4108.

250. Recknor, J.B., et al., *Oriented astroglial cell growth on micropatterned polystyrene substrates*. *Biomaterials*, 2004. **25**(14): p. 2753-2767.
251. Moon, J.H. and S. Yang, *Chemical Aspects of Three-Dimensional Photonic Crystals*. *Chemical Reviews*, 2010. **110**(1): p. 547-574.
252. de Villeneuve, V.W.A., et al., *Colloidal hard-sphere crystal growth frustrated by large spherical impurities*. *Science*, 2005. **309**(5738): p. 1231-1233.
253. Lopez, C., *Materials aspects of photonic crystals*. *Advanced Materials*, 2003. **15**(20): p. 1679-1704.
254. Hawkins, R.J. and R.A. Aldoroty, *The Osmotic Bulk Modulus of a Colloid Crystal of Infinite Rod-Like Molecules*. *Chemical Physics Letters*, 1987. **137**(1): p. 83-85.
255. Egelman, E.H., N. Francis, and D.J. Derosier, *Helical Disorder and the Filament Structure of F-Actin Are Elucidated by the Angle-Layered Aggregate*. *Journal of Molecular Biology*, 1983. **166**(4): p. 605-629.
256. Mcpherson, A., A.J. Malkin, and Y.G. Kuznetsov, *The Science of Macromolecular Crystallization*. *Structure*, 1995. **3**(8): p. 759-768.
257. Malkin, A.J., et al., *Mechanisms of Growth for Protein and Virus Crystals*. *Nature Structural Biology*, 1995. **2**(11): p. 956-959.
258. Boistelle, R. and J.P. Astier, *Crystallization Mechanisms in Solution*. *Journal of Crystal Growth*, 1988. **90**(1-3): p. 14-30.
259. Yamamoto, K., et al., *Study on Structure of Paracrystals of F-Actin*. *Journal of Molecular Biology*, 1975. **91**(4): p. 463-&.

260. Wang, F., et al., *Genetically Modifiable Flagella as Templates for Silica Fibers: From Hybrid Nanotubes to 1D Periodic Nanohole Arrays* (vol 18, pg 4007, 2008). *Advanced Functional Materials*, 2009. **19**(21): p. 3355-3355.

Appendix

List of Copyrights and Permissions:



Dear Binui Cao

We hereby grant you permission to reprint the material detailed below at no charge in your thesis subject to the following conditions:

1. If any part of the material to be used (for example, figures) has appeared in our publication with credit or acknowledgement to another source, permission must also be sought from that source. If such permission is not obtained then that material may not be included in your publication/copies.
2. Suitable acknowledgment to the source must be made, either as a footnote or in a reference list at the end of your publication, as follows:

"This article was published in Publication title, Vol number, Author(s), Title of article, Page Nos, Copyright Elsevier (or appropriate Society name) (Year)."
3. Your thesis may be submitted to your institution in either print or electronic form.
4. Reproduction of this material is confined to the purpose for which permission is hereby given.
5. This permission is granted for non-exclusive word **English** rights only. For other languages please reapply separately for each one required. Permission excludes use in an electronic form other than the submission. Should you have a specific electronic project in mind please reapply for permission.
6. This includes permission for UMI to supply single copies, on demand, of the complete thesis. Should your thesis be published commercially, please reapply for permission.

Yours sincerely

Jennifer Jones
Rights Assistant

Elsevier Limited, a company registered in England and Wales with company number 1982084, whose registered office is The Boulevard, Langford Lane, Kidlington, Oxford, OX5 1GB, United Kingdom.

AMERICAN CHEMICAL SOCIETY LICENSE
TERMS AND CONDITIONS

Dec 15, 2010

This is a License Agreement between Binrui Cao ("You") and American Chemical Society ("American Chemical Society") provided by Copyright Clearance Center ("CCC"). The license consists of your order details, the terms and conditions provided by American Chemical Society, and the payment terms and conditions.

All payments must be made in full to CCC. For payment instructions, please see information listed at the bottom of this form.

License Number	2527820408835
License Date	Oct 14, 2010
Licensed content publisher	American Chemical Society
Licensed content publication	Langmuir
Licensed content title	Oriented Nucleation of Hydroxylapatite Crystals on Spider Dragline Silks
Licensed content author	Binrui Cao et al.
Licensed content date	Oct 1, 2007
Volume number	23
Issue number	21
Type of Use	Thesis/Dissertation
Requestor type	Not specified
Format	Print
Portion	Full article
Author of this ACS article	Yes
Order reference number	
Title of the thesis / dissertation	Filamentous Biological Macromolecules Based Nanostructures and Their Applications.
Expected completion date	Dec 2010
Estimated size(pages)	150
Billing Type	Invoice
Billing Address	620 Parrington Oval, Room 208 Norman Norman, OK 73019 United States
Customer reference info	
Total	0.00 USD
Terms and Conditions	

AMERICAN CHEMICAL SOCIETY LICENSE
TERMS AND CONDITIONS

Dec 15, 2010

This is a License Agreement between Binrui Cao ("You") and American Chemical Society ("American Chemical Society") provided by Copyright Clearance Center ("CCC"). The license consists of your order details, the terms and conditions provided by American Chemical Society, and the payment terms and conditions.

All payments must be made in full to CCC. For payment instructions, please see information listed at the bottom of this form.

License Number	2527820660274
License Date	Oct 14, 2010
Licensed content publisher	American Chemical Society
Licensed content publication	Biomacromolecules
Licensed content title	Identification of Microtubule-Binding Domains on Microtubule-Associated Proteins by Major Coat Phage Display Technique
Licensed content author	Binrui Cao et al.
Licensed content date	Mar 1, 2009
Volume number	10
Issue number	3
Type of Use	Thesis/Dissertation
Requestor type	Not specified
Format	Print
Portion	Full article
Author of this ACS article	Yes
Order reference number	
Title of the thesis / dissertation	Filamentous Biological Macromolecules Based Nanostructures and Their Applications.
Expected completion date	Dec 2010
Estimated size(pages)	150
Billing Type	Invoice
Billing Address	101 Stephenson Parkway
	Norman, OK 73019
	United States
Customer reference info	
Total	0.00 USD
Terms and Conditions	

AMERICAN CHEMICAL SOCIETY LICENSE
TERMS AND CONDITIONS

Dec 15, 2010

This is a License Agreement between Binrui Cao ("You") and American Chemical Society ("American Chemical Society") provided by Copyright Clearance Center ("CCC"). The license consists of your order details, the terms and conditions provided by American Chemical Society, and the payment terms and conditions.

All payments must be made in full to CCC. For payment instructions, please see information listed at the bottom of this form.

License Number	2527840059212
License Date	Oct 14, 2010
Licensed content publisher	American Chemical Society
Licensed content publication	Chemistry of Materials
Licensed content title	Bacteriophage Bundles with Prealigned Ca ²⁺ Initiate the Oriented Nucleation and Growth of Hydroxylapatite
Licensed content author	Fuke Wang et al.
Licensed content date	Jun 1, 2010
Volume number	22
Issue number	12
Type of Use	Thesis/Dissertation
Requestor type	Not specified
Format	Print
Portion	Table/Figure/Micrograph
Number of Table/Figure /Micrographs	1
Author of this ACS article	No
Order reference number	
Title of the thesis / dissertation	Filamentous Biological Macromolecules Based Nanostructures and Their Applications.
Expected completion date	Dec 2010
Estimated size(pages)	150
Billing Type	Invoice
Billing Address	101 Stephenson Parkway Norman, OK 73019 United States
Customer reference info	
Total	0.00 USD
Terms and Conditions	

THE AMERICAN ASSOCIATION FOR THE ADVANCEMENT OF SCIENCE LICENSE
TERMS AND CONDITIONS

Dec 15, 2010

This is a License Agreement between Binrui Cao ("You") and The American Association for the Advancement of Science ("The American Association for the Advancement of Science") provided by Copyright Clearance Center ("CCC"). The license consists of your order details, the terms and conditions provided by The American Association for the Advancement of Science, and the payment terms and conditions.

All payments must be made in full to CCC. For payment instructions, please see information listed at the bottom of this form.

License Number	2527840481699
License date	Oct 14, 2010
Licensed content publisher	The American Association for the Advancement of Science
Licensed content publication	Science
Licensed content title	Fabricating Genetically Engineered High-Power Lithium-Ion Batteries Using Multiple Virus Genes
Licensed content author	Yun Jung Lee, Hyunjung Yi, Woo-Jae Kim, Kisuk Kang, Dong Soo Yun, Michael S. Strano, Gerbrand Ceder, Angela M. Belcher
Licensed content date	May 22, 2009
Type of Use	Thesis / Dissertation
Requestor type	Other Individual
Format	Print and electronic
Portion	Figure
Number of figures/tables	3
Order reference number	
Title of your thesis / dissertation	Filamentous Biological Macromolecules Based Nanostructures and Their Applications.
Expected completion date	Dec 2010
Estimated size(pages)	150
Total	0.00 USD
Terms and Conditions	

THE AMERICAN ASSOCIATION FOR THE ADVANCEMENT OF SCIENCE LICENSE
TERMS AND CONDITIONS

Dec 15, 2010

This is a License Agreement between Binrui Cao ("You") and The American Association for the Advancement of Science ("The American Association for the Advancement of Science") provided by Copyright Clearance Center ("CCC"). The license consists of your order details, the terms and conditions provided by The American Association for the Advancement of Science, and the payment terms and conditions.

All payments must be made in full to CCC. For payment instructions, please see information listed at the bottom of this form.

License Number	2527840791534
License date	Oct 14, 2010
Licensed content publisher	The American Association for the Advancement of Science
Licensed content publication	Science
Licensed content title	X-ray Structure of the FimC-FimH Chaperone-Adhesin Complex from Uropathogenic Escherichia coli
Licensed content author	Devapriya Choudhury, Andrew Thompson, Vivian Stojanoff, Solomon Langermann, Jerome Pinkner, Scott J. Hultgren, Stefan D. Knight
Licensed content date	Aug 13, 1999
Type of Use	Thesis / Dissertation
Requestor type	Other Individual
Format	Print and electronic
Portion	Figure
Number of figures/tables	1
Order reference number	
Title of your thesis / dissertation	Filamentous Biological Macromolecules Based Nanostructures and Their Applications.
Expected completion date	Dec 2010
Estimated size(pages)	150
Total	0.00 USD
Terms and Conditions	

ELSEVIER LICENSE
TERMS AND CONDITIONS

Dec 15, 2010

This is a License Agreement between Binrui Cao ("You") and Elsevier ("Elsevier") provided by Copyright Clearance Center ("CCC"). The license consists of your order details, the terms and conditions provided by Elsevier, and the payment terms and conditions.

All payments must be made in full to CCC. For payment instructions, please see information listed at the bottom of this form.

Supplier	Elsevier Limited The Boulevard, Langford Lane Kidlington, Oxford, OX5 1GB, UK
Registered Company Number	1982084
Customer name	Binrui Cao
Customer address	101 Stephenson Parkway Norman, OK 73019
License number	2527841053282
License date	Oct 14, 2010
Licensed content publisher	Elsevier
Licensed content publication	Journal of Molecular Biology
Licensed content title	Exploring the 3D Molecular Architecture of <i>Escherichia coli</i> Type 1 Pill
Licensed content author	Erik Hahn, Peter Wild, Uta Hermanns, Peter Sebbel, Rudi Glockshuber, Marcus Häner, Nicole Taschner, Peter Burkhard, Ueli Aepli, Shirley A. Müller
Licensed content date	8 November 2002
Licensed content volume number	323
Licensed content issue number	5
Number of pages	13
Start Page	845
End Page	857
Type of Use	reuse in a thesis/dissertation
Intended publisher of new work	other
Portion	figures/tables/illustrations
Number of figures/tables/illustrations	1
Format	print
Are you the author of this Elsevier article?	No
Will you be translating?	No
Order reference number	
Title of your thesis/dissertation	Filamentous Biological Macromolecules Based Nanostructures and Their Applications.
Expected completion date	Dec 2010
Estimated size (number of pages)	150
Elsevier VAT number	GB 494 6272 12
Permissions price	0.00 USD
Value added tax 0.0%	0.0 USD / 0.0 GBP
Total	0.00 USD
Terms and Conditions	